Organellomics: AI-driven deep organellar phenotyping reveals novel ALS mechanisms in human neurons

Sagy Krispin[1,2*], Welmoed van Zuiden[1,2*], Yehuda M. Danino[1,2*], Noam Rudberg[1,2], Lena Molitor[1,2], Bar Abarbanel[1,2],Gal Aviram[1,2], Gili Wolf[1,2], Chen Bar[1,2], Aviad Siani[1,2], Thea Meimoun[1,2], Alyssa N. Coyne[3,4], Marianita Santiana[5], Cory A. Weller[5], Mark R Cookson[5,6], Michael E Ward[5,7], Fergal M Waldron[8], Jenna M Gregory[8,9], Tal Fisher[1], Aharon Nachshon[1], Noam Stern-Ginossar[1], Nancy Yacovzada[1,2#], Eran Hornstein[1,2$]

[1]Department of Molecular Genetics, Weizmann Institute of Science, Israel.

[2]Department of Molecular Neuroscience, Weizmann Institute of Science, Israel.

[3]Department of Neurology, Johns Hopkins University School of Medicine, Baltimore, MD, USA.

[4]Brain Science Institute, Johns Hopkins University School of Medicine, Baltimore, MD, USA.

[5]Center for Alzheimer's Disease and Related Dementias, National Institutes of Health, Bethesda, MD, USA;

[6]Laboratory of Neurogenetics, National Institute on Aging, National Institutes of Health, Bethesda, MD, USA.

[7]National Institute of Neurological Disorders and Stroke, National Institutes of Health, Bethesda, MD, USA.

[8]Institute of Medical Sciences, University of Aberdeen, Aberdeen, UK.

[9]Department of Pathology, NHS Grampian Tissue Biorepository, Aberdeen, UK.

* These authors contributed equally

Corresponding Author for machine learning: Nancyy@weizmann.ac.il

$ Corresponding Author for all other facets of the work: Eran.Hornstein@weizmann.ac.il

Abstract

Systematic assessment of organelle architectures, termed the *organellome*, offers valuable insights into cellular states and pathomechanisms, but remains largely uncharted. Here, we present a deep phenotypic learning based on vision transformers, resulting in the Neuronal Organellomics Vision Atlas (NOVA) model that studies confocal images of more than 30 markers of distinct membrane-bound and membraneless organelles in 11.5 million images of human neurons. Organellomics analysis quantifies perturbation-induced changes in organelle localization and morphology using a rigorous mixed-effects meta-analytic framework that accounts for sampling variance and experimental heterogeneity. Applying this approach, we delineate phenotypic alterations in neurons carrying ALS-associated mutations and uncover a physical and functional crosstalk between cytoplasmic mislocalized TDP-43, a hallmark of ALS, and processing bodies (P-bodies), membraneless organelles regulating mRNA stability. These findings are validated in patient-derived neurons and human neuropathology. NOVA establishes a scalable framework for quantitative mapping of subcellular phenotypes and provides a new avenue for investigating the neurocellular basis of disease.

Keywords: AI, computer vision, deep learning, vision transformers, perturbations learning, contrastive learning, mixed effect, high throughput screening, neurodegeneration, subcellular architecture, organelles, biomolecular condensates.

Introduction

Organellomics, the systematic study of subcellular organellar architecture (the organellome), may be a useful strategy to directly phenotype cells by their subcellular compartments. This is conceivable since the quantification of RNAs, lipids, metabolites and proteins that compose organelles cannot be directly translated into complex organelle properties. Furthermore, organelles are interconnected by functional crosstalk and inter-organelle interdependency [1,2], further supporting the value of organellomics-level insights for cell biology.

The analysis of multiple organelles poses substantial challenges due to the diversity of their localizations and morphologies, which must be integrated and evaluated in parallel. Systematic quantification of organellar proteomic content using mass spectrometry–based approaches is highly informative [3–10]. However, mass spectrometry does not provide spatial or morphological context and depends on designated biochemical specializations. In addition, imaging-based approaches have been developed [11–23]; however, these are largely limited to non-polarized cultured cells.

The study of cellular organization has been traditionally focused on membrane-restricted organelles, such as the nucleus and mitochondria. However, in recent years, certain biomolecular condensates have been identified as membraneless organelles with specialized functions [24–28]. Therefore, the study of both membrane-restricted and membraneless organelles is important for gaining a comprehensive view of cellular biology.

The dysfunction of organelles is a central driver of disease. Disorders of membrane-bound organelles such as mitochondria, lysosomes, or autophagosomes have been comprehensively characterized and are associated with distinctive clinical pictures [29–34]. In addition, compelling evidence suggests a role for membraneless organellar dysfunction in neurodegeneration [28,35,36].

We hypothesized that comprehensively capturing the localization and morphological patterns across the entire organellome would allow unbiased mapping of organellar responses to perturbations using a unified scale. To test this hypothesis, we employed an image representation learning approach, particularly based on Vision Transformers (ViT [37,38]) tailored for perturbation learning [21,39–45], to capture high-level abstraction features from fluorescent confocal images. Deep representation learning enables automatic feature extraction, which is unbiased and does not require a pre-defined object or task. Hence it describes any localization and morphological pattern in the image, surpassing widely used approaches to extract objects from images based on a-priori assumptions [13,46,47].

ViTs have emerged as powerful models for analyzing microscopy images. Unlike traditional convolutional neural networks (CNNs), ViTs offer enhanced flexibility in capturing global relationships within images by processing the input as a sequence of image patches, and leveraging self-attention to compute dependencies between patches [37]. This capability is crucial for identifying minute, yet meaningful, alterations in neuronal structure and organization that can arise from specific perturbations. This characteristic makes ViTs well-suited for complex tasks such as deep phenotypic learning in diverse cellular environments, where quantification of spatial relationships of subtle organellar variations is critical.

Here, we introduce Neuronal Organellomics Vision Atlas (NOVA). The contrastive learning framework employed to minimize natural variation, forced the model to focus on genuine perturbation effects through learning transitive relationships between conditions. NOVA takes as input immunofluorescence images of a given cellular organelle in cultured cells and quantifies perturbational changes. NOVA was first pre-trained on massive amounts of OpenCell data [48] to learn to encode for subcellular localization patterns of 1,311 proteins. Then, the pre-trained model was fine-tuned for a perturbation learning task on data from highly polarized human neuronal cells incorporating diverse chemical or disease-relevant genetic perturbations. NOVA neither requires detection of the cellular borders (segmentation) nor a pre-defined task, overcoming a limitation in neuron image analysis, and is sensitive enough to depict organellome changes associated with single nucleotide genetic variants. To ensure reporting of reproducible results, NOVA enables mapping of organellar responses to perturbation by quantifying combined effect across experimental repeats using mixed-effect meta-analysis. Our organellomics approach introduces an AI-powered imaging tool that interrogates neuro-cellular biology by capturing phenotypes defined by organelle localization and morphology. We reveal functional interactions between mislocalized cytoplasmic TDP-43 - a hallmark of ALS - and P-bodies, which regulate mRNA stability, validated in patient-derived neurons. This approach offers the foundation for future hypothesis generation in neurobiology and proposes new biomarkers for human pathology.

Results

Generation of comprehensive imaging datasets to study the organellome of human neurons

The complexity of the organellome necessitates a modeling strategy that inspects unbiased, quantitative data of multiple organelles. Here, we devised a set of 25 markers for key membrane-bound and membraneless organelles (**Figure 1A** and **Table 1**). Images of neurons with specific dyes or immune-staining (image sites or 'sites') were captured by a spinning disc confocal microscope and subjected to QC and preprocessing steps, resulting in single cell tile images (1.5 neurons per tile on average, **Supplementary Figure 2** and **Supplementary Materials**). A comprehensive training dataset was generated, composed of ~3.2 million image tiles of human iPSC-derived neurons, under different experimental conditions (i.e., 1 chemical, 7 genetic perturbations, and WT; **Supplementary Figure 1**). This data was used for model training (2.24M images), validation (0.48M images), and test (0.48M images). The training dataset was generated from two independent biological differentiations (referred to as "experimental repeats"), with each differentiation including two to eight technical repeats per condition (**Supplementary Figure 1**).

All 6 independent datasets described below, encompassing a total of ~11.56M tile images, of which ~2.55M were used solely for inference (held-out from training). Furthermore, these datasets originated from different experiments in different labs, spanned different cell lines, and included unseen organelles (**Supplementary Materials**).

ViT for encoding organelle localization patterns in perturbed human neurons

Vision Transformers (ViTs), with their self-attention mechanism, excel at modeling long-range spatial relationships across image patches, making them particularly effective for capturing fine-grained cellular details in microscopy images [37]. This is particularly valuable for neurons, whose morphology is far more complex than that of simple cells. Neurons extend processes over large spatial scales, with organelles distributed across axons, dendrites, and soma. Thus, we decided to develop a VIT model to recognize intricate localization patterns and understand perturbation microscopic effects.

To examine organellar changes in neuronal cells upon disease-associated perturbations, we developed NOVA, a sequential fine-tuned model based on ViTs and contrastive learning (**Figure 1B**). First, we trained a ViT model with a multi-class classification head and cross-entropy loss on a publicly available dataset of 1,311 OpenCell proteins in human embryonic kidney cells that were cultured in basal growth conditions (HEK293T, 1,100,253 image tiles[48]). By learning to predict the protein identity in the image (loss curves in **Supplementary Figure 3A**), the model learns to encode a wide variety of organellar morphologies and localizations (referred here as topographies), achieving mean accuracy of 87% in identification of organelle localization categories (ROC AUC curves, confusion matrix and UMAP visualization of localization categories in **Supplementary Figure 3B-D**).

We next extended the model to perform a perturbation learning task by continuing the training with images of neurons with perturbations (**Methods**). To retain the knowledge learned from the localization encoding task, a partial fine-tuning step was performed, using an angle-metric [49] optimization approach on the model's layers (**Supplementary Figure 4** and **Methods**). Specifically, the

angle-metric quantified how much each layer changed between the localization and perturbation tasks. Layers showing minimal deviation were kept frozen to preserve general knowledge, while layers with deviations larger than the median were retrained to adapt the model to neuron-specific and perturbation-related features.

The perturbation learning head and loss function were devised to perform contrastive learning, using Information Noise Contrastive Estimation loss (InfoNCE, **Figure 1B** and **Supplementary Figures 5**, **6**). InfoNCE loss encourages the model to implicitly learn to focus on similarities or dissimilarities that correspond to true perturbation effects. Hence, impactful perturbations are pushed apart in the latent space, diverging their feature representations away from the baseline, control condition. In parallel, perturbations without effect generated similar representations, ensuring that the model doesn't overfit irrelevant non-biological differences or technical artifacts. Together, NOVA performs two tasks: (1) the encoding of neuron images for feature representations, and (2) detecting true perturbation effects.

Full neuronal organelle landscape in unperturbed neurons

As an initial characterization of the neuronal organellome, we sought to establish proof of feasibility for the identification of organelles in the basal, unperturbed state. Therefore, we performed inference on images from three experimental repeats of unperturbed neurons acquired in the NIH CARD (using a Ti2 Spinning Disk confocal microscope, 8 technical repeats per experimental repeat, 296,776 neuron images post QC). 26 organelles were analyzed, including microtubules (TUJ1) and TIA1 granules, two organelles not previously seen by the model in the training set.

Images of unperturbed neurons were encoded using NOVA, and the three experimental repeats were jointly projected into a single Uniform Manifold Approximation and Projection (UMAP)[50] plot (**Figure 1C**). The full neuronal organelle landscape revealed distinct clusters corresponding to most organelles, indicating that the learned embeddings capture organelle-specific features, and that experimental repeat effects did not dominate the latent space. Furthermore, the resulting image representations were evaluated with a post-hoc classifier for neuronal organelle identification (**Methods**) and achieved 99.57% accuracy in correctly calling each of the 26 organelle averaged across all experimental repeats (**Supplementary Figure 7** and **Methods**).

We benchmarked neuronal organelle identification by comparing performance of a classifier trained on representations extracted by NOVA versus Cytoself model[11] or CellProfiler[13,47] features. The classifier trained on NOVA's embeddings achieved the highest sensitivity performance (sensitivity 90.26%, accuracy 99.57%, **Figure 1C**), outperforming Cytoself (sensitivity 83.66%, accuracy 99.28%) and CellProfiler (sensitivity 79.88%, accuracy 98.62%). Organellar maps generated with Cytoself or CellProfiler appeared more diffuse than those from NOVA (**Supplementary Figure 8**), likely because NOVA has learned images of neurons and is trained to minimize experimental repeat-related variability.

To quantify relationships between organelles, we computed the pairwise Euclidean distances between organelles, using the full latent representations, and rescaled by min-max normalization to [0,1] (distance noted as d, **Supplementary Figure 9**). Small distances in the latent space indicate that

178 the model has captured organelle similarities in their morphology (size, shape, texture) or spatial
179 context (co-occurrence within the same subcellular regions).

180 As expected, pairwise distance analysis revealed neighborhoods of organelles with evident
181 physical and/or functional crosstalk. Mitochondria-outer-membrane (MOM), peroxisomes, and
182 lysosomes clustered closely, with a mean intra-community distance of d=0.21, compared to a mean
183 inter-community distance of d=0.74 (**Supplementary Figure 9**). This is consistent with known
184 communication through membrane contact sites, shared functions and linked dysfunction in
185 Parkinson's disease[51–56]. Likewise, the cytoskeleton-associated organelles, actin cytoskeleton and
186 microtubules, presented an intra-community distance of d=0.22, as also apparent in the UMAP
187 projection (**Figure 1C**). Unexpectedly, Mitotracker-labeled mitochondria, which preferentially mark
188 active mitochondria, were distant from MOM (d = 0.8, **Supplementary Figure 9**), likely reflecting
189 functional or structural differences between these subcompartments which are of biological interest.
190 We note that one of the lowest pairwise distances (d = 0.11) was between NEMO granules, essential
191 for NF-κB signaling[57], and the postsynapse (PSD-95; **Supplementary Figure 9**), suggesting potential
192 new functional links. Finally, the low pairwise distances of TDP-43 granules to paraspeckles (d = 0.22)
193 and ANXA11 granules (d = 0.27) align with reported interactions in ALS and FTD[58–64]. Taken together,
194 the relative concordance between multiple experimental repeats UMAP and latent-space distances
195 supports the robustness of NOVA, whose embedding space captures organelle neighborhoods and
196 reveals potential new biological relationships.

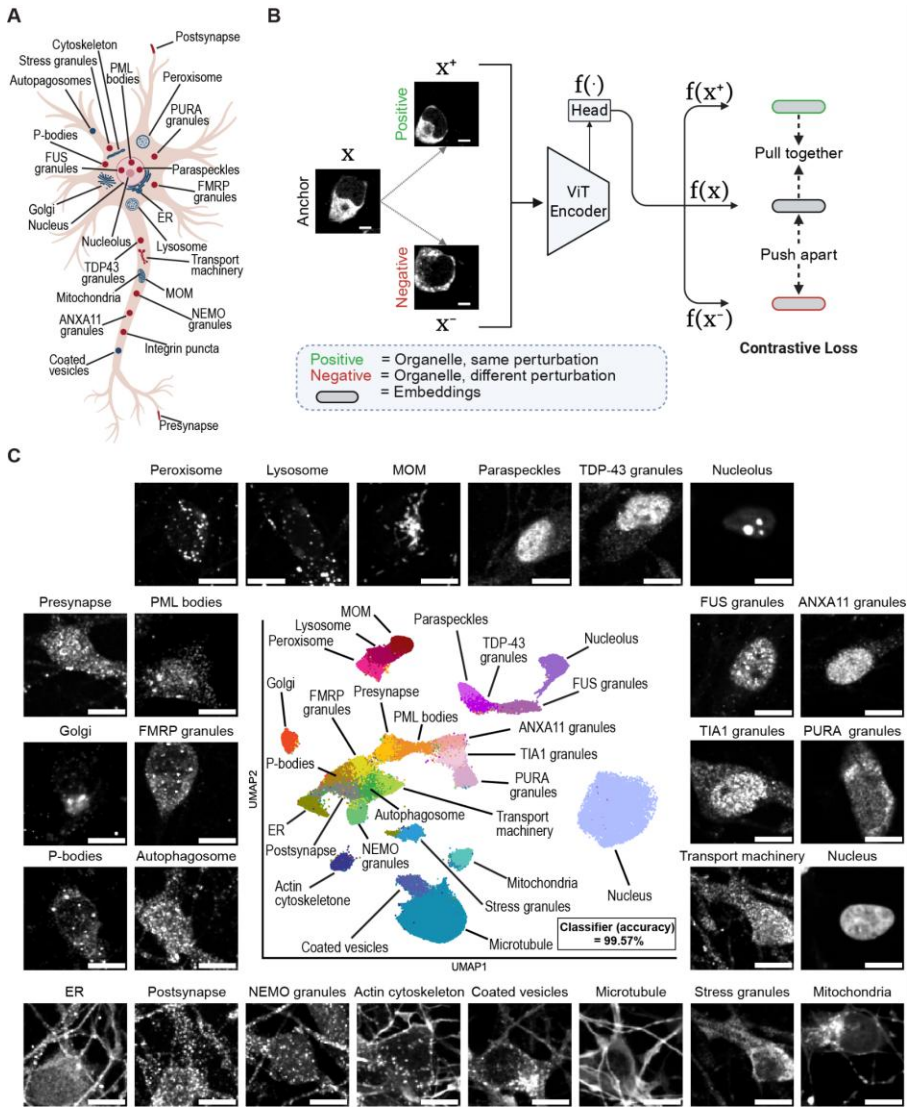

Figure 1. Vision transformer-based perturbation learning model enables organellomic studies in neurons. (A) Diagram of a neuron with the 25 organelles used for sequential fine-tuned training in NOVA. **(B)** Perturbation learning workflow with contrastive learning. An input image (anchor) is encoded into 192 latent features (embeddings). Each anchor is randomly matched with other images of the same organelle under the same perturbation ("positives," similar effects) and with images of the same organelle under different perturbations ("negatives," dissimilar or no effect). During training, the model converges to establish meaningful representations via contrastive loss: pulling together positives in feature space, while pushing apart negatives based on the distinct differences learned from the data. Perturbations with no apparent effect result in feature representations similar to unperturbed cells. To prevent the model overfitting to potential experimental repeat or well effects, positives and negatives were sampled from different experimental repeats and wells (**Supplementary Figure 6** and **Methods** for details). **(C)** UMAP visualization of jointly projected three experimental repeats, showing the organellar landscape of day 8 human iPSC-derived neurons under basal growth conditions. 26 organelles form distinct topographic patterns (classifier accuracy 99.57%; see

213 **Supplementary Figure 7** and **Methods**). ~6k image tiles per organelle. Representative images
214 displayed. Scale bar, 5 µm.

215 **Table 1**. **Key 26 organelles characterized in this study, respective abbreviations and markers**

Organelle	Abbr.	Marker	Literature
Nucleus		Hoechst 33342	[65]
Mitochondria		Mitotracker	[66]
Mitochondria Outer Membrane	MOM	TOMM20	[67]
Golgi Apparatus	Golgi	GM130	[68]
Endoplasmic Reticulum	ER	Calreticulin	[69]
Actin Cytoskeleton	Cytoskeleton	Phalloidin	[70]
Microtubule Cytoskeleton	Microtubule	Tubulin or TUJ1 (beta Tubulin 3)	[71–73]
Autophagosomes		SQSTM1	[74]
Lysosomes		LAMP1	[75]
Peroxisomes		PEX14	[76]
Coated Vesicles		CLTC	[77]
Nucleolus		NCL	[78]
Paraspeckles		NONO	[79,80]
TDP-43 granules		TDP-43	[81]
FUS granules		FUS	[82]
Promyelocytic Leukaemia Nuclear Bodies	PML bodies	PML	[83]
P-Bodies		DCP1A or LSM14A	[84,85]
Stress granules		G3BP1	[86]
ANXA11 granules		ANXA11	[87]
PURA granules		PURA	[88,89]
NEMO granules		NEMO	[57]
Microtubule-Associated Transport Machinery	Transport machinery	KIF5A	[90]
Presynaptic Terminals	Presynapse	SNCA	[91,92]
Post-Synaptic Subcompartments	Postsynapse	PSD95	[93]
FMRP granules		FMRP	[94]
Nuclear speckles		SON	[95]

216

217 **A ranking system for quantification of the organellar response across experimental repeats**

218 For each perturbation under examination during inference, the NOVA-derived embeddings of control
219 images versus perturbed are utilized to estimate an effect size for each organelle across experimental
220 repeats (biological differentiations or human subjects). Effect size is designed to capture the degree
221 to which a perturbation shifts organelle topography from the baseline state, and is estimated for each
222 combination of (perturbation × organelle × experimental repeat). Then, effect sizes are combined in
223 mixed-effects meta-analytic analysis to estimate the combined effect size (denoted $\hat{\mu}$), while
224 accounting for heterogeneity across experimental repeats **(Figure 2A, Methods)**. Latent space
225 distances provide a single-metric quantification of the response to perturbations. This approach
226 models both the sampling variance within repeats (uncertainty) and the heterogeneity across repeats
227 (random effect), allowing to statistically test whether an organelle is consistently affected
228 (reproducibility). Effects are presented in organelle scoring forest plots; organelles are ranked based
229 on their combined effect size and multiple hypothesis correction is applied.

To evaluate the ability of NOVA to detect organellar changes in response to perturbations we introduced sodium arsenite (0.5 mM, 30 minutes)[96,97], which leads to oxidative stress, into day 8 human iPSC-derived neurons (three experimental repeats, >590,600 images; **Supplementary Figure 10**). A mixed-effects meta-analysis, accounting for experimental repeat reproducibility, revealed substantial alterations in the topography of multiple organelles (**Figure 2B, C**). The largest combined effect size was of stress granules (SGs), cytoplasmic biomolecular condensates that are composed of RNA-binding proteins and RNAs that are formed in response to stress (marked by G3BP1; $\hat{\mu}$=0.703, adj. p=2.22 × 10^{-7}). A similar effect was observed for FMRP, which is localized in neurons into RNA-associated granules ("FMRP granules"), including SGs under stress[94]. However, strong heterogeneity driven by a single divergent experimental repeat limited statistical significance after FDR correction ($\hat{\mu}$=0.421, adj. p=0.074; heterogeneity: I^2=95.45, τ^2=0.126 (95% CI=[0.024,2.33]); **Figure 2B, C**). In addition, PURA granules effectively discriminated stressed from untreated neurons ($\hat{\mu}$=0.182, adj. p=1.98 × 10^{-4}, **Figure 2B, C**), consistent with their association with SGs[88,89]. Reproducible and significant stress-associated changes were also observed in the mitochondria ($\hat{\mu}$= 0.292, adj. p=9.87 × 10^{-5}), MOM ($\hat{\mu}$ = 0.213, adj. p=0.012), PML bodies ($\hat{\mu}$=0.223, adj. p=2.6e × 10^{-4}), P-bodies ($\hat{\mu}$=0.182, adj. p=0.007), and microtubules (μ=0.095, adj. p=9.35 × 10^{-5}; **Figure 2B, C**). We further implemented NOVA rollout attention maps to visualize image regions that most strongly influenced the model's output, highlighting areas of highest attention and enabling interpretation of the features driving NOVA's output (**Figure 2C, Methods**).

Altogether, we comprehensively characterize the changes that neuronal organelles undergo in response to oxidative stress, using a single-scale system. Organelle scoring is a unified system for organellar comparison that reassuringly detects known markers of the neuronal stress response and provides an overview of significant, reproducible perturbation effects on organelles across multiple experimental repeats.

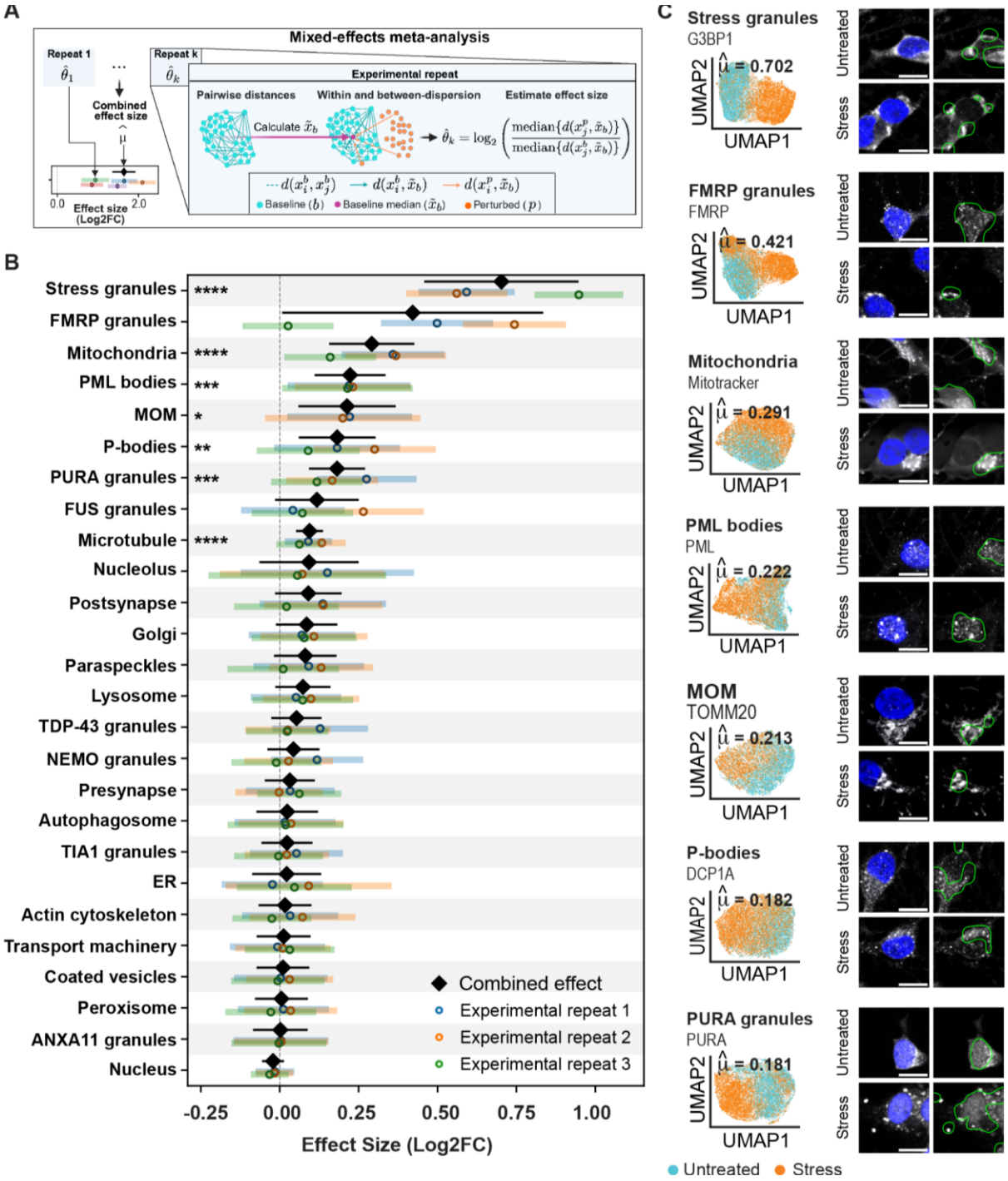
A
Mixed-effects meta-analysis
Repeat 1
Repeat k
Combined effect size
Effect size (Log2FC)
Experimental repeat
Pairwise distances
Within and between-dispersion
Estimate effect size
Calculate
Baseline (b)
Baseline median
Perturbed (p)
B
Stress granules
FMRP granules
Mitochondria
PML bodies
MOM
P-bodies
PURA granules
FUS granules
Microtubule
Nucleolus
Postsynapse
Golgi
Paraspeckles
Lysosome
TDP-43 granules
NEMO granules
Presynapse
Autophagosome
TIA1 granules
ER
Actin cytoskeleton
Transport machinery
Coated vesicles
Peroxisome
ANXA11 granules
Nucleus
Combined effect
Experimental repeat 1
Experimental repeat 2
Experimental repeat 3
-0.25
0.00
0.25
0.50
0.75
1.00
Effect Size (Log2FC)
C
Stress granules
G3BP1
FMRP granules
FMRP
Mitochondria
Mitotracker
PML bodies
PML
MOM
TOMM20
P-bodies
DCP1A
PURA granules
PURA
UMAP1
UMAP2
Untreated
Stress

255

256

Figure 2. Neuronal organelle response to oxidative stress in human neurons. (A) Overview of meta-analytic framework for perturbation effect size estimation. Effect size is defined as the shift in organelle topography (localization/morphology) under perturbation, quantified as the distance in NOVA embedding space between perturbed and baseline states. Effect sizes are computed independently per experimental repeat and integrated using mixed-effects meta-analysis, accounting for within- and between-repeat variance, yielding a combined estimate with confidence intervals that reflect biological and technical variability. **(B)** Stacked forest plot of organelle effect size (log2 fold change) in day 8 neurons in response to oxidative stress ($NaAsO_2$, 0.25 mM, 30 min), relative to untreated controls. Three experimental repeats. Colored dots represent the experimental repeat-wise effect estimate, with horizontal bars indicating the 95% CI variance within experimental repeats. The combined effect estimate ($\hat{\mu}$) is shown in black diamond with its 95% meta-analytic CI, which accounts for variance between experimental repeats when present. Adjusted p-value: * < 0.05, ** < 0.01, *** < 0.001, **** < 0.0001. ~800-2800 image tiles per condition/experimental repeat. **(C)** Joint UMAP projection of three experimental repeats, highlighting top organelles by combined effect size and FDR-corrected meta-analysis significance. Point - single image tile, ~7k images/condition. Untreated (blue) vs oxidative stress (orange). $\hat{\mu}$- the combined effect estimate. Representative images with nucleus (hoechst 33342) and overlaid model's attention maps. Lens ×63; scale bar, 10 µm.

An organellar response to ALS-associated single-nucleotide variants in neuron

The iPSC Neurodegenerative Disease Initiative (iNDI)[98] enables controlled comparison of different neurodegeneration-associated variants within a single isogenic background. We quantified the effects of ALS-associated genetic variants on neuronal organelles in iPSC-derived iNDI neurons. The ancestral isogenic control line (Knockout Laboratory F2.1 Jackson, KOLF, wild-type) was compared to four ALS-associated variants: *FUS* (Fused in Sarcoma) R495*[99,100], *TARDBP* (TAR DNA/RNA-Binding Protein 43; TDP-43) M337V[101,102], *OPTN* (Optineurin) Q398E[103], and *TBK1* (TANK Binding Kinase 1) E696K[104] (**Figure 3A**). We generated a neuronal imaging dataset consisting of six experimental repeats with 2 technical repeats each (~6,495,000 images post-QC, representing ~1,250,000 neurons captured in 2–4 channels; average 1.7 nuclei per tile; **Supplementary Figure 11** and **Supplementary Materials**). Neurons were stained with the 26 organelle markers initially used (**Table 1**) and three other markers that were used for inference only (SON (nuclear speckles), hnRNPA1 (hnRNP complex), and LSM14A (P-bodies).

Inference on the iNDI induced neurons dataset revealed diverse and significant organellar changes in ALS-associated variants relative to wild-type. Overall, a total of 19 organelles were affected in ALS-associated lines, relative to wild-type (WT) including FUS granules, lysosome, peroxisome, PURA granules, NEMO granules, presynapse, PML bodies, TIA1 granules, P-bodies (LSM14A, DCP1A), MOM, hnRNP complex (HNRNPA1), TDP-43 granules, ANXA11 granules, Golgi, ER, paraspeckles, microtubule (Tubulin), and postsynapse (**Figure 3B-F**). The effect size of FUS granules was the largest across all lines (*OPTN* Q398E ($\hat{\mu}$=0.709, adj.p=1.17 × 10^{-4}; heterogeneity: I^2=95.41%, τ^2=0.1217 (95% CI=[0.035,0.7738]))), *TBK1* E696K ($\hat{\mu}$=0.342, adj.p=1.1 × 10^{-3}; heterogeneity: I^2=83.47%, τ^2=0.0377 (95% CI=[0.0068,0.264])), *TARDBP* M337V ($\hat{\mu}$=0.247, adj.p=5.9 × 10^{-2}; heterogeneity: I^2=88.1%, τ^2=0.045 (95% CI=[0.01,0.311]; *FUS* R495* $\hat{\mu}$=1.352, adj. p=3.22 × 10^{-15}; heterogeneity: I^2=78.25%, τ^2=0.0142 (95% CI=[0.0019,0.1059]) **Figure 3B-E** and **Supplementary Figure 12**).

298 We also compared *FUS* 495* to the revertant line (REV), in which the variant had been
299 corrected by genome editing. The restoration of the wild-type *FUS* gene sequence was associated with
300 relocalization of the FUS protein into the nucleus (FUS granules,REV:$\hat{\mu}$=1.385, adj.p=6.4 × 10^{-15};
301 heterogeneity: I^2=87.96%, τ^2=0.0266 (95% CI=[0.0062,0.1801]); **Figure 3F,G**). Since the *FUS* 495*
302 variant disrupts FUS's steady-state nuclear localization and thereby reduces nuclear signal intensity,
303 the model's nuclear focus might suggest that it utilizes this loss of nuclear enrichment to distinguish
304 *FUS* 495* from the wild-type and revertant lines. Several other organelles showed significant
305 alterations in *FUS* R495* relative to both the wild-type (WT) and revertant (REV), namely, PURA
306 granules (WT: $\hat{\mu}$=0.139, adj.p=3.4 × 10^{-7}, REV: $\hat{\mu}$=0.152, adj.p=2.5 × 10^{-7}; **Figure 3E, F**), Peroxisomes
307 (WT: $\hat{\mu}$=0.199, adj.p=3.2 × 10^{-15}, REV: $\hat{\mu}$=0.139, adj.p=2.9 × 10^{-4}), lysosome (WT: $\hat{\mu}$=0.18, adj.p=5.44 ×
308 10^{-3}, REV: $\hat{\mu}$=0.09, adj.p=9.05 × 10^{-3}) and hnRNP complex (WT: $\hat{\mu}$=0.078, adj.p=2.25 × 10^{-2} REV: $\hat{\mu}$=0.27,
309 adj.p=2.72 × 10^{-2}; heterogeneity: I^2=88.33%, τ^2=0.074 (95% CI=[0.02,0.384])). These data underscore
310 a robust and reproducible modification across two different controls. Comparable analysis of the *FUS*
311 R495* heterozygous variant, is described in **Supplementary Figure 13**.

312 Additional organelles were altered across multiple lines: P-bodies, marked by LSM14A, altered
313 in response to variants *TBK1* E696K ($\hat{\mu}$=0.146, adj.p=2.8 × 10^{-5}), *OPTN* Q398E ($\hat{\mu}$=0.124, adj.p=1.2 ×
314 10^{-4}) and *TARDBP* M337V ($\hat{\mu}$=0.101, adj.p=5.8 × 10^{-3}; **Figure 3B-D**)), while DCP1A was also impacted
315 in both *TBK1* E696K ($\hat{\mu}$=0.109, adj.p=7 × 10^{-5}) and *OPTN* Q398E ($\hat{\mu}$=0.078, adj.p=3 × 10^{-3}); **Figure 3B-D**
316 and **Supplementary Figure 14**). Additionally, lysosomes were affected by variants in *TBK1* E696K
317 ($\hat{\mu}$=0.11, adj.p=1.3 × 10^{-2}), *OPTN* Q398E ($\hat{\mu}$=0.205, adj.p=3.8 × 10^{-3}; heterogeneity: I^2=74.22%,
318 τ^2=0.0179 (95% CI=[0.0028, 0.1143])) and *FUS* R495* ($\hat{\mu}$=0.18, adj.p=5.4 × 10^{-3}; (**Figure 3B-D and**
319 **Supplementary Figure 15**). NEMO granules altered by variants in *TARDBP* M337V (μ=0.107, adj.p=5.9
320 × 10^{-3}), *OPTN* Q398E (μ=0.103, adj.p=7.2 × 10^{-3}) and *TBK1* E696K ($\hat{\mu}$=0.105, adj.p=0.044; **Figure 3B-D**).
321 Notably, TDP-43 granules were unaffected by any of the variants, consistent with the absence of TDP-
322 43 proteinopathy in premature 8-day-old neurons [105].

323 Altogether, NOVA detected subtle yet reproducible changes associated with single nucleotide
324 changes, uncovering multiple organelles affected across different ALS-associated mutations, including
325 FUS granules and P-bodies. Together, these results provide a comprehensive view of shared and
326 distinct organellar alterations, underscoring the complexity of diverse organelles in ALS.

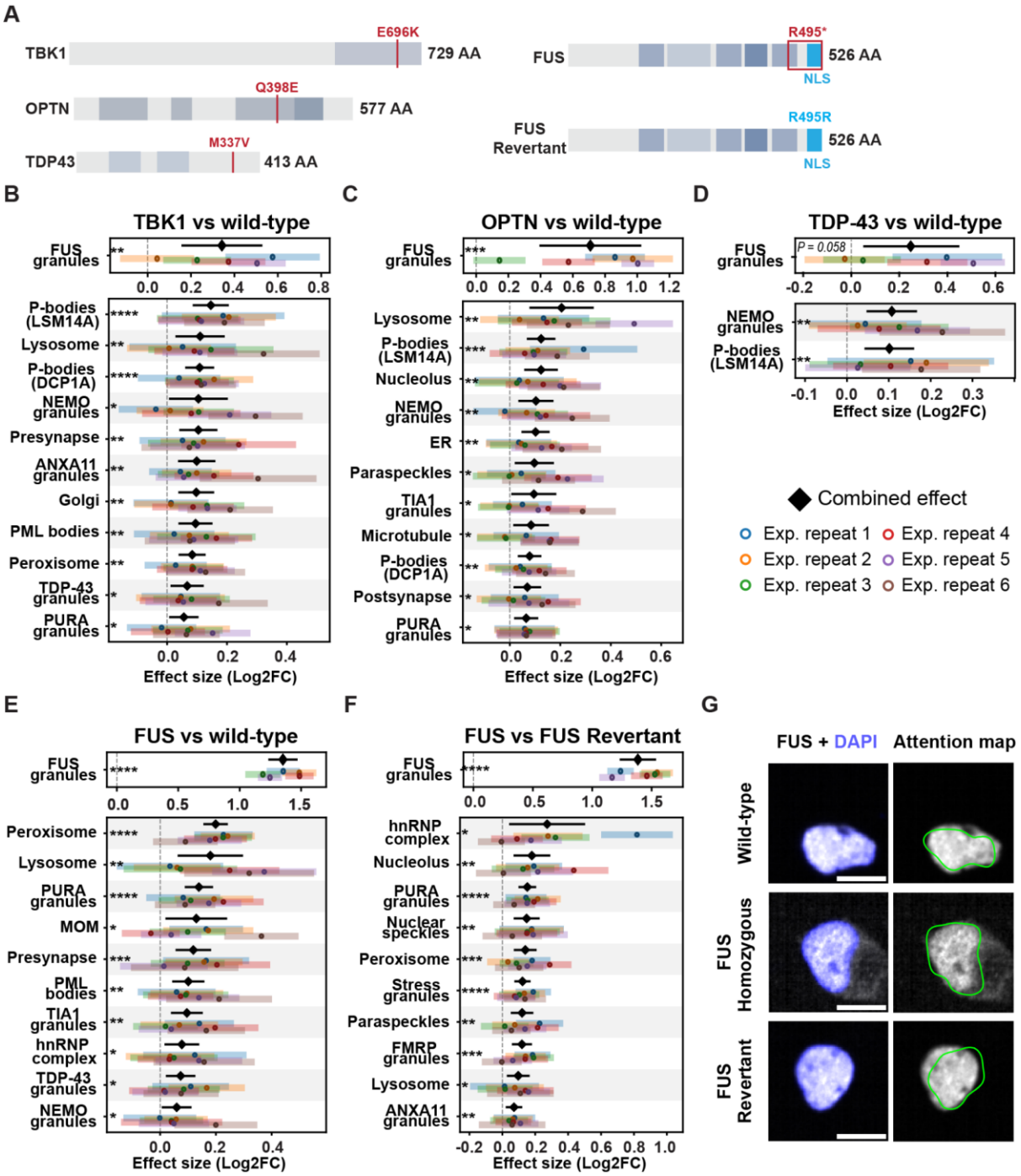
A
TBK1
E696K
729 AA
OPTN
Q398E
577 AA
TDP43
M337V
413 AA
FUS
R495*
526 AA
NLS
FUS Revertant
R495R
526 AA
NLS
B
TBK1 vs wild-type
FUS granules
P-bodies (LSM14A)
Lysosome
P-bodies (DCP1A)
NEMO granules
Presynapse
ANXA11 granules
Golgi
PML bodies
Peroxisome
TDP-43 granules
PURA granules
Effect size (Log2FC)
C
OPTN vs wild-type
FUS granules
Lysosome
P-bodies (LSM14A)
Nucleolus
NEMO granules
ER
Paraspeckles
TIA1 granules
Microtubule
P-bodies (DCP1A)
Postsynapse
PURA granules
Effect size (Log2FC)
D
TDP-43 vs wild-type
FUS granules
P = 0.058
NEMO granules
P-bodies (LSM14A)
Effect size (Log2FC)
Combined effect
Exp. repeat 1
Exp. repeat 2
Exp. repeat 3
Exp. repeat 4
Exp. repeat 5
Exp. repeat 6
E
FUS vs wild-type
FUS granules
Peroxisome
Lysosome
PURA granules
MOM
Presynapse
PML bodies
TIA1 granules
hnRNP complex
TDP-43 granules
NEMO granules
Effect size (Log2FC)
F
FUS vs FUS Revertant
FUS granules
hnRNP complex
Nucleolus
PURA granules
Nuclear speckles
Peroxisome
Stress granules
Paraspeckles
FMRP granules
Lysosome
ANXA11 granules
Effect size (Log2FC)
G
FUS + DAPI
Attention map
Wild-type
FUS Homozygous
FUS Revertant

327

328

329 **Figure 3. Neuronal organelle response to ALS-associated variants. (A)** ALS-associated variants and
330 genetically-corrected revertant for FUS variant (from stop codon at amino acid 495 to arginine; *495R)
331 from the iPSC Neurodegenerative Disease Initiative (iNDI) [98]. **(B-F)** Stacked forest plot of organelle
332 effect size (log2 fold change) in day 8 neurons harboring homozygous variants of **(B)** *TBK1*, **(C)** *OPTN*,
333 **(D)** *TARDBP* or **(E)** *FUS*, relative to wild-type control. **(F)** *FUS* homozygous variant relative to *FUS*
334 Revertant line. Six experimental repeats. 29 organelles studied. Only significant organelles are shown.
335 Colored dots represent the experimental repeat-wise effect estimate, with horizontal bars indicating
336 the 95% CI variance within experimental repeats. The combined effect estimate ($\hat{\mu}$) is shown in black
337 diamond with its 95% meta-analytic CI, which accounts for variance between experimental repeats
338 when present. Adjusted p-value: * < 0.05, ** < 0.01, *** < 0.001, **** < 0.0001. ~620-6800 image tiles
339 per organelle/variant/experimental repeat. **(G)** Representative images of *FUS* allelic series with
340 nucleus (hoechst 33342) and overlaid model's attention maps. Lens ×63; scale bar, 10 µm

341 **Cytoplasmic TDP-43 interacts with P-bodies and affect their functions**

342 We next focused on TDP-43 cytoplasmic mislocalization, a hallmark of ALS and frontotemporal
343 dementia (FTD) pathology [106–108]. To this end, we used human iPSC-derived neurons overexpressing
344 doxycycline-inducible TDP-43 (*TARDBP*) lacking a functional nuclear localization signal (NLS; TDP-
345 $43^{\Delta NLS}$), which is therefore restricted to the cytoplasm **(Figure 4A)**. Notably, TDP-$43^{\Delta NLS}$ expression was
346 minimal without doxycycline and, upon induction, reached ectopic levels ~3-fold higher than
347 endogenous TDP-43 (**** < 0.0001, One-way ANOVA with Benferroni's multiple comparison test,
348 **Supplementary Figure 16**). Induction of TDP-$43^{\Delta NLS}$ by doxycycline (+DOX) increased cytoplasmic TDP-
349 43 relative to nuclear TDP-43 by ~10-fold compared to the uninduced condition (-DOX; β = 0.55, p <
350 0.0001, (95% CI [0.54, 0.56]), fixed-effect fallback used, **Figure 4B**).

351 We generated a dataset of TDP-$43^{\Delta NLS}$ neuron images across five experimental repeats (three
352 technical repeats each) stained for 29 organelles (~1,192,600 images post-QC, **Table 1**, **Supplementary**
353 **Figure 17**). This line, unseen during training, was stained with the 26 organelle markers initially used
354 (**Table 1**) and three other markers that were used for inference only (SON (nuclear speckles), hnRNPA1
355 (hnRNP complex), and LSM14A (P-bodies).

356 As could be expected, the topography of TDP-43 granules was the most affected by the TDP-
357 $43^{\Delta NLS}$, relative to uninduced state ($\hat{\mu}$=0.693, adj. p=6.4×10^{-15}; (95% CI=[0.626,0.76]), **Figure 4C, D**). P-
358 bodies and PML nuclear bodies, two principal membraneless organelles that regulate nucleic acids in
359 the cytoplasm and nucleus, respectively, also displayed significant topographic changes (P-bodies
360 (LSM14A): $\hat{\mu}$=0.457, adj. p=0.0001; heterogeneity: I^2=67.64, τ^2=0.032 (95% CI = [0.24, 0.675]); P-bodies
361 (DCP1A): $\hat{\mu}$=0.155, adj. p=7.11×10^{-5}; (95% CI = [0.085, 0.226]); PML nuclear bodies (PML): $\hat{\mu}$=0.217,
362 adj. p=3.7×10^{-8}; (95% CI = [0.144, 0.289]); **Figure 4C,E**).

363 PML nuclear bodies regulate TDP-43 homeostasis and may accordingly be affected by TDP-43
364 overexpression [109,110]. No discernible changes were identified in several other organelles, including
365 stress granules markers (G3BP1, FMRP, and PURA; **Supplementary Figure 18A**), consistent with
366 previous reports that cytosolic TDP-43 assemblies operate separately from conventional stress
367 granules [111].

368 P-body topography changes were depicted with two independent markers (LSM14A and
369 DCP1A). To further investigate the hypothesis that TDP-43 granules interact with P-bodies, we
370 demonstrated that colocalization of P-bodies with TDP-43$^{\Delta NLS}$ (measured as the percent of TDP-43$^{\Delta NLS}$
371 signal inside P-bodies; **Supplementary Figure 18B**) was significantly greater in TDP-43$^{\Delta NLS}$ neurons than
372 expected by chance under spatial randomization (mean real fraction overlap 0.170 vs. 0.047 in
373 rotated; Wilcoxon signed-rank test, ****$p < 0.0001$; three experimental repeats, four technical
374 repeats each, ~200 imaging sites per condition; **Figure 4F**).

375 Next, using SpeedPPI, a machine-learning algorithm for structure-based protein-protein
376 interaction prediction [112–114], we tested whether P-body-enriched proteins are predicted to physically
377 interact with TDP-43. We analyzed proteins that were co-immunoprecipitated with the P-body protein
378 DDX6 [115] and were either enriched (n=20 proteins), or depleted (n=18 proteins) in P-bodies by
379 unbiased mass spectrometry [116]. The predicted interactions of the enriched P-body proteins with TDP-
380 43 were significantly stronger than those of the group of proteins highly depleted from P-bodies
381 (average pDockQ score = 0.3334 vs. 0.2058; $p = 0.0112$; Mann–Whitney U test; **Supplementary Figure**
382 **18C** and **Supplementary Materials**), supporting the specificity of these predicted interactions with
383 TDP-43.

384 We further characterized the proteome in the vicinity of cytoplasmic TDP-43 using engineered
385 ascorbate peroxidase (APEX) proximity labeling and mass spectrometry. APEX uses hydrogen peroxide
386 (H2O2), to generate reactive biotin radicals that label nearby biomolecules, revealing weak or
387 transient interactions and enabling characterization of cellular compartments at nanometer
388 resolution [117–119]. An APEX peptide fused to TDP-43$^{\Delta NLS}$ or to NES constructs in frame, demonstrated
389 specificity by immunostaining. The biotinylated signal was observed only when both H2O2 and biotin
390 phenol (BP) were present in the medium and overlapped with construct localization **(Supplementary**
391 **Figure 19A)**. This provides a reliable framework to capture cytoplasmic TDP-43 interactions and enable
392 proteomic mapping of its cytoplasmic environment.

393 Following proximity labeling, biotinylated proteins were pulled down with streptavidin beads
394 and analyzed by mass spectrometry (MS) in two independent experiments (3-4 technical repeats per
395 condition each). In total, 212 proteins interacted specifically with TDP-43$^{\Delta NLS}$ relative to the NES control
396 in both experiments (FDR < 0.01, log2FC > 2, unpaired two-sided t-test). TDP-43 itself was reassuringly
397 among the most enriched proteins (13-fold and 38-fold relative to NES, respectively; **Figure 4G,**
398 **Supplementary Figure 19B, Supplementary Materials**). Gene Ontology (GO) cellular component
399 analysis [120,121] revealed strong enrichment of "P-body" proteins (fold enrichment = 4.32, FDR < 0.01;
400 **Supplementary Figure 19C**) as well as RNA-induced silencing complex (RISC)/RNAi effector complex
401 proteins, which often localize to P-bodies and share overlapping functions in mRNA silencing [122,123].
402 We further validated 10 P-body-enriched proteins [116] (AGO1, AGO2, DCP1A, DCP2, EIF4ENIF1, LSM14A,
403 MCM7, MSI1, SMG7, YTHDC2) as TDP-43$^{\Delta NLS}$ interactors in an independent targeted MS experiment,
404 whereas five housekeeping proteins (obtained from the proteomic data, VDAC1, RPAB1, GDIA, RL10A,
405 TBA1A) were not significantly enriched (unpaired two-sided t-test; **Figure 4H, Supplementary**
406 **Materials**).

407 P-bodies are dynamic, phase-separated condensates, and their fluidity directly influences
408 cellular processes [124,125]. We hypothesized that cytoplasmic TDP-43 disrupts P-body function as
409 indicated by P-body size (average radius). P-body size was significantly reduced in cultured neurons

410 upon induction of TDP-43$^{\Delta NLS}$ (LSM14A: β = −0.0247, p < 0.0001, (95% CI [−0.03, −0.02]); DCP1A: β =
411 −0.0566, p < 0.0001, (95% CI [−0.059, −0.052]); fixed-effect fallback used, **Figure 4I-J**). Effects were
412 estimated with a linear mixed-effects model (DOX treatment as a fixed effect, experimental repeat as
413 a random intercept). Notably, wild-type TDP-43 overexpression (containing functional NLS) in day 8
414 neurons, caused a slight increase in P-body size with ten-fold smaller effect size compared to the
415 induction of TDP-43$^{\Delta NLS}$ (TDP-43$^{\Delta NLS}$: β = -0.032, p < 0.0001, (95% CI: [-0.04, -0.03]); TDP-43^{WT}: β = 0.003,
416 p = 0.025, (95% CI: [0.00, 0.01])), **Supplementary Figure 20)**, suggesting that TDP-43 mislocalization
417 drives the observed P-body alterations.

418 Reduced fluidity of biomolecular condensates and a shift toward more solid-like states is a
419 process linked to neurodegenerative diseases including ALS. To test whether cytoplasmic TDP-43
420 impacts P-body diffusion dynamics, we used partial fluorescence recovery after photobleaching
421 (FRAP). In U2OS cells constitutively expressing YFP-DCP1A and transfected with inducible TDP-43$^{\Delta NLS}$,
422 induction of cytoplasmic TDP-43 significantly delayed internal diffusion of YFP-DCP1A within P-bodies,
423 relative to uninduced controls (p < 0.001, Two-way ANOVA with repeated measures and Geisser–
424 Greenhouse correction; **Figure 4K**, **Supplementary Figure 21A, B**). In contrast, induction of the NES
425 control peptide did not significantly affect P-body dynamics **(Supplementary Figure 21C–E)**. These
426 results suggest that cytoplasmic TDP-43 reduces P-body liquidity.

427 We also evaluated the effect of mislocalized cytoplasmic TDP-43 on P-bodies in orthogonal
428 model systems. In U2OS cells expressing clover-tagged TDP-43$^{\Delta NLS}$, cytoplasmic TDP-43 altered P-body
429 size (unpaired t-test, p < 0.0001, **Supplementary Figure 21F**). Notably, this effect was observed only
430 under oxidative stress conditions (0.25 M sodium arsenite, 30 min) and during a subsequent 60-
431 minute recovery period, but not under basal (pre-stress) conditions. This likely reflects a previously
432 reported phenomenon in this cellular model, in which oxidative stress induces the formation of toxic,
433 SG-independent cytoplasmic TDP-43 foci [126].

434 A similar effect was demonstrated in wild type iPSC-derived neurons, where cytoplasmic
435 mislocalization of endogenous TDP-43 was triggered by osmotic stress [127,128] (sorbitol 0.4 M, 2 hr;
436 **Supplementary Figure 21G**). Consistently, under sorbitol-induced cytoplasmic TDP-43 conditions,
437 DCP1A-containing P-bodies were significantly smaller (β = −0.0327, p < 0.0001, (95% CI [−0.033,
438 −0.031]), fixed effect fallback used), whereas LSM14A-containing P-bodies were not significantly
439 affected (**Supplementary Figure 21H**). Taken together, these results support interaction between
440 mislocalized cytoplasmic TDP-43 and P-bodies that alter P-body properties, suggesting a role for P-
441 bodies in ALS and FTD that was not shown previously.

442 Although P-body function is still highly debated, P-bodies seem to play a role in RNA storage
443 and decay [129]. Thus, we assessed the changes to RNA half-life in response to TDP-43$^{\Delta NLS}$ expression in
444 neurons using the incorporation of 4-thiouridine (4sU; 200 µM) into newly transcribed RNA molecules
445 (2 or 3 hours labeling pulse), followed by SLAM-seq and GRAND-SLAM analysis [130–132](**Figure 4L,**
446 **Supplementary Materials**). Induction of TDP-43$^{\Delta NLS}$ caused a 10% reduction in global RNA half-life,
447 relative to uninduced control (p-value < 0.0001, Mann–Whitney U test; **Figure 4M**). This reduction in
448 mRNA stability increased to 30% when analyzing mRNAs that are enriched inside P-bodies [116] (p-value
449 < 0.0001, Mann–Whitney U test; **Figure 4N**). In contrast, there was a milder 5% decrease in the half-
450 life of RNAs not specifically enriched in P-bodies (p-value < 0.01, Mann–Whitney U test; **Figure 4O**).
451 Therefore, accelerated mRNA decay is caused by cytoplasmic TDP-43 malposition and is specific to

452 mRNAs that reside within P-bodies. Overall, we conclude that cytoplasmic TDP-43 directly interacts
453 with P-bodies, and disrupts their biophysical properties and functions. This suggests a potential role
454 of P-bodies in the molecular mechanisms underlying TDP-43 proteinopathy and neurodegeneration.

455

Figure 4. Cytoplasmic TDP-43 overexpression interacts with neuronal P-bodies, altering their function. (A) Diagram and representative images of day 8 neurons expressing doxycycline-inducible TDP-43 with a mutated nuclear localization signal (TDP-43$^{\Delta NLS}$; -DOX uninduced, +DOX induced). Lens ×63; scale bar, 5 µm. **(B)** Boxplots of cytoplasmic-to-nuclear TDP-43 signal ratios in TDP-43$^{\Delta NLS}$ neurons ±DOX induction (means = 0.064 (-DOX) vs. 0.615 (+DOX)). Colored dots represent experimental repeat means; gray dots - individual site images. ****p < 0.0001. Linear model with DOX as a fixed effect and experimental repeat as a covariate; random-effect variance estimated as 0. **(C)** Stacked forest plot of organelle effect sizes (log2 fold change) in day 8 TDP-43$^{\Delta NLS}$ neurons +DOX, relative to -DOX. Five experimental repeats. 29 organelles. Colored dots represent the experimental repeat effect estimate, with horizontal bars indicating the 95% CI within-experimental repeat variance. The combined effect estimate ($\hat{\mu}$) is shown in black diamond with its 95% meta-analytic CI, which accounts for between-experimental repeat variance when present. Adjusted p-value: * < 0.05, ** < 0.01, *** < 0.001, **** < 0.0001. Only significant organelles are shown. ~280-6200 image tiles per organelle/condition/experimental repeat. Joint UMAP projection of five experimental repeats showing **(D)** TDP-43 granules (image tiles: 12,530 +DOX; ~8,500 -DOX) and **(E)** P-bodies stained with LSM14A (left, image tiles: 9,510 +DOX; ~8,580 -DOX) or DCP1A (right, image tiles: ~8,610 +DOX; ~9,690 -DOX). Neurons -DOX/+DOX (green/ purple). Points - single image tiles. $\hat{\mu}$- the combined effect estimate. Representative images with nucleus (hoechst 33342) or overlayed model's attention maps. Lens ×63; scale bar, 10 µm. **(F)** Boxplots of P-body-positive (DCP1A) pixels that are also positive for TDP-43 (V5 tag). Colocalization fraction in real images vs. randomized (rotated) images (mean fraction overlap = 0.170 vs. 0.047, respectively). ~1,800 site images; Wilcoxon signed-rank test, ****p < 0.0001. Blue dots - condition means; Gray dots - individual images; three experimental repeats of day 8 induced neurons. **(G)** Volcano plots of relative protein levels in induced APEX-TDP-43$^{\Delta NLS}$ relative to APEX-NES samples (x axis log2 scale), analyzed by mass spectrometry. y axis depicts the differential expression p values (−log10 scale). One of two independent experiments; 3-4 technical repeats per condition. TDP-43 (red) and selected P-body proteins (from ref.[116], blue). Unpaired two-sided t-test. **(H)** Normalized enrichment of P-body proteins (AGO1, AGO2, DCP1A, DCP2, EIF4ENIF1, LSM14A, MCM7, MSI1, SMG7, YTHDC2) and housekeeping proteins (VDAC1, RPAB1, GDIA, RL10A, TBA1A) in the vicinity of TDP-43$^{\Delta NLS}$ vs. NES control, analyzed by targeted mass spectrometry. Unpaired two-sided t-test. CellProfiler quantification of P-body size in monoclonal TDP-43$^{\Delta NLS}$ neurons (-DOX vs. +DOX) stained by P-body markers: **(I)** LSM14A or **(J)** DCP1A (means (-DOX vs. +DOX) = 1.70 vs. 1.68 or 1.51 vs. 1.46, respectively). Colored dots - experimental repeat means; gray dots - site-level measurements. Five experimental repeats per condition. Linear mixed-effects model with DOX as a fixed effect and experimental repeat as a random intercept; fixed-effects fallback used when variance was zero. ****p < 0.0001. **(K)** Live imaging of fluorescence recovery after photobleaching (FRAP) of YFP-DCP1A in P-bodies. U2OS cells with or without DOX-induced TDP-43$^{\Delta NLS}$, normalized to pre-bleaching baseline. Images depict a single P-body; scale bar, 1 µm. Four repeats with 3-5 fields of view and 2-9 P-bodies per field. Two-way ANOVA with repeated measures and Geisser-Greenhouse correction. *** P < 0.001 **(L)** Schematic of the SLAM-seq approach for measuring RNA half-life through incorporation of 4-thiouridine (4sU; 200 µM) into newly transcribed RNA molecules [130]. GRAND-SLAM[131] RNA half-life estimates from 0, 2, and 3 h of 4-thiouridine labeling: **(M)** all mRNAs, **(N)** P-body–enriched mRNAs or **(O)** P-body-depleted mRNAs. Dots = individual transcripts; 2–4 technical repeats per timepoint. Mean ± 95% CI. Whiskers - SD. Mann–Whitney U test, P-value: * < 0.05, ** < 0.01, *** < 0.001, **** < 0.0001, ns = not significant.

500 **TDP-43 and P-bodies in ALS patient-derived iPSC neurons and post-mortem tissues**

501 We tested NOVA's ability to identify neuronal phenotypes (ALS vs. healthy human subjects) in
502 patient-derived neurons that were not previously seen by the model. We differentiated iPSCs from a
503 cohort of 21 subjects into day 60 motor neurons [105,133], including healthy controls (n=6, 3 males, 3
504 females), *C9orf72*-ALS patients (C9ALS, n=3, 2 males, 1 female), two sporadic ALS patients without
505 cytoplasmic TDP-43 (sALS-, n=2, 1 male, 1 female), and ten sporadic ALS patients with cytoplasmic
506 TDP-43 (sALS+, n=10, 6 males, 4 females). This cohort (~9,160 image tiles post-QC) was
507 immunofluorescently stained for 4 organellar markers: TDP-43 granules, P-bodies (DCP1A), nucleus
508 (Hoechst 33342) and microtubule (MAP2; **Figure 5A**). Lines derived from different human subjects are
509 defined as experimental repeats, in accordance with the MDAR (Materials Design Analysis Reporting)
510 framework guidelines [134].

511 C9ALS and sALS+ patient groups showed a significant increase in cytoplasmic-to-nuclear TDP-
512 43 signal ratios, relative to healthy controls (C9ALS: $\beta = 0.276$, $p < 0.0001$ (95% CI [0.1749, 0.3776]);
513 sALS+: $\beta = 0.1598$, $p < 0.0001$, (95% CI: [0.1103, 0.2092]); fixed-effect with human subject-clustered
514 standard errors, **Figure 5B**).

515 UMAP projection of NOVA-derived embeddings displayed group-specific topography of TDP-
516 43 granules and P-bodies (**Figure 5C, D,** C9ALS: $\hat{\theta}$=1.26; sALS-: $\hat{\theta}$=0.73; sALS+: $\hat{\theta}$=0.62; C9ALS: $\hat{\theta}$=1.29;
517 sALS-: $\hat{\theta}$=0.73; sALS+: $\hat{\theta}$=0.49, respectively, adj. p<0.05; permutation test, 100 iterations). These
518 clusters are also reflected in the pairwise Euclidean distances computed on the NOVA-derived
519 embeddings between pairs of human subjects (**Supplementary Figure 22A, B**). Surprisingly,
520 subclusters could be observed in UMAPs of nucleus and microtubule topography with significant effect
521 sizes as well (C9ALS: $\hat{\theta}$=1.39; sALS-: $\hat{\theta}$=0.77; sALS+: $\hat{\theta}$=0.41; C9ALS: $\hat{\theta}$=1.24; sALS-: $\hat{\theta}$=0.71; sALS+:
522 $\hat{\theta}$=0.44, respectively, adj. p<0.05; permutation test, 100 iterations; **Supplementary Figure 22C-F**).
523 Furthermore, colocalization of P-bodies with TDP-43 was significantly greater than expected in C9ALS
524 patients and in patients with cytoplasmic TDP-43 (C9ALS: $\beta = 0.063$, $p < 0.001$, (95% CI [0.026, 0.1]);
525 sALS+: $\beta = 0.188$, $p < 0.0001$, (95% CI [0.113, 0.263]); linear fixed-effects model with patient-clustered
526 standard errors, fallback used; **Supplementary Figure 22G**). Therefore, NOVA detects organellar
527 changes in patient-derived neurons, despite being trained solely on isogenic iNDI lines.

528 Next, we generated another dataset of day 60 neurons (n=12, three subjects per human
529 subject group, **Figure 5E**), stained for 32 organelles (~58K tile images post-QC). This dataset included
530 ten markers not seen in training: NUP62, NUP98 and NUP153 (nuclear pore complex), Lamin B1
531 (nuclear envelope), TIA1 (stress granules), EEA1 (early endosomes), hnRNPA1 and hnRNPA2B1 (hnRNP
532 complex), calnexin (ER) and MAP2 (microtubule). Similarly to the first cohort, C9ALS and sALS+ patient
533 groups showed a significant increase in cytoplasmic-to-nuclear TDP-43 signal ratios, relative to healthy
534 controls (C9ALS: $\beta = 0.315$, $p < 0.0001$ (95% CI [0.24012, 0.38942]); sALS+: $\beta = 0.321$, $p < 0.0001$, (95%
535 CI: [0.24591, 0.39521]); linear mixed-effects model, **Figure 5F**). Consistent with the previous cohort,
536 TDP-43 granules and P-bodies UMAPs displayed group-specific topographies (mixed-effect meta
537 analysis: C9ALS: $\hat{\mu}$=1.04, adj. p=1.98×10^{-14}; sALS-: $\hat{\mu}$=0.84, adj. p=4.26×10^{-9}; sALS+: $\hat{\mu}$=0.81, adj. p=6.6
538 $\times 10^{-8}$; C9ALS: $\hat{\mu}$=0.96, adj. p=1.98×10^{-8}; sALS-: $\hat{\mu}$=0.59, adj. p=8.22×10^{-4}; sALS+: $\hat{\mu}$=0.54, adj. p=7.22
539 $\times 10^{-2}$, respectively; mixed effects. **Figure 5G, H**), with C9ALS forming a distinct community with a mean

intra-community distance of d=0.02 (TDP-43 granules) and d=0.007 (P-bodies) based on pairwise Euclidean distance between human subjects (**Supplementary Figure 23**).

Meta-analytic effect sizes of all 32 organelles were quantified, relative to control, for C9ALS (**Figure 5I** and **Supplementary Figure 24A**); sALS+, sALS- (**Supplementary Figure 24B, C**). In C9ALS patients, 29 organellar markers displayed a change in topography that is significantly different from the controls (**Figure 5I**). Unexpectedly, the effect size of nine organelles was larger than that of TDP-43 granules (early endosomes ($\hat{\mu}$=1.8, adj. p=5.33 × 10^{-15}), Golgi ($\hat{\mu}$=1.64, adj. p=2.93 × 10^{-14}), nucleolus ($\hat{\mu}$=1.44, adj. p=3.78 × 10^{-3}; heterogeneity: I^2=82.49%, τ^2=0.5422 (95% CI=[0.0369,11.71])), lysosome ($\hat{\mu}$=1.28, adj. p=5.33 × 10^{-15}), coated vesicles ($\hat{\mu}$=1.2, adj. p=6.4 × 10^{-15}), NEMO granules ($\hat{\mu}$=1.13, adj. p=5.33 × 10^{-15}), actin cytoskeleton ($\hat{\mu}$=1.13, adj. p=4.76 × 10^{-8}), NPC ($\hat{\mu}$=1.12, adj. p=1.32 × 10^{-3}), and ER ($\hat{\mu}$=1.09, adj. p=5.33 × 10^{-15}), **Supplementary Figure 24D**). These findings may imply a change in autophagy and endosomal–lysosomal pathways in C9ALS. [135,136]

To investigate whether patient-derived neurons reflect the suggested crosstalk between TDP-43 and P-bodies, we modeled the fraction of TDP-43 overlap with P-bodies using a linear fixed-effects model with human subject-clustered standard errors (fallback used). Relative to healthy controls, colocalization was significantly increased in C9ALS patients (β = 0.305, p < 0.0001, (95% CI [0.27, 0.34]; **Figure 5J**) and sALS+ patients (β = 0.304, p < 0.0001, (95% CI [0.18, 0.42]); fixed effect fallback used). In contrast, sALS- patients did not differ significantly from controls (β = 0.001, p = 0.94) as expected given the absence of TDP-43 mislocalisation. In addition, P-bodies were significantly smaller in C9ALS patients and showed a near significant reduction in sALS+ patients relative to controls (C9ALS: β = -0.0157, p < 0.0001, (95% CI [-0.0223, -0.009]); sALS+: β = -0.0102, p = 0.051, (95% CI [-0.020, 0.00006]); fixed-effects with patient-clustered standard errors, **Figure 5K**)

Finally, we assessed the relevance of TDP-43-P-body crosstalk in ALS pathology, characterized by cytoplasmic TDP-43 aggregates [137,138]. Approximately 10-60% of the puncta area that was positive for either P-body protein DCP1A or LSM14A colocalized with TDP-43-specific RNA aptamer[139] and colocalization was evident in 46-100% of the neurons in C9ALS post-mortem motor cortices (four human subjects, **Figure 5L,M** and **Supplementary Figure 25A, B**). In C9ALS post-mortem tissue, cells contained a significantly lower number of puncta containing P-body proteins (DCP1A, LSM14A, or AGO2) compared to non-neurological controls (Mann-Whitney U test, p < 0.05). In contrast, puncta area size was significantly increased for LSM14A and DCP1A, but not for AGO2 (Mann-Whitney U test, p < 0.05, **Supplementary Figure 25C-I**). Furthermore, analysis of neurons with and without TDP-43 mislocalisation to the cytoplasm (-/+ cytoplasmic TDP-43) in C9ALS post-mortem tissues, revealed a significantly lower number of puncta containing LSM14A or DCP1A in the presence of mislocalised TDP-43 (nested t-test, p < 0.01, **Supplementary Figure 25J-K**), and significantly increased P-body area size (nested t-test, p < 0.05, **Supplementary Figure 25L-M**). This indicates that these properties are directly affected by cytoplasmic TDP-43. Intriguingly, large intra-neuronal and extracellular LSM14A-positive bodies were evident in C9ALS and sporadic ALS (sALS) brains, which were nearly absent in control tissues (10 controls, 6 C9ALS, 6 sAS; Kruska-Wallis test with Dunn's multiple comparisons test, adj. P-value for intra-neuronal bodies = 0.0006 or 0.0034; and for extracellular bodies = 0.0001 or 0.0182, C9ALS or sALS vs. controls, respectively; **Figure 5N-P**). Thus, TDP-43 pathology is associated with altered distribution of typical P-body markers.

581 Since cytoplasmic TDP-43 affects mRNA decay in cultured neurons, we sought supporting
582 evidence in neuropathology. We analyzed RNA-seq data from post-mortem neuronal *C9orf72* nuclei
583 that were sorted based on their TDP-43 content [140]. Nuclei exhibiting a loss of TDP-43 had more severe
584 downregulation of P-body-enriched mRNAs relative to P-body-depleted mRNAs. In two out of five
585 patients, this increase in the proportion of downregulated P-body mRNAs was statistically significant,
586 as well as the overall effect across patients (Cochran-Mantel-Haenszel test < 0.0001, **Figure 5Q**). These
587 data are consistent with altered RNA metabolism in TDP-43–deficient neurons. Therefore, accelerated
588 mRNA decay is associated with cytoplasmic TDP-43 malposition and is specific to mRNAs that reside
589 in P-bodies.

590 Together, cytoplasmic TDP-43 crosstalks with P-bodies, disrupting their biophysical properties
591 and function, proposing a role for P-bodies in the molecular mechanisms underlying TDP-43
592 proteinopathy and neurodegeneration (**Figure 5R**).

593

594

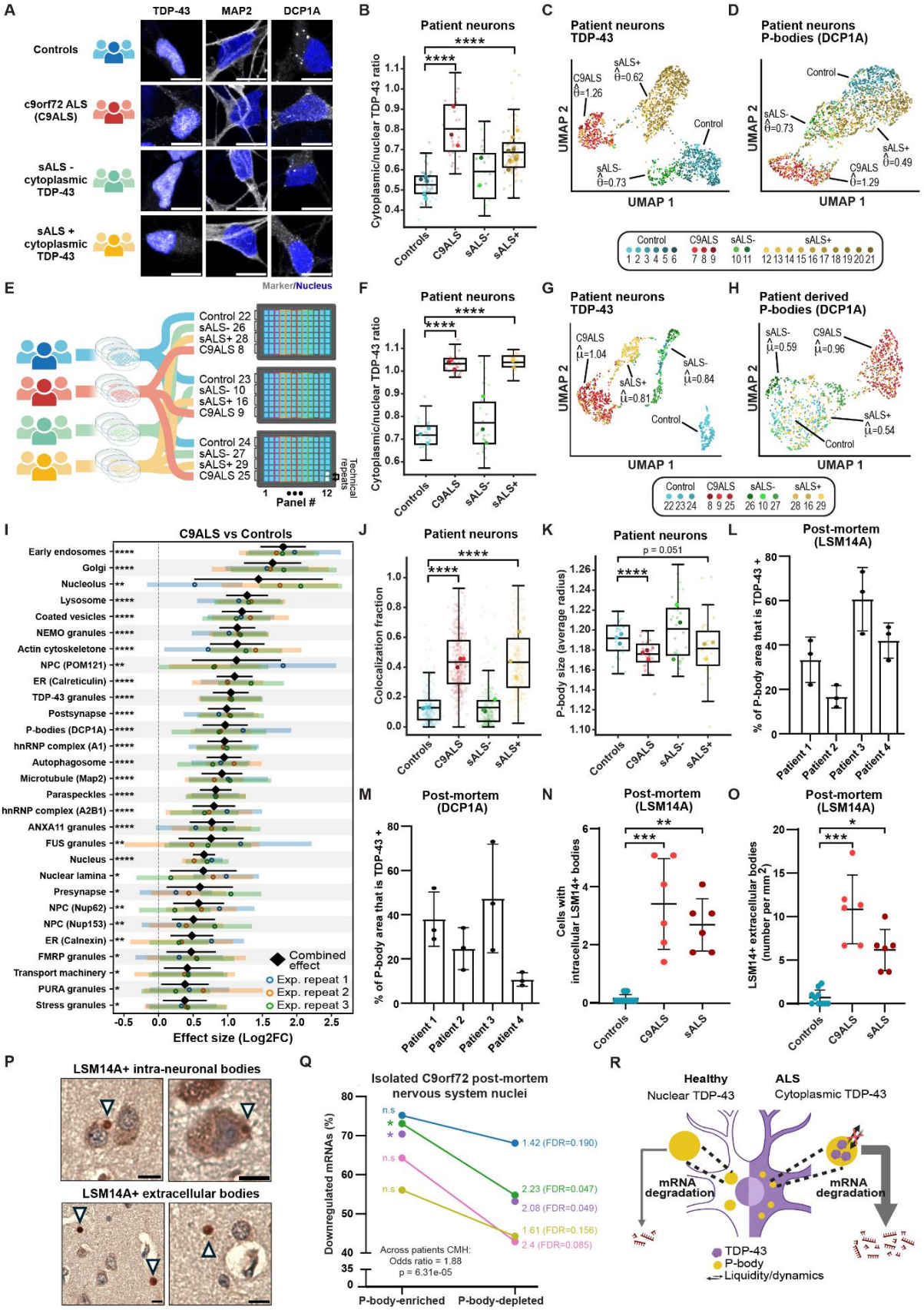
A
TDP-43
MAP2
DCP1A
Controls
c9orf72 ALS (C9ALS)
sALS - cytoplasmic TDP-43
sALS + cytoplasmic TDP-43
Marker/Nucleus
B
Patient neurons
Cytoplasmic/nuclear TDP-43 ratio
Controls
C9ALS
sALS-
sALS+
C
Patient neurons TDP-43
UMAP 1
UMAP 2
Control
D
Patient neurons P-bodies (DCP1A)
E
Control 22
sALS- 26
sALS+ 28
C9ALS 8
Control 23
sALS- 10
sALS+ 16
C9ALS 9
Control 24
sALS- 27
sALS+ 29
C9ALS 25
Technical repeats
Panel #
F
Patient neurons
G
Patient neurons TDP-43
H
Patient derived P-bodies (DCP1A)
I
C9ALS vs Controls
Early endosomes
Golgi
Nucleolus
Lysosome
Coated vesicles
NEMO granules
Actin cytoskeletone
NPC (POM121)
ER (Calreticulin)
TDP-43 granules
Postsynapse
P-bodies (DCP1A)
hnRNP complex (A1)
Autophagosome
Microtubule (Map2)
Paraspeckles
hnRNP complex (A2B1)
ANXA11 granules
FUS granules
Nucleus
Nuclear lamina
Presynapse
NPC (Nup62)
NPC (Nup153)
ER (Calnexin)
FMRP granules
Transport machinery
PURA granules
Stress granules
Combined effect
Exp. repeat 1
Exp. repeat 2
Exp. repeat 3
Effect size (Log2FC)
J
Patient neurons
Colocalization fraction
K
Patient neurons
P-body size (average radius)
p = 0.051
L
Post-mortem (LSM14A)
% of P-body area that is TDP-43 +
Patient 1
Patient 2
Patient 3
Patient 4
M
Post-mortem (DCP1A)
N
Post-mortem (LSM14A)
Cells with intracellular LSM14+ bodies
O
Post-mortem (LSM14A)
LSM14+ extracellular bodies (number per mm2)
P
LSM14A+ intra-neuronal bodies
LSM14A+ extracellular bodies
Q
Isolated C9orf72 post-mortem nervous system nuclei
Downregulated mRNAs (%)
1.42 (FDR=0.190)
2.23 (FDR=0.047)
2.08 (FDR=0.049)
1.61 (FDR=0.156)
2.4 (FDR=0.085)
Across patients CMH:
Odds ratio = 1.88
p = 6.31e-05
P-body-enriched
P-body-depleted
R
Healthy
Nuclear TDP-43
ALS
Cytoplasmic TDP-43
mRNA degradation
TDP-43
P-body
Liquidity/dynamics

595

Figure 5. Cytoplasmic TDP-43 and P-body function in ALS patient-derived iPSC neurons and post-mortem tissues. (A) Representative images of TDP-43 granules (green), Cytoskeleton (red), P-bodies (magenta), and nucleus (blue) in day 60 iPSC-derived motor neurons from human subjects. Healthy control (blue, n=6), *C9orf72*-ALS (C9ALS, red, n=3), sporadic ALS (sALS) without cytoplasmic TDP-43 (sALS-, green, n=2), or sALS with cytoplasmic TDP-43 (sALS+, yellow, n=10). Lines derived from different human subjects are defined as experimental repeats, in accordance with the MDAR (Materials Design Analysis Reporting) framework guidelines[134]. Scale bar - 10 µm. **(B)** Boxplots of cytoplasmic-to-nuclear TDP-43 signal ratios in C9ALS, sALS- or sALS+ vs. healthy controls (means: 0.802, 0.591 or 0.686 vs. 0.526, respectively). **** $p < 0.0001$. Linear fixed-effects model with human subject-clustered standard errors (fallback used). Joint UMAP projection of day 60 motor neurons from a cohort of 21 human subjects, showing **(C)** TDP-43 granules and **(D)** P-bodies (DCP1A). Points - single image tiles. ~60-160 image tiles per human subject/organelle. ($\hat{\theta}$) the effect size estimate. **(E)** Experimental design for an expanded marker study of 32 organelles in day 60 motor neurons. Three plates, each containing one human subject from every group. Three experimental repeats (human subjects) for each group in the meta-analysis. **(F)** Cytoplasmic-to-nuclear TDP-43 signal ratios in C9ALS, sALS- or sALS+ vs. healthy controls (means: 1.032, 0.772 or 1.038 vs. 0.717, respectively, **** $p < 0.0001$, linear mixed-effects model). Joint UMAP projections of **(G)** TDP-43 granules and **(H)** P-bodies (DCP1A). Individual human subject IDs denoted. Subjects 8, 9, 10 and 16 shared between initial and expanded marker cohorts. 30-90 image tiles per human subject/organelle. ($\hat{\mu}$) the combined effect size estimate. **(I)** Stacked forest plot of organelle effect size (log2 fold change) in day 60 human subject motor neurons from three C9ALS patients relative to three healthy controls. Colored dots represent the effect estimate per experimental repeat (human subject), with horizontal bars indicating the 95% CI of within-study variance. Paired C9ALS and healthy control within plate and meta-analysis of three plates. The combined effect estimate ($\hat{\mu}$) is shown in black diamond with its 95% meta-analytic CI, which accounts for between experimental repeat (human subject) variance. Adjusted p-value: * < 0.05, ** < 0.01, **** < 0.0001. ~50-170 image tiles per organelle/human subject. **(J)** Boxplots of P-body-positive (DCP1A) pixels that are also positive for endogenous TDP-43. Colocalization fraction in human subjects day 60 motor neuron images in C9ALS, sALS- or sALS+ vs. healthy controls (mean fraction overlap = 0.433, 0.13 or 0.433 vs. 0.128, respectively). ~70-170 image tiles per human subject; Linear fixed-effects model with human subject-clustered standard errors (fallback used). **** $p < 0.0001$. Three human subjects per group. **(K)** CellProfiler quantification of P-body size (mean radius) in C9ALS, sALS- or sALS+ vs. healthy controls (means: 1.17, 1.20 or 1.18 vs. 1.19, respectively). Three human subjects per group. Linear fixed-effects model with human subject-clustered standard errors (fallback used). **** $p < 0.0001$. In all box plots, the black line indicates group mean. Large, saturated dots - human subject means; small, washed dots - individual site images. Percentage of DAB chromogenic immunohistochemistry signal for P-body proteins, **(L)** LSM14A or **(M)** DCP1A, colocalized with TDP-43 aptamer[139]. Each point represents the average colocalized area (%) across three regions of interest (n=3 ROIs) in post-mortem frontal lobe punches from four C9ALS patients (1-4). Mean ± SD, quantified using ImageJ. Quantification of **(N)** intra-cellular (means: 0.07, 3.33, 2.61) and **(O)** extracellular (means: 0.70, 10.83, 6.17) LSM14A-positive(+) bodies in brain sections and **(P)** their representative images (arrowheads), from controls (blue, n=10), C9ALS (red; n=6) or sporadic ALS (dark brown, n=6). Data points - mean number of cells containing intracellular bodies or number of extracellular bodies per mm^2; Mean ± SD; Kruskal-Wallis test with Dunn's multiple comparisons; Adjusted p-value: * < 0.05, ** < 0.01, *** < 0.001. **(Q)** Percentage of down-regulated mRNAs in isolated neuronal nuclei without TDP-43 relative to uninvolved normal neuronal nuclei analyzed in five *C9orf72*

641 post-mortem human nervous systems [140]. Bins of P-body-enriched/depleted mRNAs (by FDR ≤ 0.05
642 and enrichment ≥ 1 or ≤ −1, respectively in Ref. [116]). Odds-ratio and one-sided Fisher's exact test and
643 Benjamini–Hochberg FDR; * $p < 0.05$. n.s. non-significant. Lower left: Cochran-Mantel-Haenszel (CMH)
644 test for overall association based on per-subject contingency 2×2 tables and controlling for subject as
645 a stratum. χ^2 statistic, **** p (one-sided) < 0.0001, and 95% CI [1.38, 2.56]. **(R)** Model for mechanism
646 and consequences of cytoplasmic TDP-43 interactions with P-bodies in ALS.

Discussion

In this work, we present NOVA, a deep learning framework for microscopic phenotyping studies in neurons. We developed a ViT architecture with supervised contrastive loss to systematically encode perturbation-induced subcellular localization and morphology patterns from immunofluorescent images of membrane-bound and membraneless organelles (**Figure 1**). NOVA enables characterization of organellar responses to perturbations on a single metric scale, including responses to stress (**Figure 2**) and ALS-associated genetic variants (**Figure 3**). Our study further revealed that cytoplasmic TDP-43, a key hallmark of ALS, alters P-body biophysics and function (**Figure 4**). Deep microscopic phenotyping with NOVA can also be applied to human–derived motor neurons (**Figure 5**), overcoming inter-patient heterogeneity and sex differences[141]. The organellar changes described in experimental ALS-like models and ALS patient neurons demonstrate both unique and shared alterations across different ALS genetic backgrounds, highlighting the broader potential of organellomics to advance insight into neuro-cellular biology and prioritise functionally relevant effects.

Organellomics is a new high-throughput omics approach for comparison of any number of organelles across diverse subcellular topographies. The relevance of organellomic studies lies in the need to understand the complex regulation of cellular functions through the network of membrane-bound and membraneless organelles[87,142–149]. Our image-based organellomics strategy provides a compelling alternative to traditional biochemical methods of organellar fractionation[3–7], addressing the inherent challenges of isolating organelles, particularly liquid-like membraneless structures[150]. The use of thoroughly characterized commercial antibodies for immunofluorescence in the method we have developed, combined with standard confocal microscopy, offers a flexible platform that is easily transferable and scalable, making it readily adoptable by most laboratories without specialized infrastructure. Thus, our approach delivers unprecedented depth to organellar studies while enabling investigations at scale.

NOVA's ability to study perturbed cultured human neurons offers several advantages. First, the model was pre-trained on OpenCell data from 1,311 proteins, learning to encode localization patterns from a publicly available dataset. This pre-training step optimized the model for predicting organelle identity from image embeddings and enhanced its generalizability to unseen organelles. Next, we extended the model to a perturbation learning task through contrastive loss and partial fine-tuning. During fine-tuning on a dataset composed of ~3.2 million images of perturbed cultured human neurons generated in-house, we selectively froze specific layers using the angle metric approach, and replaced the loss function with a contrastive objective that encourages the model to learn features that are robust and discriminative for perturbation effects.

Furthermore, we developed an organelle scoring framework that ranks perturbation responses and enables direct comparisons across all studied organelles, while accounting for inter-experimental repeat differences. To ensure robust and reproducible statistical inference, experimental repeats were explicitly modeled using mixed-effects modeling. To test whether organelles are consistently affected, this approach incorporates random effects to capture variability alongside fixed effects representing the biological conditions or perturbations of interest. As suggested in [151], this strategy separates true treatment effects from experimental repeat-specific noise, thereby improving reproducibility and interpretability. In our framework, NOVA-derived embeddings are used to estimate organelle-level effect sizes ($\hat{\theta}$) that capture the extent to which a perturbation shifts organelle topography from

689 baseline. Effect sizes are calculated per perturbation-organelle-experimental repeat combination,
690 relative to the natural variability observed in control embeddings. Experimental repeat-specific effect
691 sizes ($\hat{\theta}$) are then combined through meta-analytic modeling to yield a combined effect size ($\hat{\mu}$), which
692 accounts for heterogeneity across experimental repeats (cell line differentiation, or human subject).
693 Organelles are ranked by their combined effect size, and multiple hypothesis correction is applied. By
694 operating exclusively on distances in latent space, this framework provides a unified metric for
695 quantifying organellar changes in response to perturbations. Thus, mixed-effects meta-analysis of
696 NOVA-derived embeddings determines both effect size and reproducibility with rigorous statistical
697 support.

698 NOVA's generalizability is demonstrated by its ability to analyze data from multiple cell lines, including
699 those not seen during training (e.g., TDP-43$^{\Delta NLS}$ and patient-derived motor neurons), across different
700 neuronal types (day 8 cortical neurons and day 60 human subject–derived motor neurons), and using
701 data generated by different microscopes and experimentalists across laboratories. In addition, we
702 successfully performed inference on several neuronal markers not included in the training set. NOVA
703 also performed well in a clinically relevant out-of-distribution task: identifying neuronal disease
704 phenotypes (human subject–derived C9 and sporadic ALS neurons versus healthy controls), where
705 disease-related changes outweighed individual variability. Together, these results support NOVA as a
706 solid foundation for future AI-driven studies in neurobiology.

707 Moreover, NOVA offers practical advantages: (i) our in-house dataset, comprising millions of neuronal
708 images captured under diverse perturbations, is now released and publicly available, providing a
709 valuable resource for future research. (ii) the technology operates on standard confocal images,
710 offering a cost-effective alternative to complex multiplexed platforms such as PhenoCycler or 4i[152,153];
711 (iii) it can be applied retrospectively to existing microscopy datasets and is agnostic to the number of
712 fluorescent channels; and (iv) compared with methods based on hand-engineered features (e.g.,
713 CellPainting and CellProfiler[46,47]), NOVA's deep representation learning captures multi-scale patterns
714 without pre-defined objects, which was shown to generalize better across markers and conditions[154–
715 157]. Noteworthy, Cell Painting captures standardized morphology using six dyes and offers
716 interpretable baselines, whereas NOVA learns organelle organization directly from endogenous
717 protein patterns, flexibly adapts to any fluorescent marker, and quantifies perturbation effects across
718 numerous organelles.

719 NOVA enabled mapping of the neuronal stress response at the level of the entire organellome for the
720 first time. This revealed that oxidative stress induces not only the expected formation of stress
721 granules (SGs), but also topographic remodeling of diverse additional organelles. While changes in
722 individual organelles have been reported[158,159], we are able to demonstrate the relative topographic
723 changes to all organelles, including nuclear PML bodies and mitochondria. In this way, NOVA highlights
724 how stress triggers a distributed reorganization across multiple organelles. Recently, Rhoads et al.,
725 suggested organelle-level differences between neurons and astrocytes in rodent CNS cells in response
726 to stress [160], suggesting another layer of cell-type specificity.

727 Application of NOVA to the iPSC Neurodegenerative Disease Initiative (iNDI) provided the first
728 organellomic maps of ALS-affected human cortical neurons. This revealed unanticipated changes in
729 FUS granules, P-bodies, and lysosomes in several ALS-associated variants. *TARDBP* M337V drove only
730 modest alterations, consistent with literature reporting minimal mislocalization of TDP-43 in

731 premature iPSC-derived neurons[161,162], possibly reflecting the early developmental stage of the
732 neurons. The *FUS* R495* variant, clinically associated with aggressive juvenile ALS and deficient in its
733 nuclear localization signal[99,163–165], was analyzed alongside an isogenic revertant in which the arginine
734 at position 495 was restored. NOVA detected robust changes in FUS granules and additional
735 compartments, including the hnRNP complex, peroxisomes, lysosomes, and PURA granules.
736 Comparison with both wild-type and revertant controls indicated that many alterations reflected
737 genuine FUS-driven organellar changes, noticeable even in the context of passage effects or CRISPR
738 off-target edits. Together, these data confirm that FUS mislocalization exerts widespread,
739 reproducible effects on organelle organization.

740 A prominent NOVA finding was the reproducible sensitivity of P-bodies to cytoplasmic TDP-43, in line
741 with previous work in rat hippocampal neurons[128]. Inducible TDP-43$^{\Delta NLS}$ neurons displayed significant
742 remodeling of P-bodies (marked by LSM14A/DCP1A) without concomitant SG changes, demonstrating
743 that TDP-43–P-body crosstalk can be SG-independent. This is intriguing given the reported
744 interactions between P-bodies and SGs and TDP-43 influence on P-body-SG docking, [145,166] but
745 resonates with other reports about independence of cytoplasmic TDP-43 and stress granules [126].
746 Orthogonal assays reinforced this conclusion: microscopy showed colocalization between P-bodies
747 and TDP-43 inclusions; proximity labeling/MS identified P-body proteins enriched in the vicinity of
748 cytoplasmic TDP-43; and quantitative morphology analyses revealed smaller, less fluid P-bodies,
749 consistent with FRAP-based evidence of altered P-body biophysics. These effects extended to
750 patient-derived neurons and C9ALS post-mortem cortex, where cytoplasmic TDP-43 aggregates
751 co-localized with P-body markers and correlated with altered P-body morphology. Furthermore, large
752 intracellular and extracellular LSM14A-positive inclusions were specific to human C9ALS and sporadic
753 ALS neuropathology and absent in non-neurological controls, suggesting new potential biomarkers.

754 Cytoplasmic TDP-43 also increased the decay of mRNAs enriched in P-bodies, which are similarly
755 downregulated in nuclei from *C9orf72* TDP-43 proteinopathy patients. Together, and supported by
756 recent preprints that suggest new roles for P-bodies in ALS [167,168], these observations highlight P-bodies
757 as a convergent hub in TDP-43 proteinopathies and as a potential therapeutic target. These findings
758 implicate P-bodies in the pathobiology of C9ALS and motivate targeted studies of their dynamics,
759 RNA-handling roles, and interactions with TDP-43.

760 We acknowledge notable limitations in the model. In order to be applicable to any cell type, NOVA's
761 design intentionally avoids whole-cell contour segmentation and the training images predominantly
762 contain single cells. This confers substantial computational efficiency but confines use to
763 homogeneous cultures. Analyses in more complex settings, such as co-cultures, mixed genotypes, and
764 tissue sections, will require additional development. At present, the NOVA model has been validated
765 on iPSC-derived cortical and motor neurons. We anticipate that it can be extended to additional
766 disease-relevant cell types, including microglia and astrocytes. Similarly, the present focus on static
767 topography could be broadened by quantifying organelle contact sites and microscopy-compatible
768 functional reporters could provide complementary readouts of organelle activity. Quality control of
769 such large and complex screening datasets, model training on new data, and statistical inference all
770 require a degree of machine learning proficiency. Finally, translating quantified topographic shifts into
771 mechanisms will benefit from targeted perturbations and dedicated interpretability methods, which
772 together can provide clearer causal insight into the underlying biology.

773 Altogether, organellomics is a microscopy-based framework for interrogating organellar cell biology
774 at scale. It builds on standard immunofluorescence workflows and functions robustly across diverse
775 imaging platforms. It provides representation of the full organellar landscape, enabling quantitative
776 comparisons of cellular responses to any type of perturbation. In doing so, organellomics move
777 beyond compartment-specific narratives toward system-level deep phenotyping of cellular
778 organization and its disruption in disease. The NOVA framework is broadly extensible to additional
779 disease phenotypes, other types of patient-derived cells, and existing imaging data. Organellomics
780 holds the potential to generate novel hypotheses in cellular and disease biology research and may
781 foster diagnosis and precision medicine for neurological diseases.

782 **Supplementary Figures**

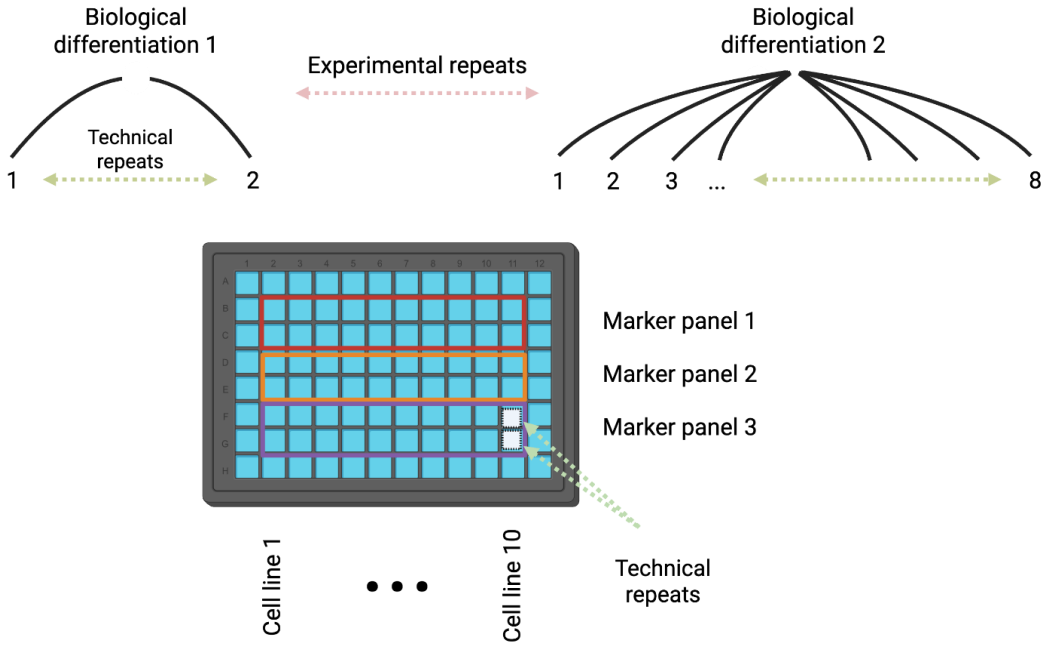

783

784 **Supplementary Figure 1. Experimental design of iPSC-derived cortical neurons used for model**
785 **training.** Each 96-well plate included 10 cell lines or conditions and 3 marker panels, with a total of 60
786 wells used per plate. A full experimental repeat for studying 25 organelles was generated using 11
787 marker panels across 4 different plates (see **Table 1**). Each well contained a distinct cell line or
788 experimental condition, with a specific marker panel consisting of antibodies targeting 2–4 organelles.
789 From each well, 100 site images were acquired. For each full organellomic study, two wells (technical
790 repeats) per marker panel per plate were imaged. Bottom: an exemplary plate design from a single
791 experimental repeat (biological differentiation).

792

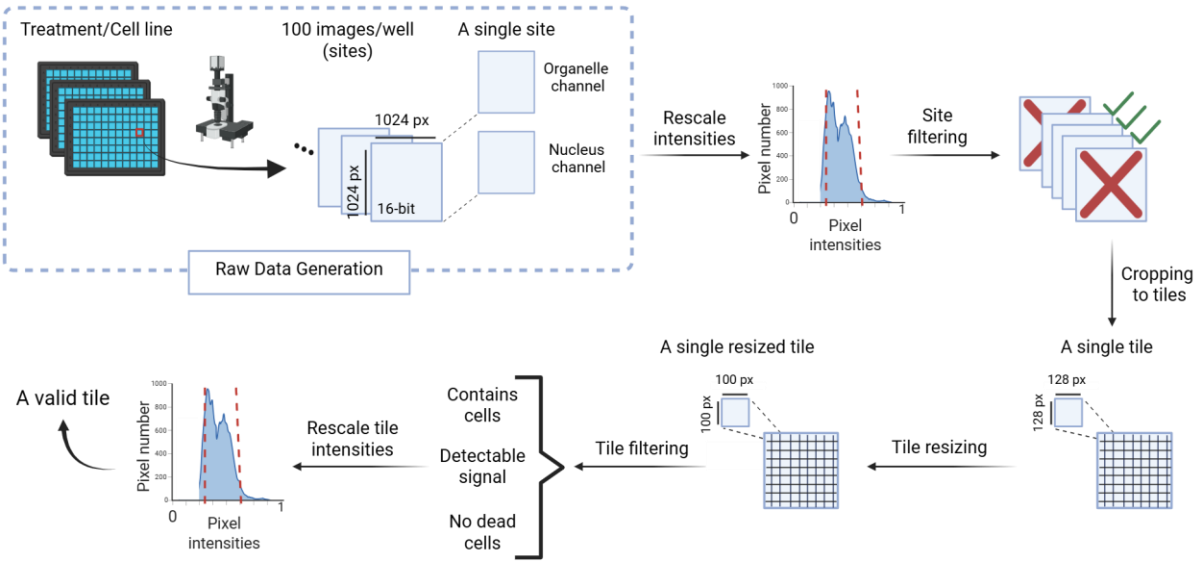

Supplementary Figure 2. Image quality control (QC) and pre-processing.

Microscopy images were acquired at defined fluorescent emission frequencies, stained for a single organelle, and collected at 16-bit resolution, 1024 × 1024 pixels (referred to as "site images"). All organelle images were paired with the corresponding nucleus channel. Site images were rescaled to [0,1] and tested for autofocus quality using the Brenner score (**Methods**). Site images that passed QC were cropped into 64 tiles of 128 × 128 pixels. Tiles then resized to 100 × 100 pixels. Automated nuclei detection was performed on the nucleus channel using CellPose, retaining tiles with at least one but no more than five nuclei. The resulting tiles were rescaled again to [0,1]. To reduce false positives, tiles lacking detectable signal in either channel or flagged as containing dead cells were excluded (**Methods**). The remaining tiles were retained for analysis.

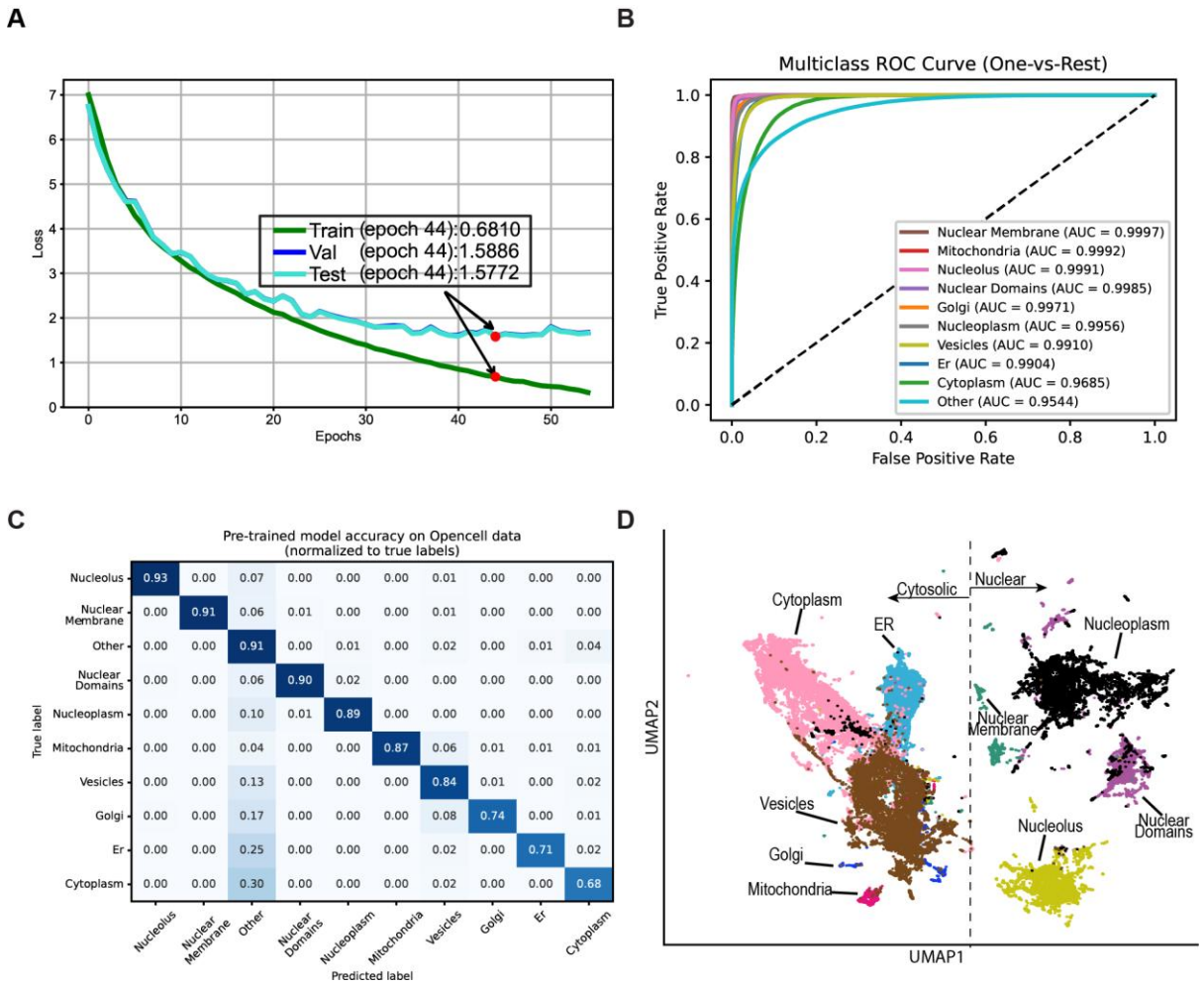

Supplementary Figure 3. ViT-based protein classification model trained to encode organelle subcellular localization patterns of 1,311 proteins in human embryonic kidney cells. (A) Training curves of the model on the OpenCell dataset (train, validation, and test). The y-axis shows the loss value, and the x-axis the number of epochs. Epoch 44, marked by a red dot, was selected as the final model, as it was the last epoch with an improvement in validation loss. Exact loss values are shown in the inset. **(B)** Receiver operating characteristic (ROC) curves for each organelle class in a one-vs-rest setting. The x-axis represents the false positive rate, and the y-axis the true positive rate. Each colored curve corresponds to one organelle class, with its area under the curve (AUC) shown in the legend. AUC values near 1 indicate excellent discriminative performance. The dashed diagonal line represents random classification (AUC = 0.5). The class "Other" represents markers not associated with annotated organelles in the dataset. **(C)** Confusion matrix showing the accuracy of the pre-trained model in predicting organelle identity. The x-axis represents predicted labels, and the y-axis true labels. Values are normalized per true label to [0,1]. High diagonal values indicate correct predictions, while off-diagonal values reflect misclassifications. The model achieved strong performance across most organelles. **(D)** UMAP visualization of the OpenCell test set (held-out data), colored by protein localization categories, shows distinct organelle clustering. Only proteins with clear and exclusive localization patterns are depicted (~7k image tiles per localization category). The list of annotated proteins is provided in the **Supplementary Materials** (OpenCell_annotated_proteins.csv).

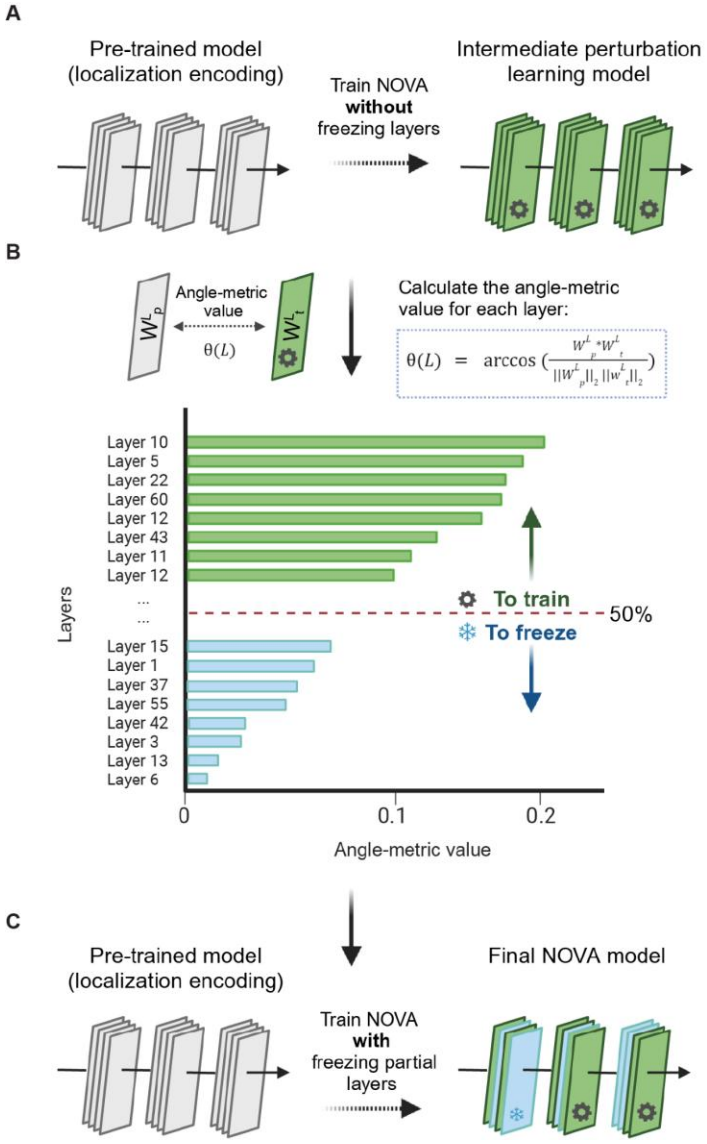

Supplementary Figure 4. Partial fine-tuning using the angle-metric approach.

Starting from the pre-trained model for localization encoding on the OpenCell dataset, a data-driven strategy was applied to identify which layers to freeze during fine-tuning for perturbation learning. Freezing a layer prevents it from updating during fine-tuning. **(A)** Initial fine-tuning with a contrastive loss function was performed on neuronal perturbation data without freezing any layers. **(B)** The angle metric, which is a vector similarity measure, was calculated between corresponding layers of the pre-trained and fine-tuned models. Layers with angle metric values below the median were frozen. **(C)** A final fine-tuning step, beginning from the same pre-trained model with the selected layers frozen, produced the NOVA model used throughout this work.

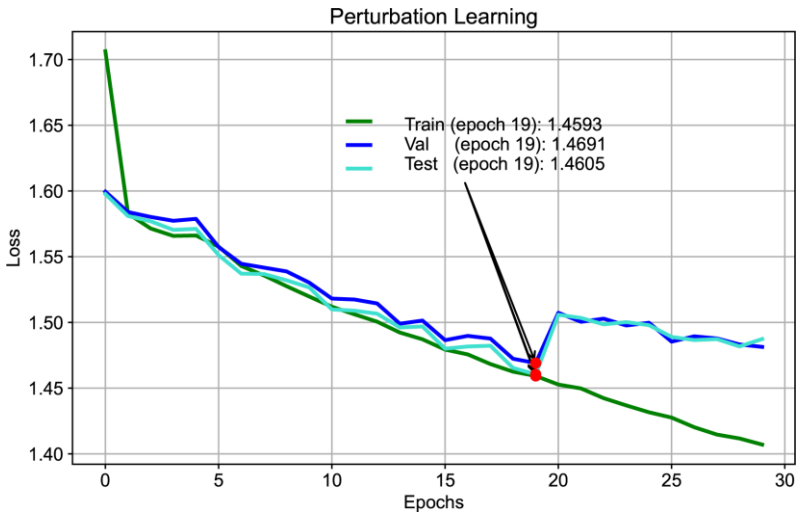

Supplementary Figure 5. Loss curves for the perturbation learning ViT fine-tuned model. The training curves of the fine-tuned model for perturbations learning on iPSCs-derived neurons (train, val (validation), and test. Loss value of the model (y-axis) and the number of epochs (x-axis). Epoch 19, marked by a red dot, was selected as the final model, as it was the last epoch with an improvement in validation loss. Exact loss values depicted.

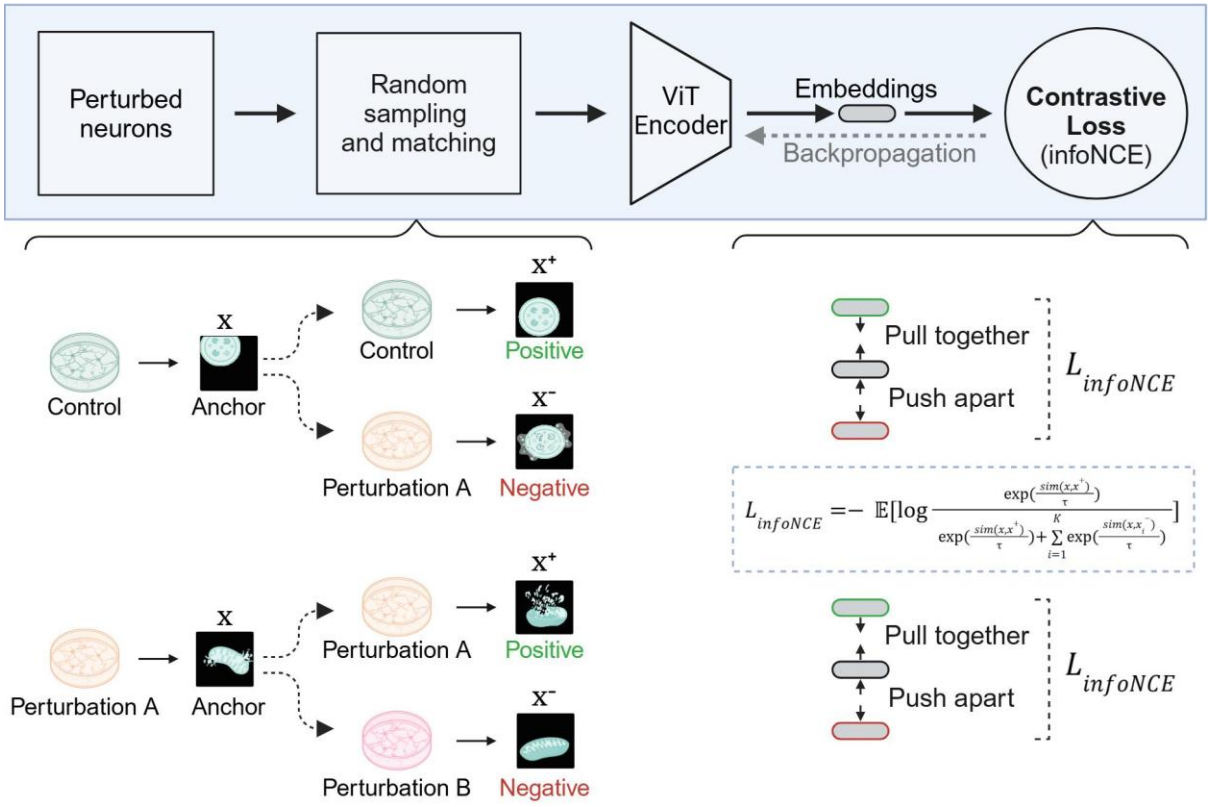

Supplementary Figure 6. Perturbation learning workflow with contrastive learning.

For each image in the training set (the "anchor"), six additional tiles were randomly sampled from different wells and experimental repeats: one positive and five negatives. Positives were tiles from the same organelle and perturbation as the anchor, while negatives were tiles from the same organelle under different perturbations. Embeddings for all seven samples were computed, and the InfoNCE contrastive loss was applied. Contrastive learning pulled together images with similar topographies (anchor and positives) and pushed apart dissimilar ones (negatives), enabling the model to learn a structured latent space. Random sampling across experimental repeats was performed to reduce overfitting to non-biological differences such as biological differentiation or plate effects. See **Methods** for details.

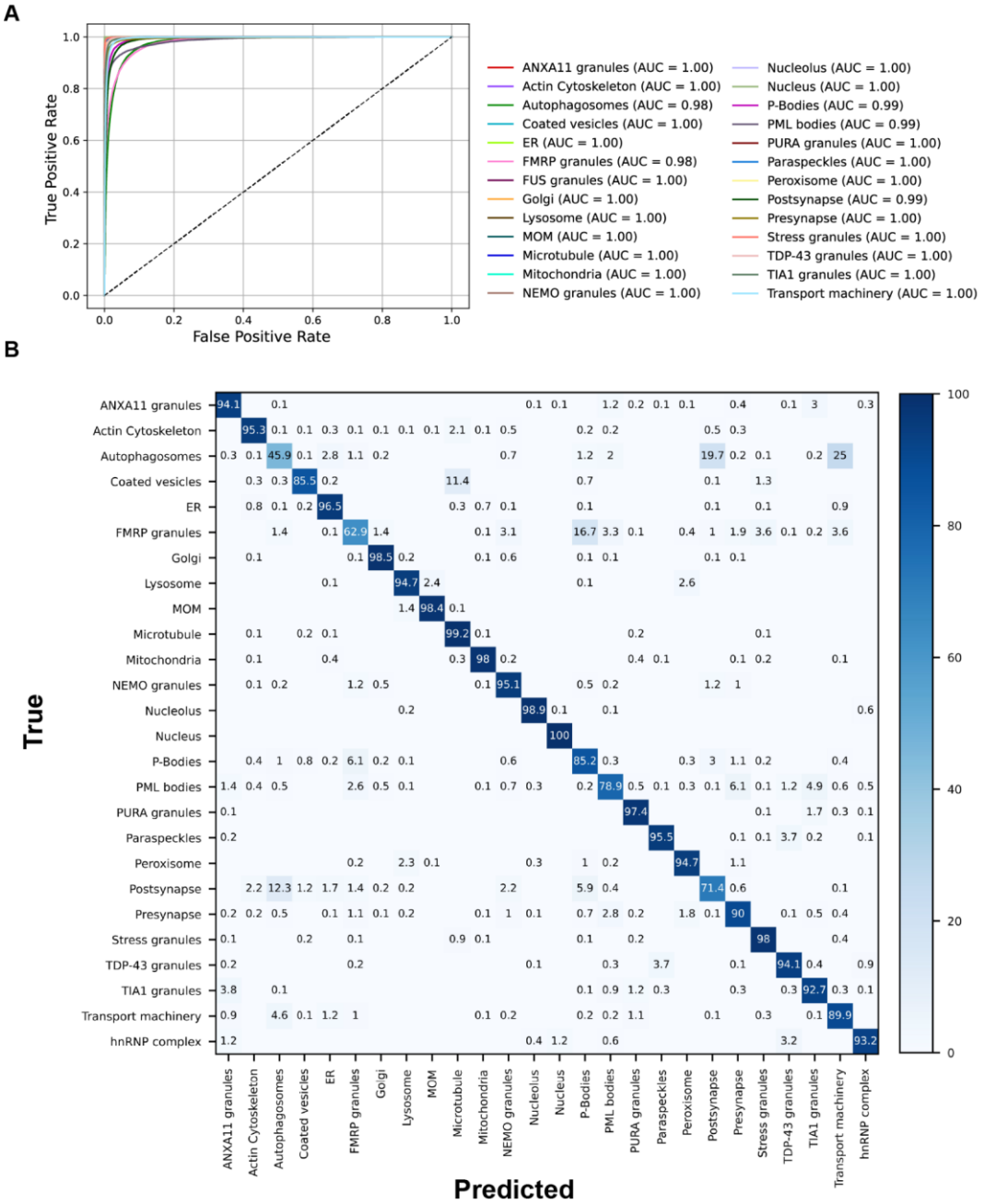

Supplementary Figure 7. Organelle identification performance of NOVA embeddings.

NOVA's embeddings showed strong organelle identification performance on the dataset in **Figure 1C**. A classifier was trained on these embeddings (see **Methods**) and evaluated using two complementary approaches. **(A)** Receiver operating characteristic (ROC) curves for all organelles. Each curve shows the change in true positive rate relative to false positive rate as the classification threshold varied. The area under the curve (AUC) is reported, with values > 0.97 for all organelles, indicating excellent discriminative performance. **(B)** Confusion matrix of classification accuracy across organelles. Values represent the percentage of true labels assigned to each predicted label. High diagonal values indicate strong prediction accuracy, while low off-diagonal values reflect minimal misclassification.

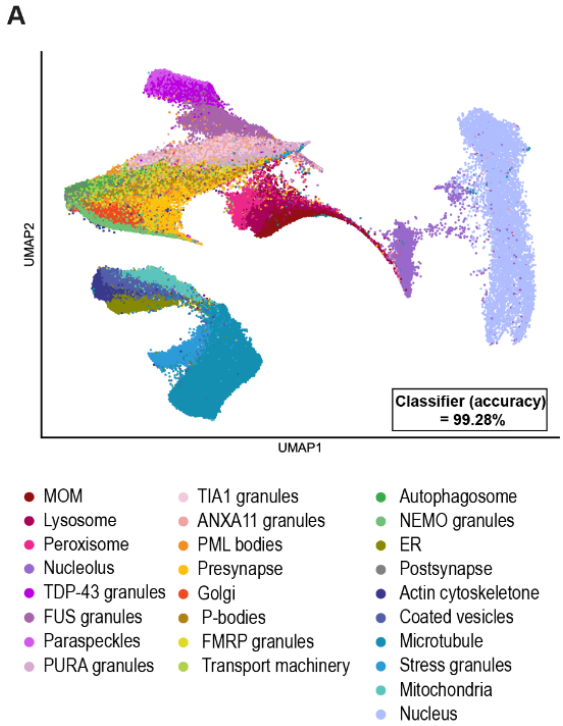

C

	Accuracy (%)	Sensitivity (%)	Specificity (%)
NOVA	**99.57**	**90.26**	**99.77**
Cytoself	99.28	83.66	99.63
CellProfiler	98.62	79.88	99.28

Supplementary Figure 8. Benchmarking NOVA in neuronal organelle identification against published methods.

The organelle landscape in the dataset shown in **Figure 1C** displayed better-defined clusters compared to **(A)** Cytoself-derived features (classifier accuracy = 99.28%; ~6k image tiles per organelle) or **(B)** CellProfiler-derived features (classifier accuracy = 98.62%; ~560 image sites per organelle to match CellProfiler's typical site-level analysis). **(C)** Performance comparison of classifiers trained on NOVA-derived embeddings, Cytoself-derived embeddings, and CellProfiler features for organelle identification. While Cytoself and CellProfiler achieved equivalent overall accuracy, NOVA's embeddings captured the information needed for this task with higher sensitivity (83.66% vs. 79.88% vs. 90.26%).

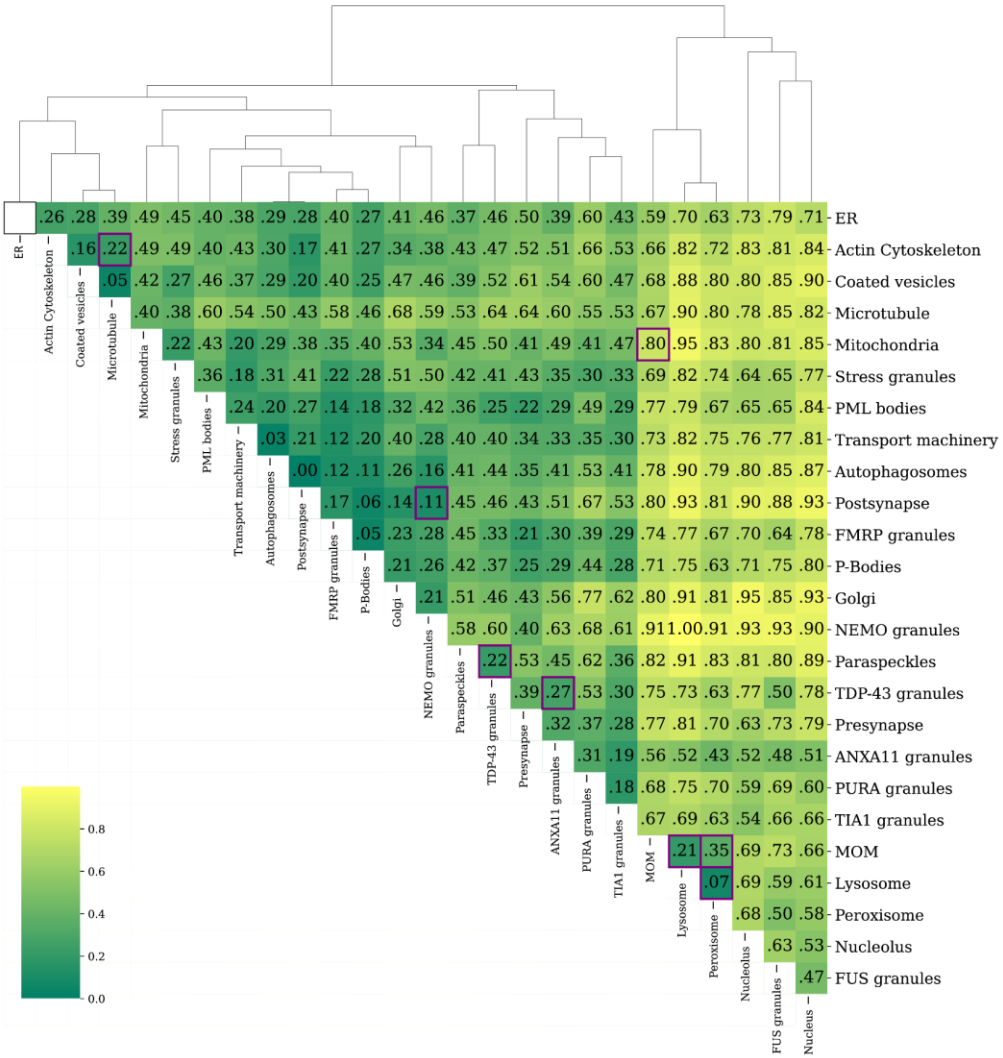

Supplementary Figure 9. Distances across the organellar landscape of day 8 human iPSC-derived neurons.

For each organelle pair in the landscape shown in **Figure 1C**, pairwise Euclidean distances were computed between NOVA-derived embeddings. Heatmap values represent the median distance, rescaled to the [0,1] interval using min–max normalization. A value of 0 indicates the closest organelles (highest similarity, darker colors), and 1 the most distant (lowest similarity, lighter colors). Rows and columns were clustered by agglomerative hierarchical clustering of the scaled distance values (Euclidean distance, average linkage). Dendrogram depicts the hierarchical relationships among organelles.

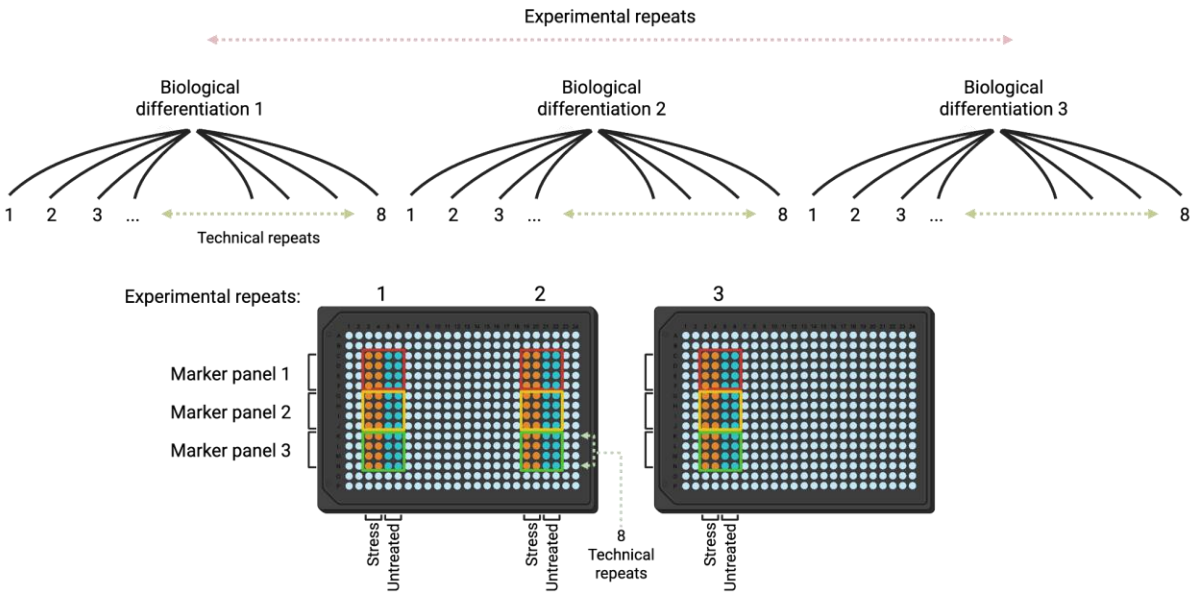

896

897 **Supplementary Figure 10. Experimental design of the NIH CARD dataset, related to Figures 1 and 2.**
898 Three experimental repeats (biological differentiations), with eight technical repeats (wells) each.
899 Twenty-five site images were acquired per well. Two columns for oxidative stress treatment and two
900 untreated. Every four rows were assigned to a different marker panel. 12 marker panels in total with
901 three marker panels per plate. Cells were seeded into PLO-coated 384-well plates on day 4 post-
902 differentiation and fixed on day 8 of differentiation.

903

904

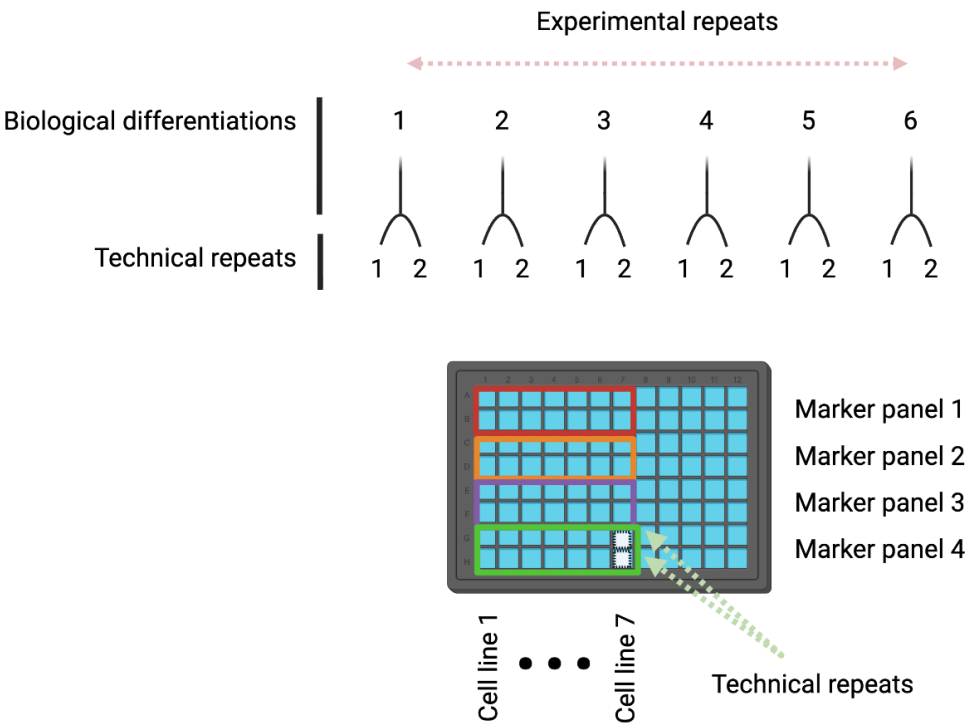

905

906 **Supplementary Figure 11. Experimental design of iNDI lines used for inference related to Figure 3.**
907 Six experimental repeats (biological differentiations), with two technical repeats (wells) each. Seven
908 iNDI lines: ancestral isogenic control line, Knockout Laboratory F2.1 Jackson (wild-type, KOLF), *FUS*
909 R495* homozygous, *FUS* R495* heterozygous, *FUS* revertant (corrected *495R), *TARDBP* M337V
910 homozygous, *OPTN* Q398E homozygous, *TBK1* E696K homozygous. Each line seeded into a separate
911 column. Every two rows were assigned to a different marker panel. 12 marker panels in total with four
912 marker panels per plate. iNDI cells were seeded into PLO-coated 96-well plates on day 4 post-
913 differentiation and fixed on day 8 of differentiation. Two hundred fifty site images were acquired per
914 well. An exemplary plate design from a single experimental repeat (biological differentiation) is
915 depicted.

916

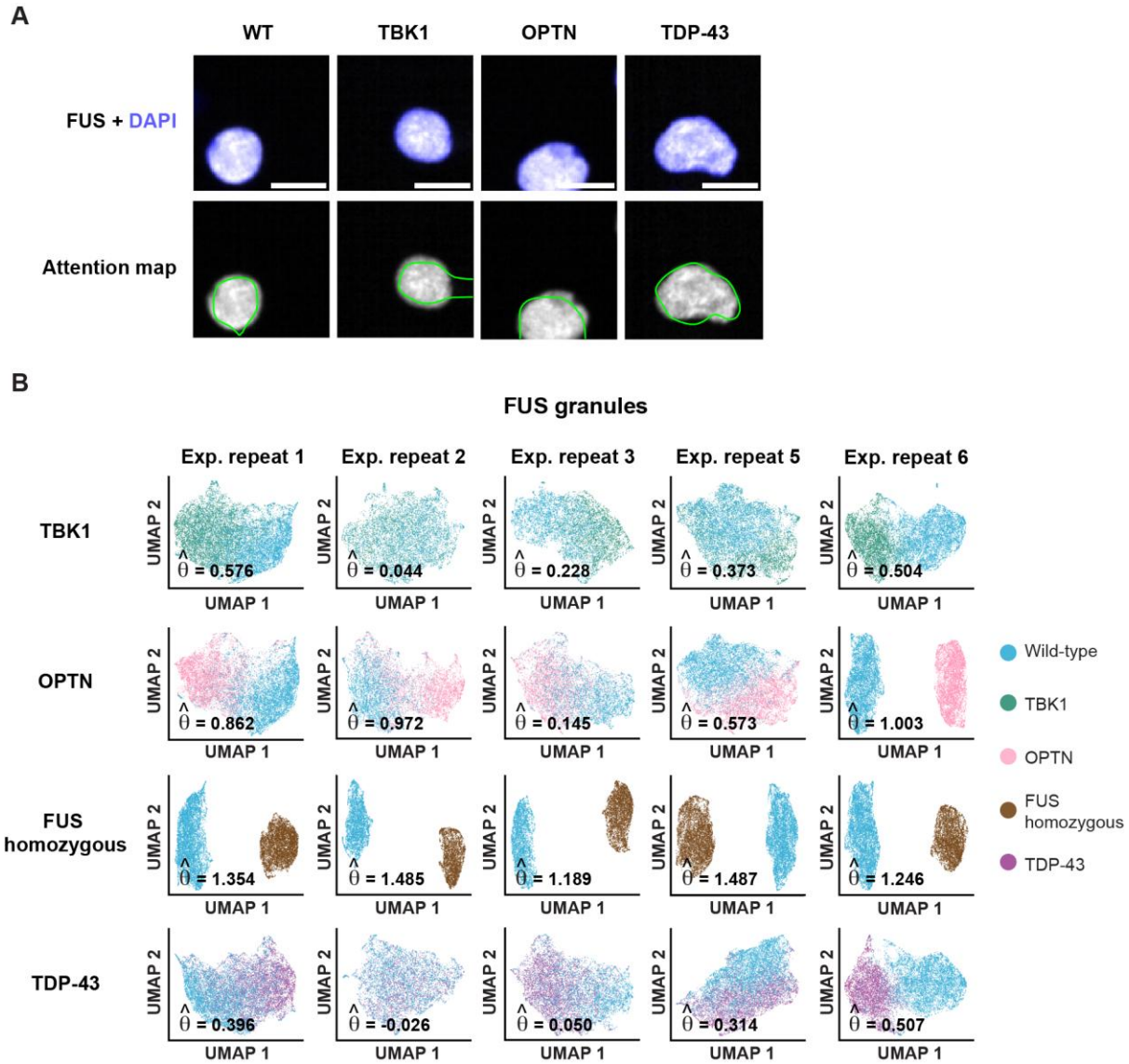

Supplementary Figure 12. Altered topography of FUS granules in the iNDI lines.

(A) Representative images of FUS granules across iNDI lines. Nucleus (hoechst 33342, blue) and overlaid model's attention maps. Scale bar - 10 µm. **(B)** UMAP visualization of FUS granule changes per experimental repeat across iNDI lines. experimental repeat # 4 is missing due to insufficient valid image tiles on FUS marker (~2.5K–7K tiles per line/experimental repeat). ($\hat{\theta}$) the effect size estimate.

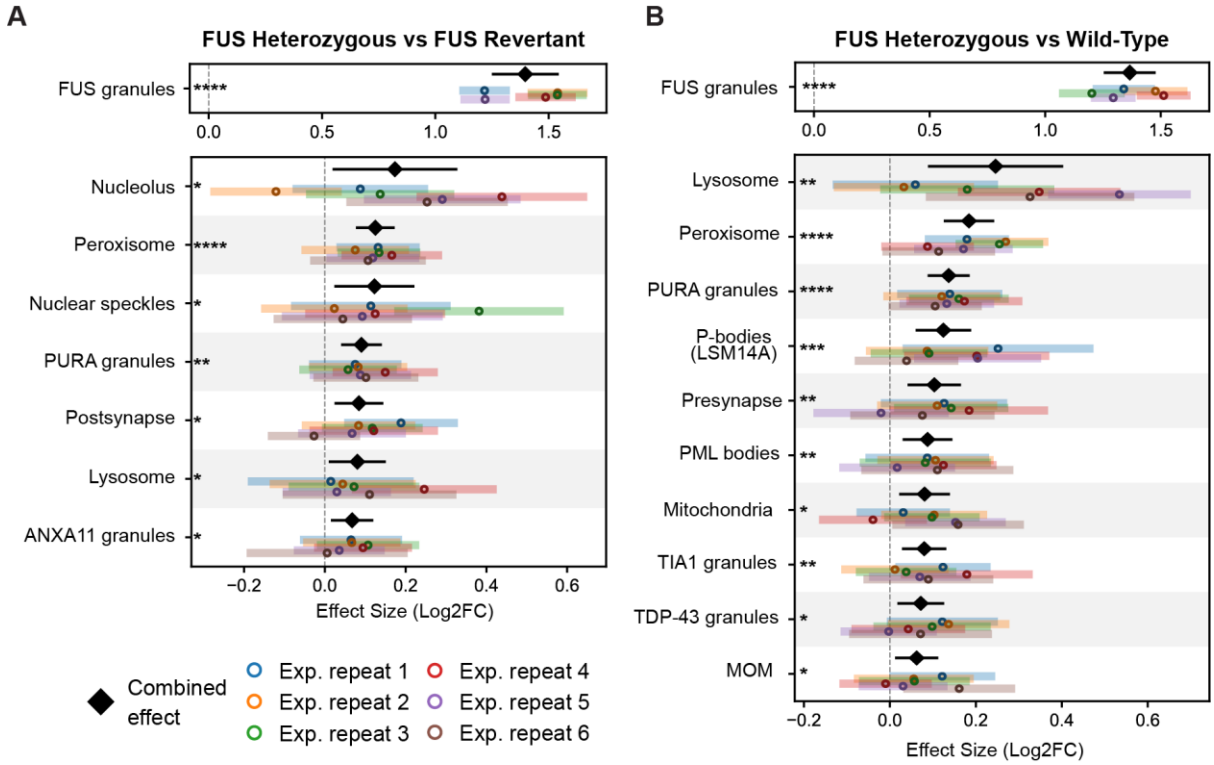

Supplementary Figure 13. Organellar scoring of iNDI FUS lines reveals unique and shared changes, including FUS granules. Stacked forest plot of organelle effect sizes ($\log_2$ fold change) in day 8 neurons carrying the heterozygous FUS R495* variant relative to **(A)** the genetically corrected FUS revertant line and **(B)** wild-type control. Six experimental repeats; 29 organelles analyzed. Only organelles significantly altered in mixed-effects meta-analysis are shown (**Methods**). Colored dots represent experimental repeat effect estimates, with horizontal bars indicating 95% CI. The combined effect estimate ($\hat{\mu}$) is shown as a black diamond with its 95% meta-analytic CI, accounting for between-experimental repeat variance. Adjusted p-values: * < 0.05, ** < 0.01, *** < 0.001, **** < 0.0001. ~780-6500 image tiles per organelle/variant/experimental repeat. FUS granules were the most altered organelle ($\hat{\mu}$ = 1.366, adj. p = 6.4×10^{-15}; I^2 = 74.99%, τ^2 = 0.0123, 95% CI = [0.0011, 0.0944]), followed by lysosomes ($\hat{\mu}$ = 0.246, adj. p = 4.9×10^{-3}; I^2 = 78.95%, τ^2 = 0.0289, 95% CI = [0.0059, 0.1756]). P-bodies marked by LSM14A, were significantly affected in the heterozygous FUS R495* variant ($\hat{\mu}$ = 0.124, adj. p = 5.6×10^{-4}) but not in the FUS R495* homozygous variant. Peroxisomes and PURA granules were significantly altered relative to both wild-type ($\hat{\mu}$ = 0.184, adj. p = 5.3×10^{-9}; $\hat{\mu}$ = 0.136, adj. p = 1.95×10^{-7}, respectively) and the genetically corrected FUS revertant line (*495R, $\hat{\mu}$ = 0.125, adj. p = 2.2×10^{-6}; $\hat{\mu}$ = 0.09, adj. p = 2×10^{-3}), alongside FUS granules ($\hat{\mu}$ = 1.397, adj. p = 6.4×10^{-15}; I^2 = 86.84%, τ^2 = 0.0243, 95% CI = [0.0055, 0.1664]).

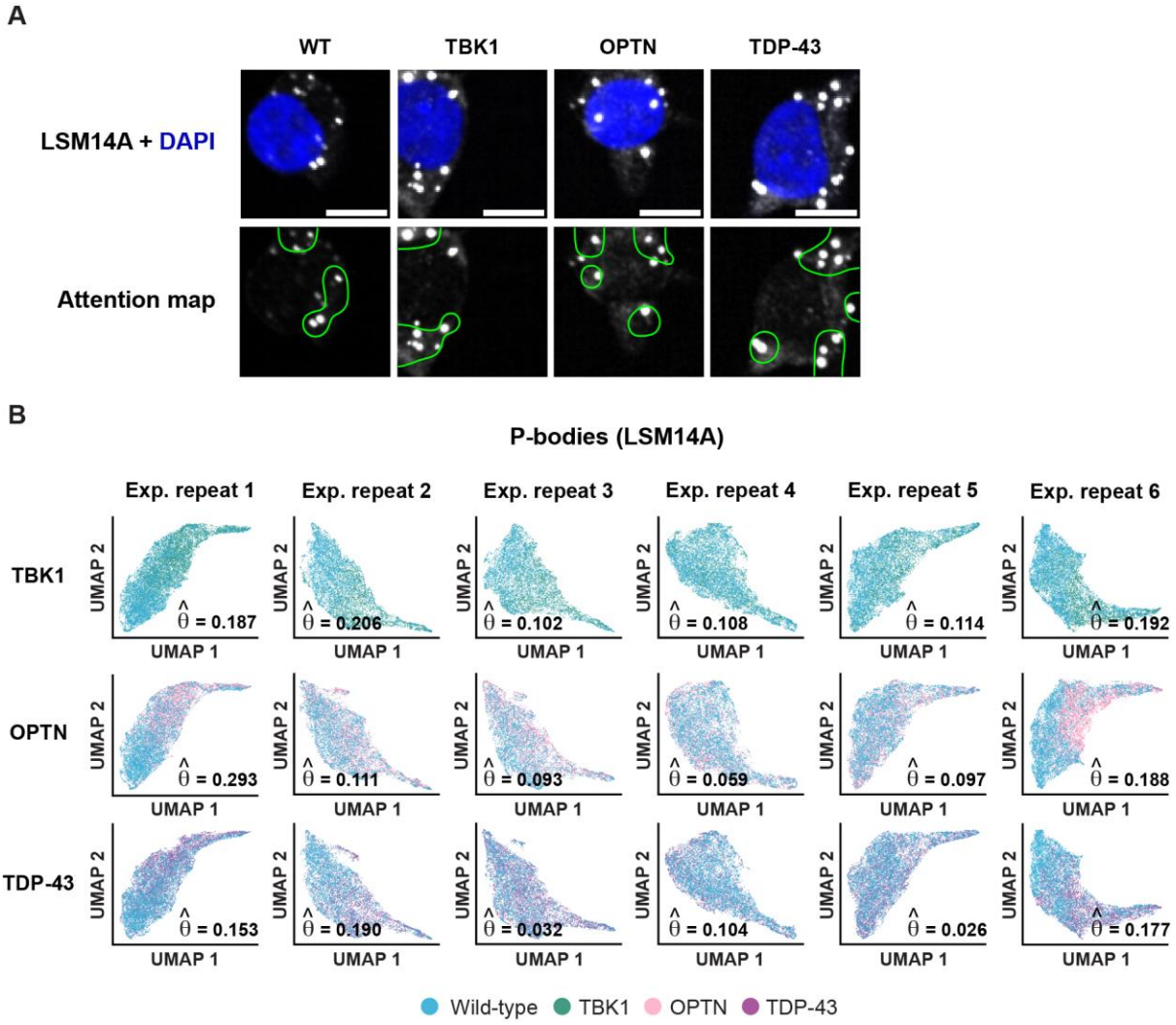

Supplementary Figure 14. Altered topography of P-bodies marked by LSM14A in the iNDI lines. (A) Representative images of P-bodies marked by LSM14A across iNDI lines. Nucleus (hoechst 33342, blue) and overlaid model's attention maps. Scale bar - 10 µm. **(B)** UMAP visualization of LSM14A changes per experimental repeat across iNDI lines. ~3300-6600 image tiles per condition/experimental repeat. ($\widehat{\boldsymbol{\theta}}$) the effect size estimate.

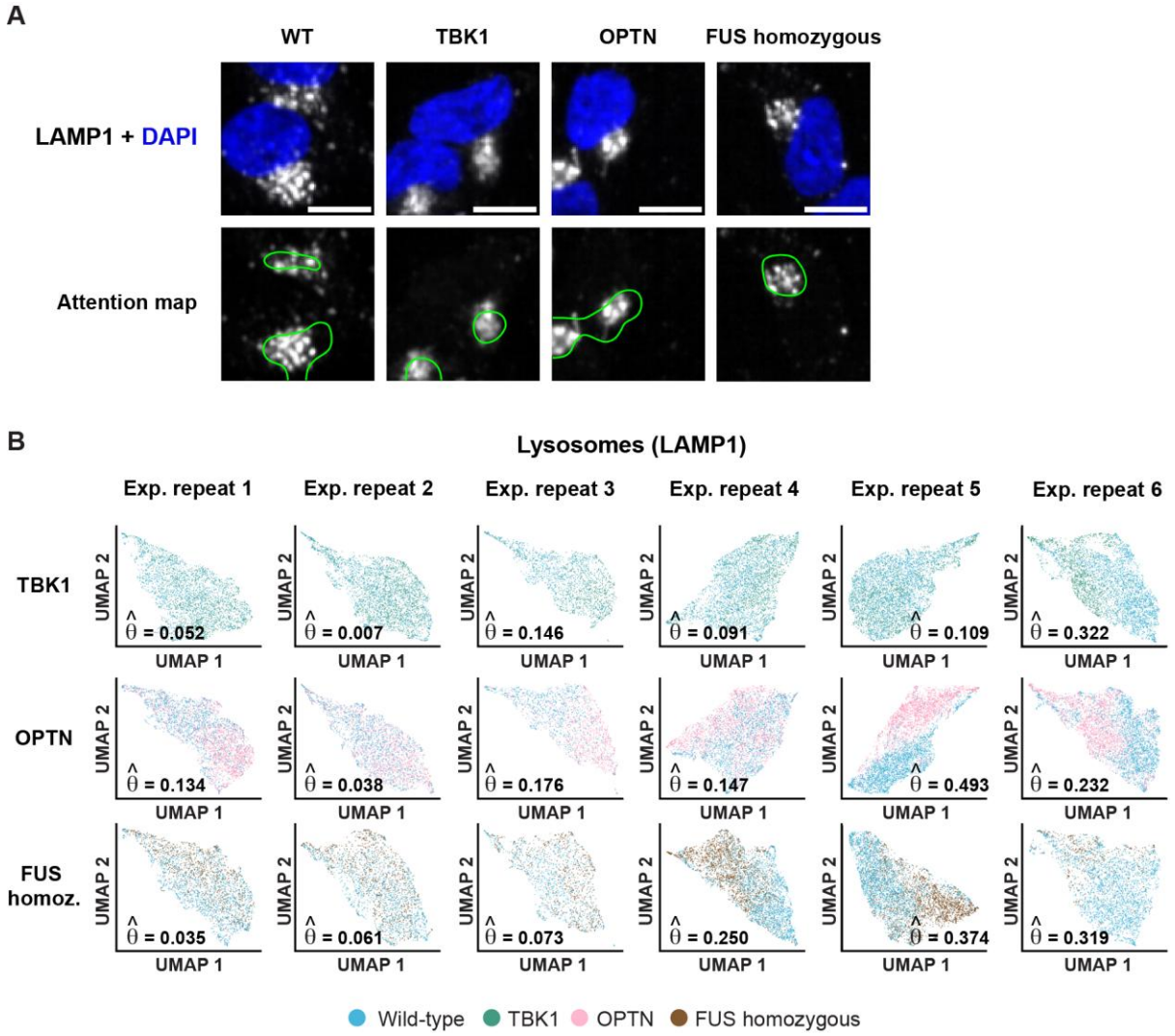

Supplementary Figure 15. Altered topography of lysosomes in the iNDI lines. (A) Representative images of lysosomes marked by LAMP1 across iNDI lines. Nucleus (hoechst 33342, blue) and overlaid model's attention maps. Scale bar - 10 µm. **(B)** UMAP visualization of LAMP1 changes per experimental repeat across iNDI lines. ~600-2700 image tiles per condition/experimental repeat. ($\widehat{\boldsymbol{\theta}}$) the effect size estimate.

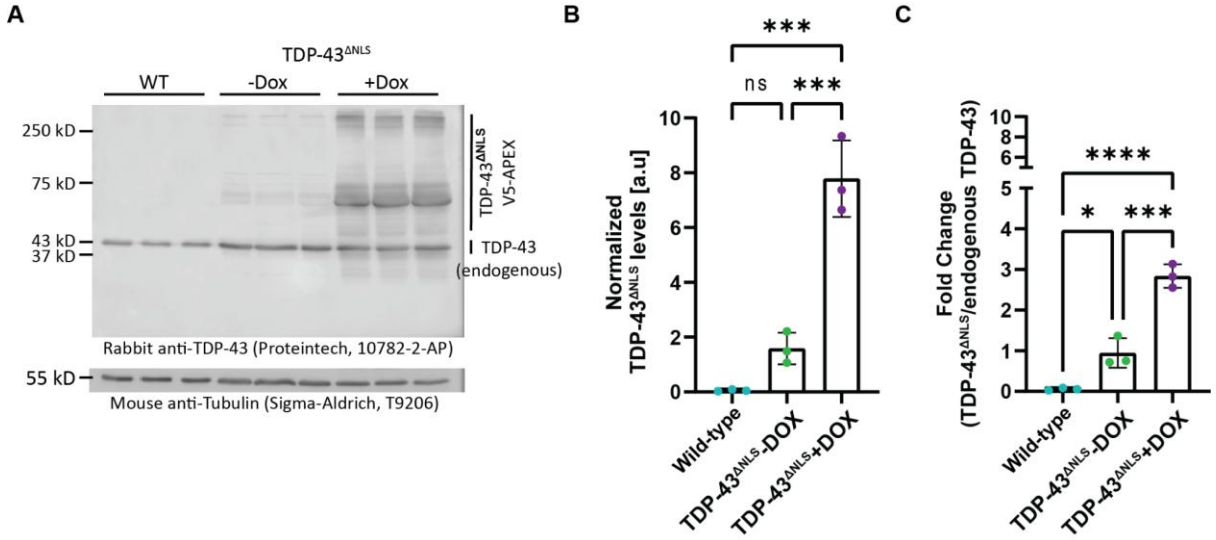

Supplementary Figure 16. Protein levels of TDP-43 in wild-type and TDP-43$^{\Delta NLS}$-expressing neurons. **(A)** Western blot analysis of endogenous TDP-43 (~43 KDa) and TDP-43$^{\Delta NLS}$-V5-APEX protein and protein oligomers (45-250 KDa bands) expression in 8-day-old wild-type (WT) neurons or neurons carrying TDP-43$^{\Delta NLS}$-V5-APEX, uninduced (-Dox) or after 24 hours of doxycycline induction (+Dox). Tubulin levels (55 KDa) were tested as loading control for normalization. **(B)** Quantification of TDP-43$^{\Delta NLS}$ levels. **(C)** Fold change of normalized TDP-43$^{\Delta NLS}$ levels relative to normalized endogenous TDP-43. P-value: * < 0.05, *** < 0.001, **** < 0.0001, ns = non-significant, One-way ANOVA with Benferroni's multiple comparison test.

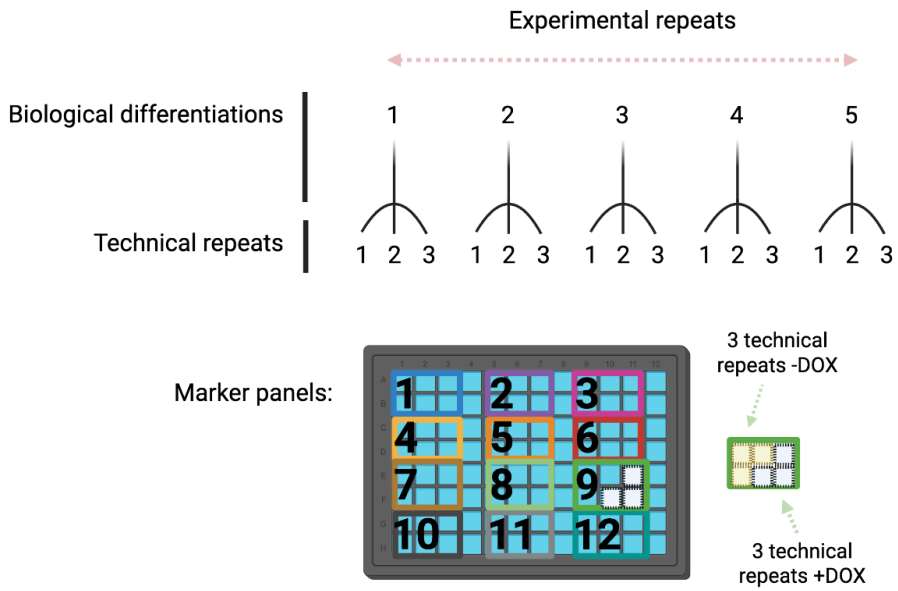

968

969 **Supplementary Figure 17. Experimental design of inducible TDP-43$^{\Delta NLS}$ related to Figure 4.** Five
970 experimental repeats (biological differentiations), with three technical repeats (wells) each. TDP-
971 43$^{\Delta NLS}$ without or with induction (±doxycycline, DOX). 12 marker panels per plate. Cells were seeded
972 into PLO-coated 96-well plates on day 4 post-differentiation and fixed on day 8 of differentiation. 250
973 site images were acquired per well. An exemplary plate design from a single experimental repeat
974 (biological differentiation) is depicted.

975

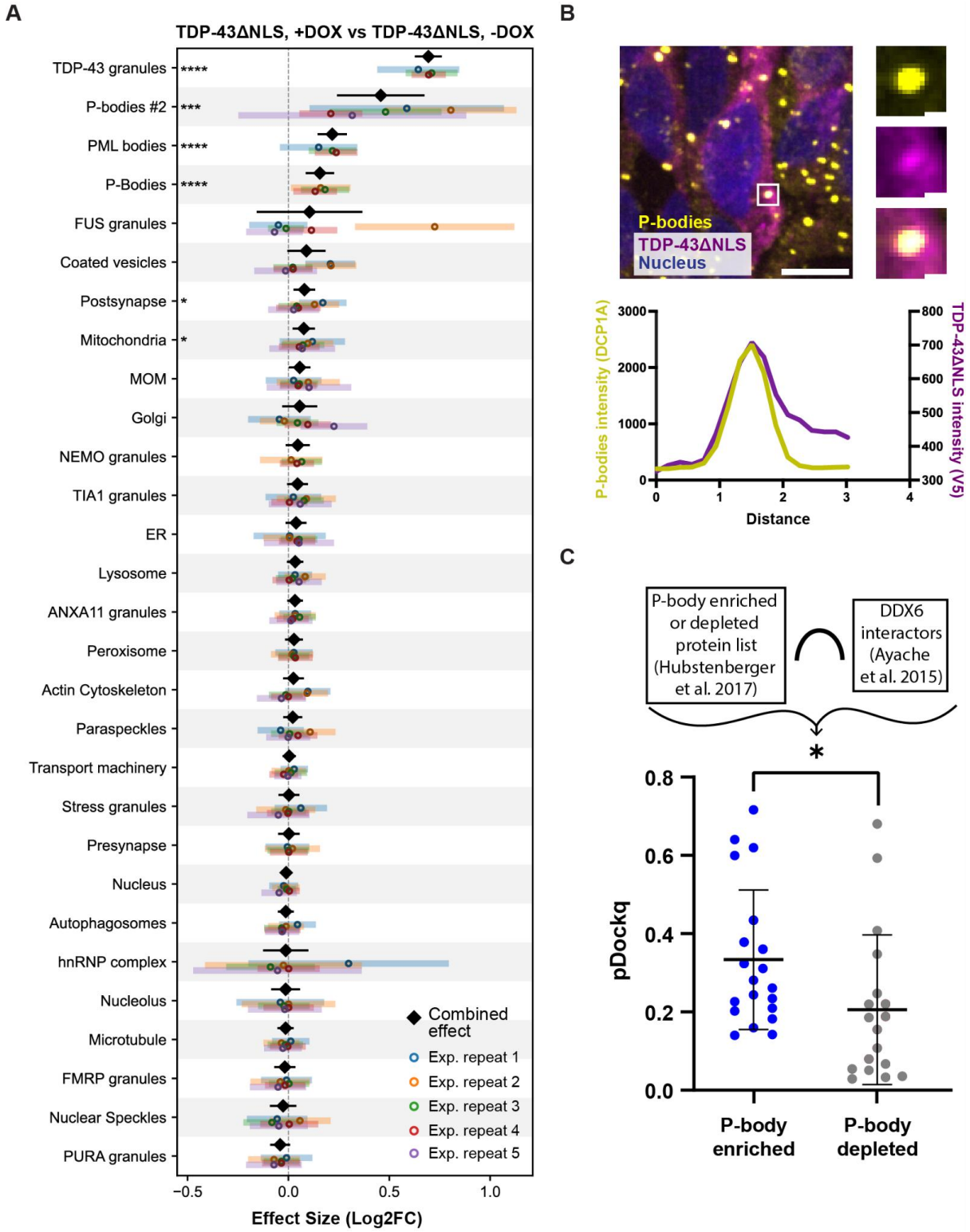
A
TDP-43ΔNLS, +DOX vs TDP-43ΔNLS, -DOX
TDP-43 granules
P-bodies #2
PML bodies
P-Bodies
FUS granules
Coated vesicles
Postsynapse
Mitochondria
MOM
Golgi
NEMO granules
TIA1 granules
ER
Lysosome
ANXA11 granules
Peroxisome
Actin Cytoskeleton
Paraspeckles
Transport machinery
Stress granules
Presynapse
Nucleus
Autophagosomes
hnRNP complex
Nucleolus
Microtubule
FMRP granules
Nuclear Speckles
PURA granules
Combined effect
Exp. repeat 1
Exp. repeat 2
Exp. repeat 3
Exp. repeat 4
Exp. repeat 5
Effect Size (Log2FC)
B
P-bodies
TDP-43ΔNLS
Nucleus
P-bodies intensity (DCP1A)
TDP-43ΔNLS intensity (V5)
Distance
C
P-body enriched or depleted protein list (Hubstenberger et al. 2017)
DDX6 interactors (Ayache et al. 2015)
pDockq
P-body enriched
P-body depleted

978 **Supplementary Figure 18. Cytoplasmic TDP-43–P-body interaction analyses in 8-day iPSC-derived**
979 **inducible TDP-43$^{\Delta NLS}$ neurons.**

980 **(A)** Stacked forest plot of organelle effect sizes ($\log_2$ fold change) in TDP-43$^{\Delta NLS}$ neurons with
981 doxycycline (+DOX) relative to without (–DOX). Five experimental repeats; 29 organelles analyzed.
982 Colored dots represent experimental repeat estimates, with horizontal bars showing 95% CI. The
983 combined effect estimate (μ) is shown as a black diamond with its 95% meta-analytic CI. Adjusted p-
984 values: * < 0.05, ** < 0.01, *** < 0.001, **** < 0.0001. ~280-6700 image tiles per
985 organelle/condition/experimental repeat. **(B)** Representative image showing colocalization of
986 cytoplasmic TDP-43$^{\Delta NLS}$ (V5 tag, purple) with P-bodies (DCP1A, yellow). Lens ×63; scale bar, 10 µm.
987 Insets show merged and separated channels of TDP-43$^{\Delta NLS}$ and a single P-body (scale bar, 1 µm) with
988 corresponding intensity profiles. **(C)** Predicted protein–protein interactions between TDP-43 and P-
989 body proteins using SpeedPPI. Y-axis: pDockQ interaction confidence score (Methods). P-body–
990 enriched proteins (blue) or depleted proteins (grey) were defined by Hubstenberger et al. and
991 identified as DDX6 interactors by immunoprecipitation. Mean: black horizontal line; error bars: SD. P-
992 value * < 0.05, Mann–Whitney U test.

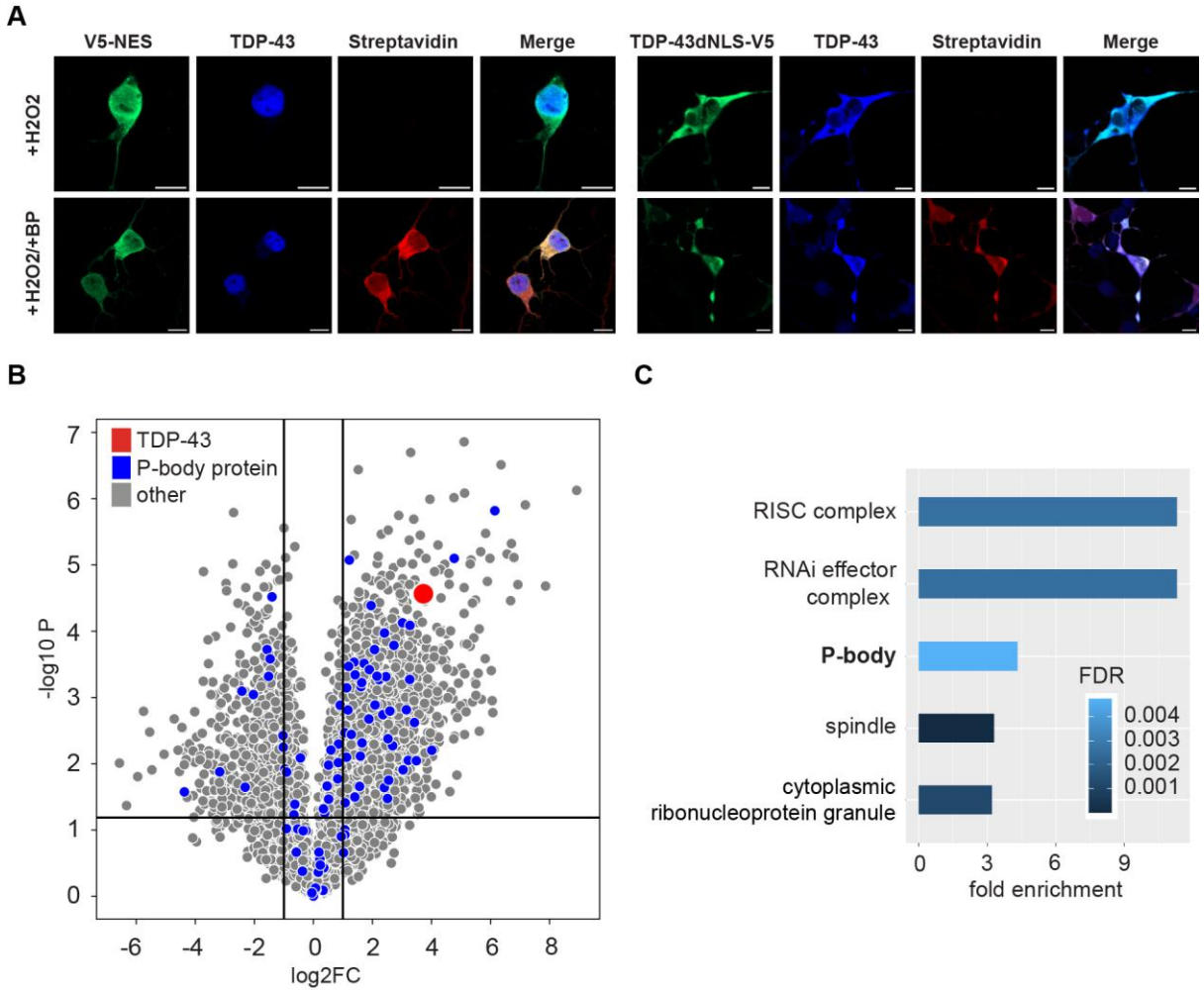

Supplementary Figure 19. Validation of APEX construct activity in 8-day iPSC-derived neurons.

(A) Immunostaining of neurons overexpressing APEX-V5-NES (+DOX, top) or TDP-43$^{\Delta NLS}$-V5-APEX (+DOX, bottom) without or with biotin phenol (BP) in the culture medium. V5-tagged construct (green), endogenous TDP-43 (blue), and biotinylated proteins (streptavidin, red). Lens ×63; scale bar, 10 µm. **(B)** Volcano plot of proteins enriched near TDP-43$^{\Delta NLS}$ compared to a cytoplasmic control construct (NES) after proximity labeling proteomics in 8-day neurons. Data from one of two independent experimental repeats (data of the other experiment shown in Figure 4G), each with 3–4 technical repeats per condition. P-body proteins (blue) as reported in ref. [116]; TDP-43 as positive control (red). Unpaired two-sided t-test. **(C)** Gene Ontology (GO) cellular component analysis (see Methods) of proteins interacting with TDP-43$^{\Delta NLS}$ in two independent proximity labeling experiments. The top five GO terms are shown. X-axis: statistical significance (FDR); colors: fold change.

1005

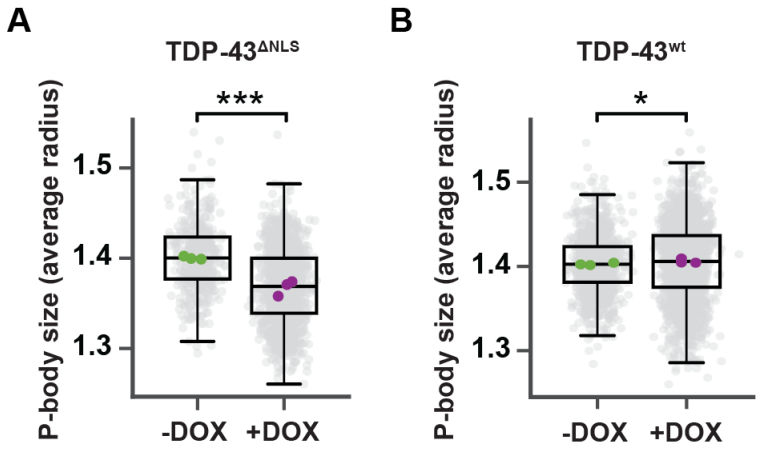

1006

1007 **Supplementary Figure 20. TDP-43$^{\Delta NLS}$ overexpression affects P-body size more than TDP-43^{wt}**
1008 **overexpression.**

1009 CellProfiler quantification of P-body size in polyclonal day 8 iPSC-derived neurons inducibly
1010 overexpressing **(A)** TDP-43$^{\Delta NLS}$ or **(B)** TDP-43^{wt} (±DOX; means = 1.4 (-DOX) vs. 1.368 (+DOX) or 1.403 (-
1011 DOX) vs. 1.406 (+DOX), respectively); P-body marker - DCP1A. Colored dots - experimental repeat
1012 means (-DOX; green, +DOX; purple); gray dots - site-level measurements. Three experimental repeats
1013 per condition. *$p < 0.05$, ***$p < 0.001$. Linear mixed-effects model with DOX as a fixed effect and
1014 experimental repeat as random intercept.

1015

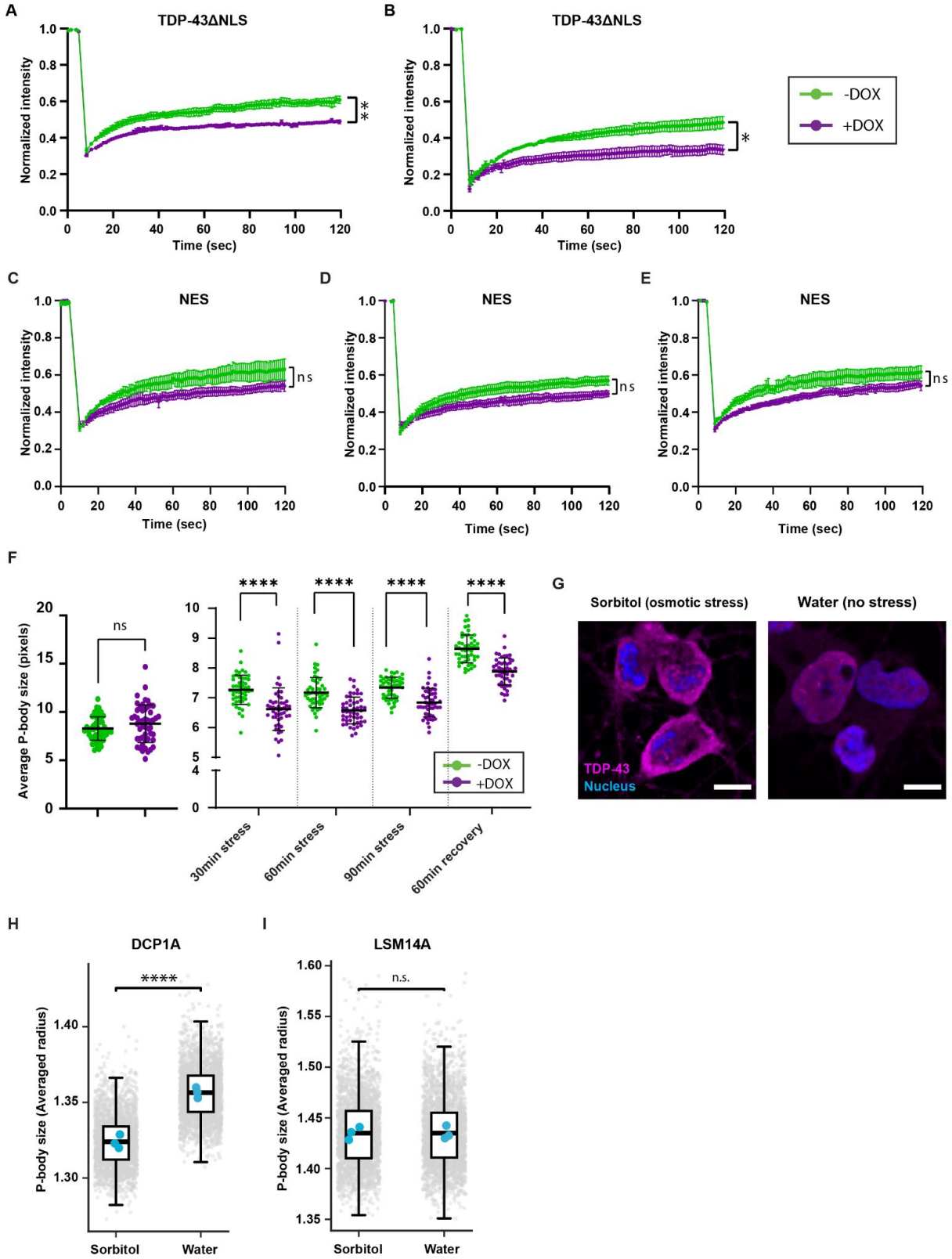

Supplementary Figure 21. Cytoplasmic TDP-43 disrupts P-body properties under stress in different cellular models.

FRAP analysis of YFP-DCP1A–labeled P-bodies in U2OS cells, partially photobleached ±DOX. **(A, B)** TDP-43$^{\Delta NLS}$ or **(C-E)** NES control. Fluorescence was normalized to baseline and recovery monitored over

1021 time (n = 4). Each data point represents the mean of 3–5 fields of view per repeat, with 2–9 P-bodies
1022 quantified per field. Two-way ANOVA with repeated measures and Geisser–Greenhouse correction;
1023 p-value * < 0.05, ** < 0.01; ns = not significant. **(F)** CellProfiler quantification of P-body size in U2OS
1024 cells expressing YFP-DCP1A with or without cytoplasmic TDP-43 (±DOX) under sodium arsenite stress
1025 (0.25 mM, 90 min) and recovery (60 min). n = 50 image fields/condition. Unpaired t-test; P-value ** <
1026 0.01, **** < 0.0001; ns = not significant. Horizontal black lines indicate means. **(G)** Immunostaining of
1027 day 8 iPSC-derived neurons (iW11) treated with carrier (water) or sorbitol (0.4 M, 2 hr) to induce
1028 mislocalization of endogenous TDP-43 (magenta) into the cytoplasm. Nucleus stained with Hoechst
1029 33342 (blue). Lens ×63; scale bar, 10 µm. CellProfiler quantification of P-body size per cell, using **(H)**
1030 DCP1A or **(I)** LSM14A, in iW11 neurons under basal vs. osmotic stress conditions (means (water vs.
1031 sorbitol) = 1.36 vs. 1.328 (DCP1A) or 1.439 vs. 1.439 (LSM14A)). Blue dots: experimental repeat means;
1032 gray dots: 250 site-level measurements per experimental repeat; three experimental repeats per
1033 condition. p-value **** < 0.0001. Linear model with sorbitol as fixed effect and experimental repeat
1034 as covariate; random-effect variance = 0.

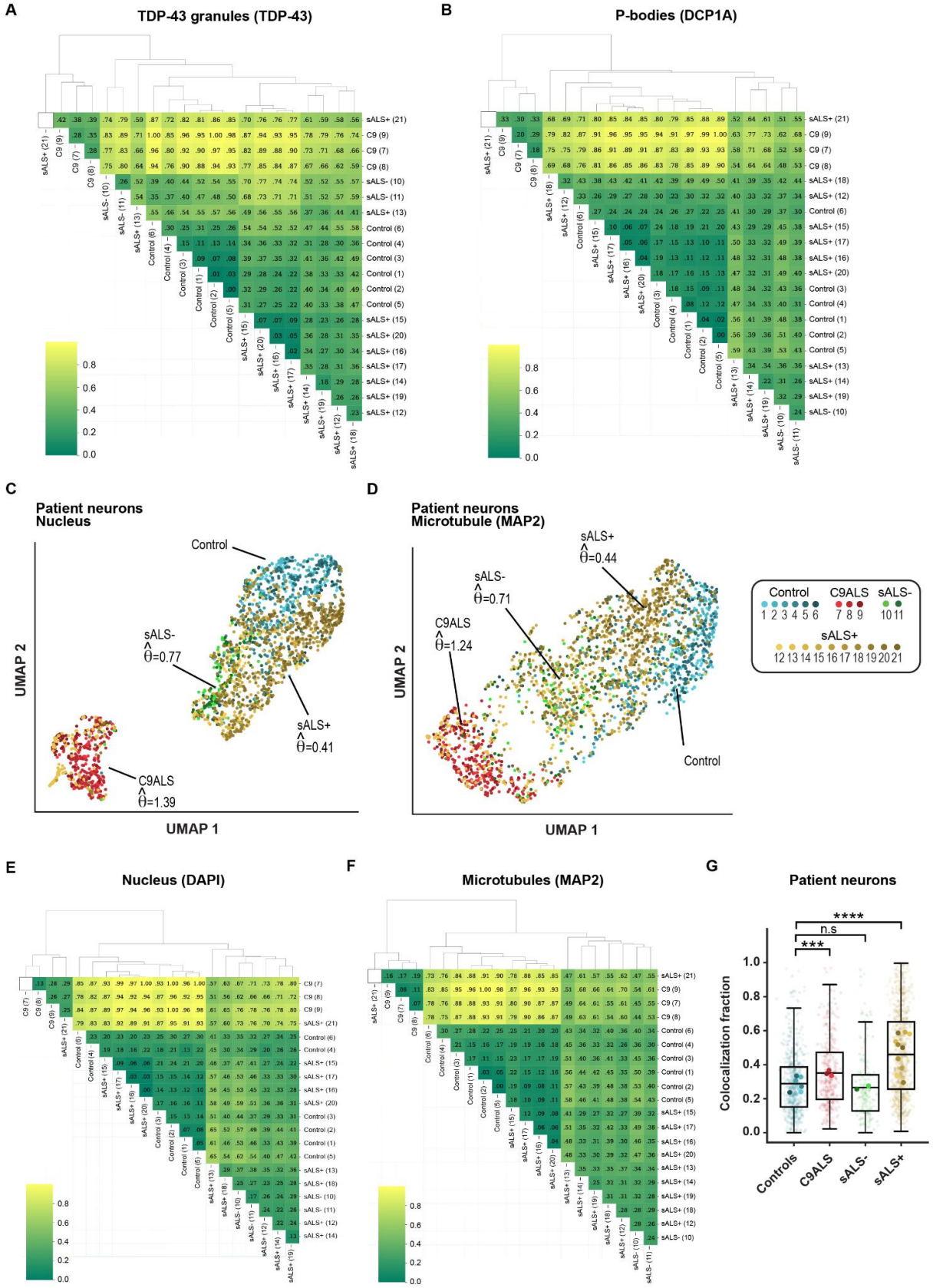
A
TDP-43 granules (TDP-43)
B
P-bodies (DCP1A)
C
Patient neurons
Nucleus
Control
sALS-
θ=0.77
sALS+
θ=0.41
C9ALS
θ=1.39
UMAP 2
UMAP 1
D
Patient neurons
Microtubule (MAP2)
sALS+
θ=0.44
sALS-
θ=0.71
C9ALS
θ=1.24
Control
UMAP 2
UMAP 1
Control
C9ALS
sALS-
1 2 3 4 5 6
7 8 9
10 11
sALS+
12 13 14 15 16 17 18 19 20 21
E
Nucleus (DAPI)
F
Microtubules (MAP2)
G
Patient neurons
****
n.s
***
Colocalization fraction
Controls
C9ALS
sALS-
sALS+

1035

1036

Supplementary Figure 22. Extended study in day 60 human motor neurons.

Pairwise Euclidean distances between NOVA-derived embeddings of **(A)** TDP-43 granules and **(B)** P-bodies were computed in the organellar landscapes shown in **Figure 5C**, **D** for each pair of human subjects. Heatmap values represent the median distance, rescaled to the [0,1] interval using min–max normalization. A value of 0 indicates the closest subjects (highest similarity, darker colors), and 1 the most distant (lowest similarity, lighter colors). Rows and columns were clustered by agglomerative hierarchical clustering of the scaled distance values (Euclidean distance, average linkage). Dendrograms depict the hierarchical relationships among human subjects. UMAP projections of day 60 motor neurons from a cohort of 21 human subjects, showing **(C)** the nucleus (hoechst 33342) or **(D)** Microtubule (MAP2). Points - single image tiles. ($\hat{\theta}$) the effect size estimate. Pairwise Euclidean distances between NOVA-derived embeddings of **(E)** nucleus and **(F)** microtubules. **(G)** Boxplots of P-body-positive (DCP1A) pixels that are also positive for TDP-43. Colocalization fraction in human subjects day 60 motor neuron images in C9ALS, sALS-, or sALS+ vs. healthy controls (mean fraction overlap = 0.35, 0.265 or 0.46 vs. 0.288, respectively). ~60-160 image tiles per human subject; Linear fixed-effects model with human subject-clustered standard errors (fallback used); *** $p < 0.001$, **** $p < 0.0001$. Large dots - condition mean per experimental repeat; small dots - individual images; Three human subjects per group.

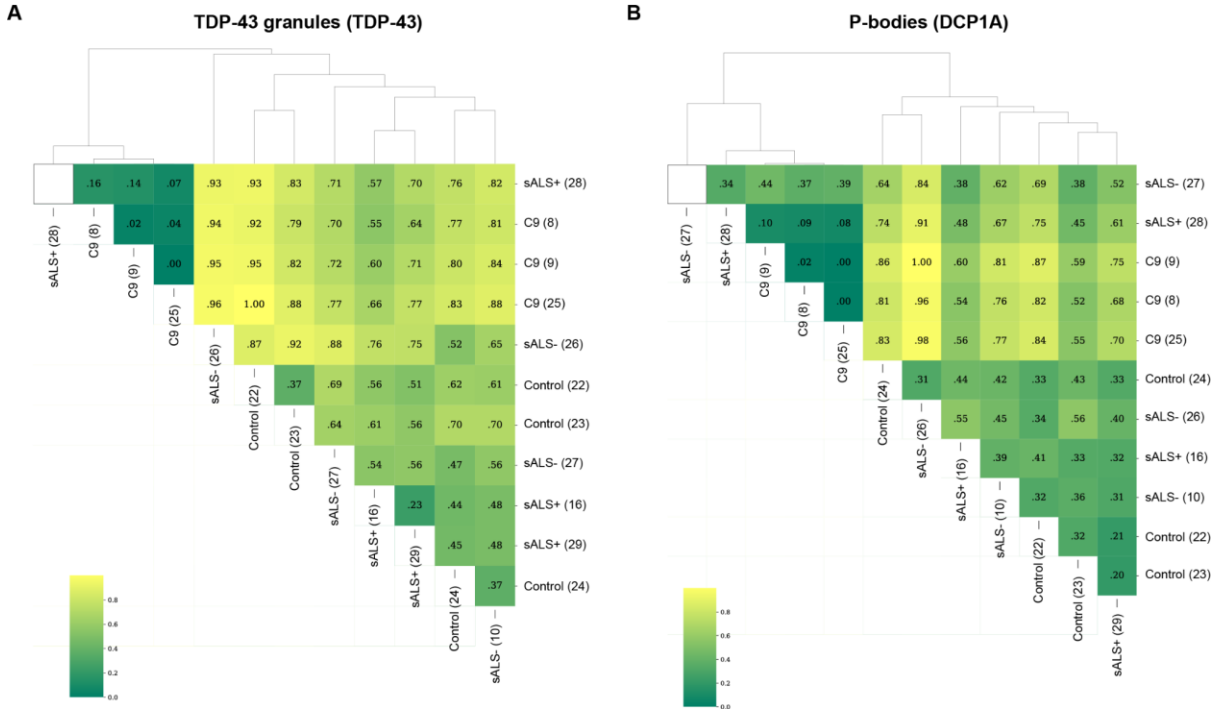

Supplementary Figure 23. Distances for TDP-43 granules and P-bodies across the human subjects in the extended study of day 60 human motor neurons.

Pairwise Euclidean distances between NOVA-derived embeddings of **(A)** TDP-43 granules and **(B)** P-bodies were computed in the organellar landscapes shown in **Figure 5G, H** for each pair of human subjects. Heatmap values represent the median distance, rescaled to the [0,1] interval using min–max normalization. A value of 0 indicates the closest subjects (highest similarity, darker colors), and 1 the most distant (lowest similarity, lighter colors). Rows and columns were clustered by agglomerative hierarchical clustering of the scaled distance values (Euclidean distance, average linkage). Dendrograms depict the hierarchical relationships among human subjects.

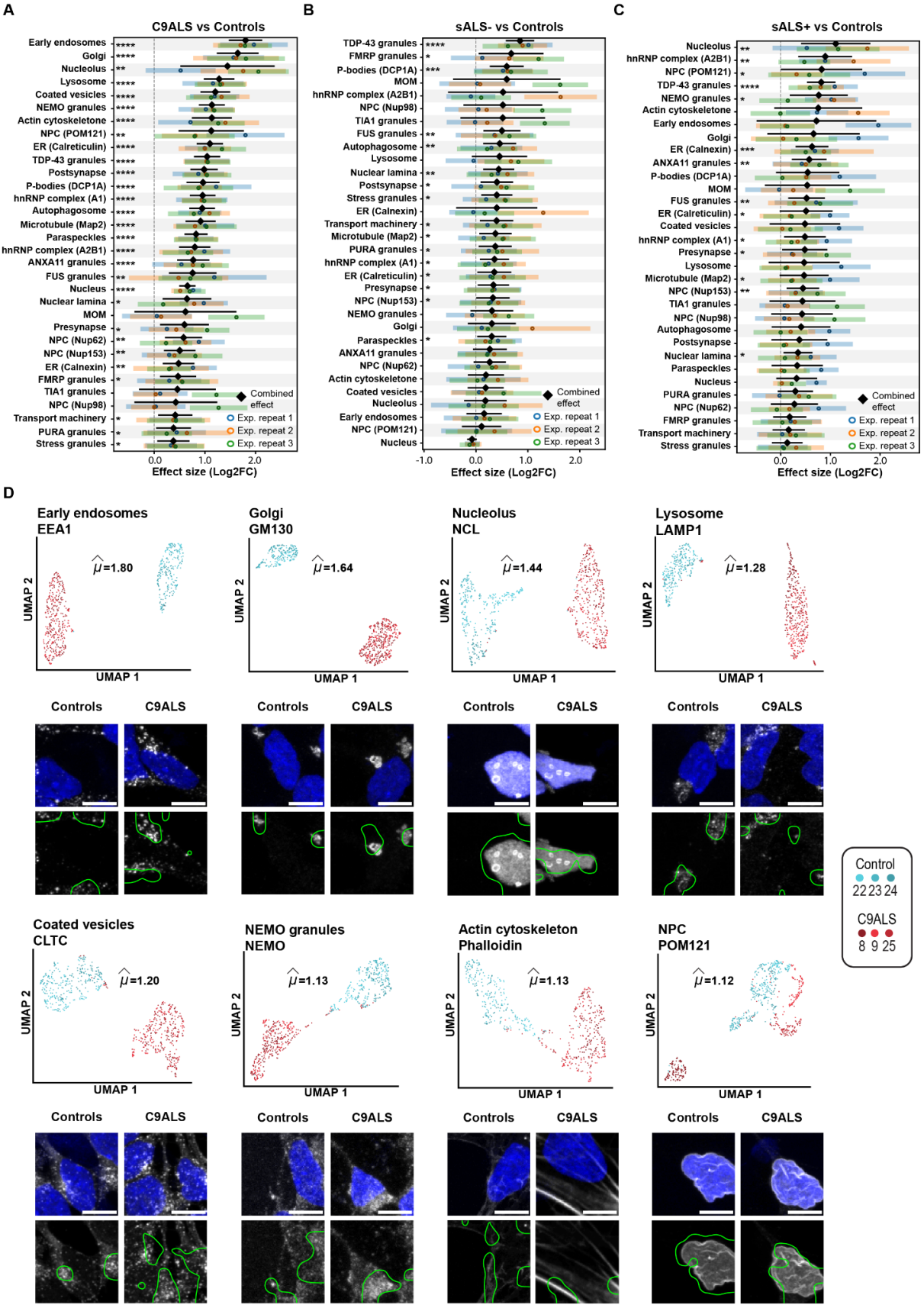
A
C9ALS vs Controls
Early endosomes ****
Golgi ****
Nucleolus **
Lysosome ****
Coated vesicles ****
NEMO granules ****
Actin cytoskeletone ****
NPC (POM121) **
ER (Calreticulin) ****
TDP-43 granules ****
Postsynapse ****
P-bodies (DCP1A) ****
hnRNP complex (A1) ****
Autophagosome ****
Microtubule (Map2) ****
Paraspeckles ****
hnRNP complex (A2B1) ****
ANXA11 granules ****
FUS granules **
Nucleus ****
Nuclear lamina *
MOM
Presynapse *
NPC (Nup62) **
NPC (Nup153) **
ER (Calnexin) **
FMRP granules *
TIA1 granules
NPC (Nup98)
Transport machinery *
PURA granules *
Stress granules *
Combined effect
Exp. repeat 1
Exp. repeat 2
Exp. repeat 3
0.0 1.0 2.0
Effect size (Log2FC)
B
sALS- vs Controls
TDP-43 granules ****
FMRP granules *
P-bodies (DCP1A) ***
MOM
hnRNP complex (A2B1)
NPC (Nup98)
TIA1 granules
FUS granules **
Autophagosome **
Lysosome
Nuclear lamina **
Postsynapse *
Stress granules *
ER (Calnexin)
Transport machinery *
Microtubule (Map2) *
PURA granules *
hnRNP complex (A1) *
ER (Calreticulin) *
Presynapse *
NPC (Nup153) *
NEMO granules
Golgi
Paraspeckles *
ANXA11 granules
NPC (Nup62)
Actin cytoskeletone
Coated vesicles
Nucleolus
Early endosomes
NPC (POM121)
Nucleus
Combined effect
Exp. repeat 1
Exp. repeat 2
Exp. repeat 3
-1.0 0.0 1.0 2.0
Effect size (Log2FC)
C
sALS+ vs Controls
Nucleolus **
hnRNP complex (A2B1) **
NPC (POM121) *
TDP-43 granules ****
NEMO granules *
Actin cytoskeletone
Early endosomes
Golgi
ER (Calnexin) ***
ANXA11 granules **
P-bodies (DCP1A)
MOM
FUS granules **
ER (Calreticulin) *
Coated vesicles
hnRNP complex (A1) *
Presynapse *
Lysosome
Microtubule (Map2) *
NPC (Nup153) **
TIA1 granules
NPC (Nup98)
Autophagosome
Postsynapse
Nuclear lamina *
Paraspeckles
Nucleus
PURA granules
NPC (Nup62)
FMRP granules
Transport machinery
Stress granules
Combined effect
Exp. repeat 1
Exp. repeat 2
Exp. repeat 3
0.0 1.0 2.0
Effect size (Log2FC)
D
Early endosomes
EEA1
μ̂=1.80
Golgi
GM130
μ̂=1.64
Nucleolus
NCL
μ̂=1.44
Lysosome
LAMP1
μ̂=1.28
UMAP 2
UMAP 1
Controls
C9ALS
Coated vesicles
CLTC
μ̂=1.20
NEMO granules
NEMO
μ̂=1.13
Actin cytoskeleton
Phalloidin
μ̂=1.13
NPC
POM121
μ̂=1.12
Control
22 23 24
C9ALS
8 9 25

1071

1072

1073 **Supplementary Figure 24. Comprehensive organellar response of day 60 human subject-derived**
1074 **motor neurons.**

1075 Stacked forest plot of organelle effect sizes (log_2 fold change) in day 60 motor neurons from **(A)** C9ALS,
1076 **(B)** sALS without cytoplasmic TDP-43 (sALS–), and **(C)** sALS with cytoplasmic TDP-43 (sALS+), relative
1077 to healthy controls. Twelve human subjects were analyzed (three per group); 32 organelles were
1078 studied. Colored dots represent group-wise effect estimates, with horizontal bars indicating 95% CI.
1079 The combined effect estimate ($\hat{\mu}$) is shown as a black diamond with its 95% meta-analytic CI,
1080 accounting for between-experimental repeat variance. Adjusted P-values: * < 0.05, ** < 0.01, *** <
1081 0.001, **** < 0.0001. ~45-170 image tiles per organelle/human subject. **(D)** UMAP projection of day
1082 60 motor neurons from C9ALS patients (n = 3) and healthy controls (n = 3), highlighting early
1083 endosomes, Golgi, nucleolus, lysosome, coated vesicles, NEMO granules, actin cytoskeleton and the
1084 nuclear pore complex (NPC), related to the autophagy and endosomal–lysosomal pathway. Each point
1085 represents a single image tile (~55 tiles per human subject per organelle). Effect size estimates (μ) are
1086 indicated. Representative images with nuclei (Hoechst 33342) and overlaid model attention maps for
1087 each organelle/group. Lens ×63; scale bar, 10 μm.

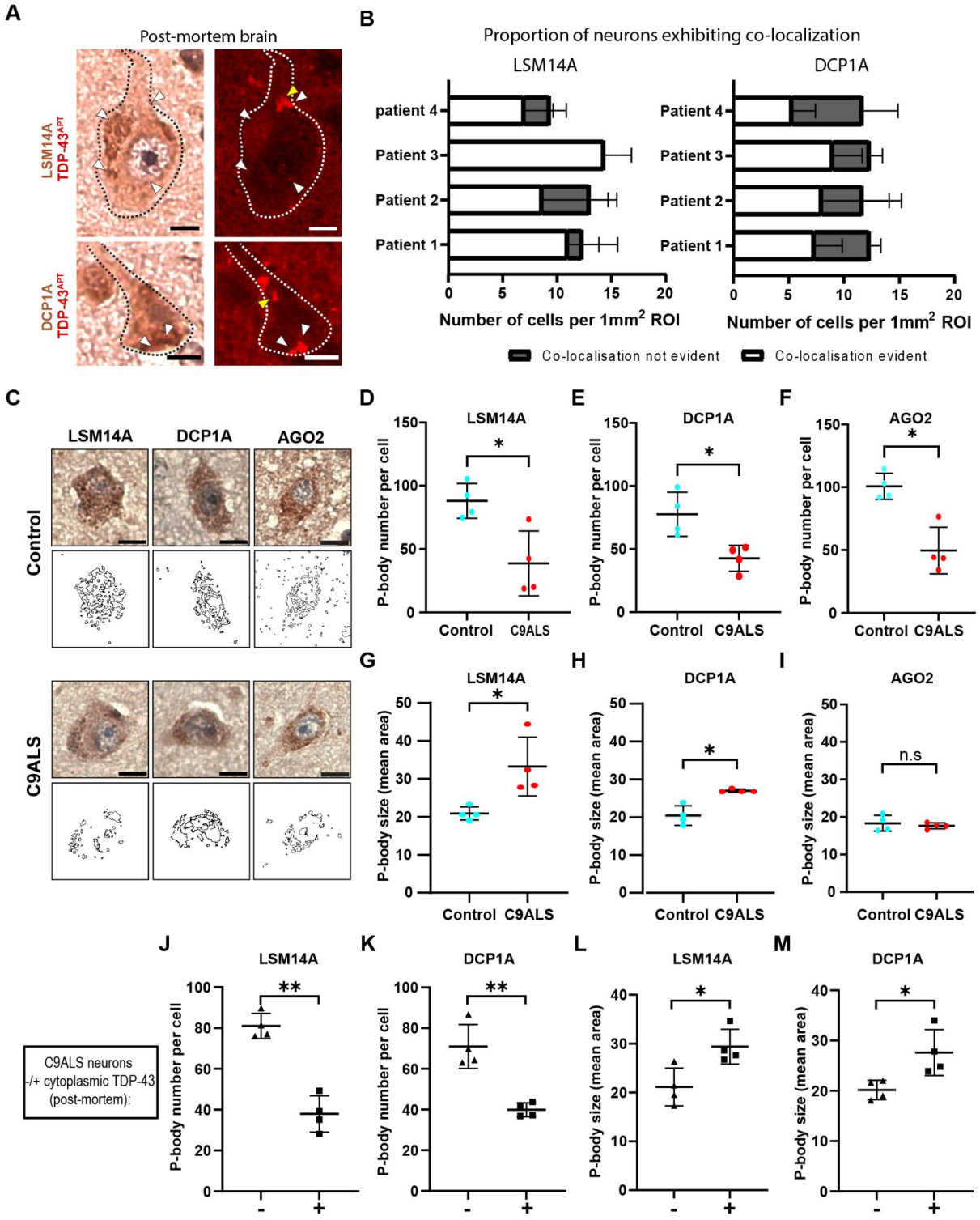

Supplementary Figure 25. TDP-43 interacts with P-bodies in ALS post-mortem tissue.

(A) Images of C9ALS neurons showing cytoplasmic TDP-43 (aptamer[139], red) colocalized with P-body markers LSM14A or DCP1A (chromogenic IHC). Yellow arrowheads: TDP-43 without colocalization; white arrowheads: with colocalization. Scale bar, 10 µm. **(B)** Quantification of neurons with (white bars) or without (grey bars) TDP-43-P-body colocalization (LSM14A, left; DCP1A, right) across four patients per region of interest (ROI) = 1 mm². Mean of three ROIs/patient; error bars, SD; analysis by

1095 ImageJ. **(C)** Representative DAB IHC of P-body proteins (DCP1A, LSM14A, AGO2) in C9ALS motor cortex
1096 (lower panels) vs. controls (upper panels). Scale bar, 10 µm. Quantification of mean P-body number
1097 **(D–F)** and size **(G–I)** per cell per subject (4 C9ALS patients (red) compared to 4 controls (blue)). Median
1098 P-body number (control vs C9ALS) = 85.95 vs 31.20 (LSM14A) or 75.15 vs 45.50 (DCP1A) or 98.20 vs
1099 43.90 (AGO2); median P-body size (control vs C9ALS) = 20.60 vs 30.35 (LSM14A) or 20.00 vs 26.80
1100 (DCP1A) or 18.00 vs 17.75 (AGO2). Mann–Whitney U test; *$p < 0.05$; ns = not significant. Scatter plots
1101 show means (black lines) ± SD. Each point represents one subject. Quantification of mean number **(J,**
1102 **K)** and size area **(L, M)** of P-bodies (LSM14A or DCP1A) in neurons without (-, triangle) or with (+,
1103 square) cytoplasmic TDP-43 within each of the C9ALS patients (mean P-body number (- vs. +) = 81.02
1104 vs. 37.252 (LSM14A) or 68.04 vs. 39.9 (DCP1A); mean P-body size area (- vs. +) = 21.12 vs. 30 (LSM14A)
1105 or 20.19 vs. 26.99 (DCP1A)). Nested t-test; *$p < 0.05$, **$p < 0.01$. Scatter plots show means (black lines)
1106 ± SD. Each point represents one subject (n = 4).

1107

1108 ## Material & Methods

1109

1110 **Cell lines**

1111 **1. Cancer cell lines and iNDI lines**

#	Cell line	Reference / gift
1	KOLF2.1J human iPSC	[169]
2	TDP-43$^{\Delta NLS}$-V5-APEX NGN2-iPSC	This study
3	TDP-43^{wt}-V5-APEX NGN2-iPSC	This study
4	NES-V5-APEX NGN2-iPSC	This study
5	U2OS stably expressing YFP-DCP1A	A gift from Nancy Kedersha Pavel Ivanov and Paul Anderson, Harvard Medical School
6	U2OS stably expressing UBAP2L-ruby and /inducibly expressing TDP-43$^{\Delta NLS}$-clover	[111]A gift from Don W Cleveland, University of California, San Diego
7	*TARDBP* M337V SNV/SNV	[98]
8	*OPTN* Q398E SNV/SNV	[98] Gift from Michael Ward, National Institutes of Health
9	*TBK1* E696K SNV/SNV	[98]
10	*FUS* R495* SNV/SNV	[98]
11	*FUS* R495* SNV/WT	[98]
12	*FUS* R495* Rev/WT	[98]
13	*SNCA* E46K SNV/SNV	[98]

1112

1113 **2. Patient-derived iPSC lines including demographic Information**

#	iPSC Line Name	Source	Clinical Diagnosis	Age at Time of	Sex	Origin

				Collection		
1	CS0002	Cedars-Sinai	Non-neurologic control	51	Male	PBMC
2	CS0201	Cedars-Sinai	Non-neurologic control	56	Female	PBMC
3	CS1ATZ	Cedars-Sinai	Non-neurologic control	60	Male	PBMC
4	CS2AE8	Cedars-Sinai	Non-neurologic control	50	Female	PBMC
5	CS8PAA	Cedars-Sinai	Non-neurologic control	58	Female	PBMC
6	CS9XH7	Cedars-Sinai	Non-neurologic control	53	Male	PBMC
7	EDi022-A	Cedars-Sinai	Non-neurologic control	79	Male	PBMC
8	EDi029-A	Cedars-Sinai	Non-neurologic control	80	Male	PBMC
9	EDi037-A	Cedars-Sinai	Non-neurologic control	79	Male	PBMC
10	CS0JGZ	Cedars-Sinai	sALS	56	Male	PBMC
11	CS3EPR	Cedars-Sinai	sALS	60	Female	PBMC
12	CS3XLK	Cedars-Sinai	sALS	55	Female	PBMC
13	CS4PFR	Cedars-Sinai	sALS	72	Female	PBMC
14	CS4ZCD	Cedars-Sinai	sALS	53	Male	PBMC
15	CS5JPF	Cedars-Sinai	sALS	55	Female	PBMC
16	CS5ZHY	Cedars-Sinai	sALS	64	Male	PBMC
17	CS6PYD	Cedars-Sinai	sALS	69	Female	PBMC
18	CS8JGP	Cedars-Sinai	sALS	61	Male	PBMC
19	CS9GXD	Cedars-Sinai	sALS	68	Male	PBMC
20	CS2FN3	Cedars-Sinai	sALS	58	Male	PBMC
21	CS7TN6	Cedars-Sinai	sALS	33	Male	PBMC
22	CS0JPP	Cedars-Sinai	sALS	61	Male	PBMC
23	CS4MLT	Cedars-Sinai	sALS	54	Male	PBMC
24	CS6ZU8	Cedars-Sinai	sALS	61	Male	PBMC
25	CS0ANK	Cedars-Sinai	sALS	65	Male	PBMC
26	CS0BUU	Cedars-Sinai	*C9orf72*	63	Female	PBMC
27	CS2YNL	Cedars-Sinai	*C9orf72*	60	Male	PBMC
28	CS7VCZ	Cedars-Sinai	*C9orf72*	64	Male	PBMC
29	CS8RFT	Cedars-Sinai	*C9orf72*	62	Male	PBMC

Human post-mortem brain tissue samples

Case Number	GUID/Block number	Source	Clinical Diagnosis	Age at Death	Sex
GBB-19-14	NEUNC276RND	Target ALS post-mortem core	Control	67	Male
GBB-16-10	NEUCG551GV1	Target ALS post-mortem core	Control	57	Female
GBB-18-13	NEUGV102NYT	Target ALS post-mortem core	Control	63	Female
GBB-17-22	NEUGJ583BEE	Target ALS post-mortem core	Control	70	Male
LP005/2007	AD	Sheffield Brain bank	Control	63	Male
LP085/2007	C	Sheffield Brain bank	Control	59	Female
LP098/2007	C	Sheffield Brain bank	Control	68	Male
PA135/2018	A1	Sheffield Brain bank	Control	85	Female

PA058/2022	A19	Sheffield Brain bank	Control	68	Female
PA154/2022	A13	Sheffield Brain bank	Control	97	Female
GBB-18-07 (Georgetown Case)	NEUGU437VNF	Target ALS post-mortem core	*C9orf72*	66	Female
GWF15-09	NEUTP019MY9	Target ALS post-mortem core	*C9orf72*	61	Female
GWF18-31	NEUKN179PH8	Target ALS post-mortem core	*C9orf72*	62	Female
GBB-18-17 (Georgetown case)	NEUBE992ZD1	Target ALS post-mortem core	*C9orf72*	68	Male
LP045/2006	A	Sheffield Brain bank	*C9orf72*	46	Male
LP066/2008	B	Sheffield Brain bank	*C9orf72*	59	Female
LP005/2011	C	Sheffield Brain bank	sALS	76	Female
NA009/1996	L	Sheffield Brain bank	sALS	78	Female
LP020/2013	A2	Sheffield Brain bank	sALS	78	Male
LP024/2008	B	Sheffield Brain bank	sALS	63	Female
LP027/2008	C	Sheffield Brain bank	sALS	70	Female
LP039/2005	B	Sheffield Brain bank	sALS	57	Female

1116

1117 **Primary antibodies used**

#	Target	Antibody #	Species	Company	Dilution
1	AGO2	ab32381	rabbit	Abcam	1:200
2	ANXA11	HPA027545	rabbit	Atlas antibodies	1:200 / 3 µg/ml / 1:500
3	Calnexin	2679S	rabbit	Cell Signaling	1:500
4	Calreticulin	ab2907	rabbit	Abcam	3 µg/ml
5	Calreticulin	ab92516	rabbit	Abcam	1:200 / 1:500
6	CLTC	ab21679	rabbit	Abcam	1:200 / 0.75 µg/ml / 1:500
7	DAPI	62248		Thermo Fisher	1:3000
8	DCP1A	PA5-82478	rabbit	Invitrogen	0.55 µg/ml
9	DCP1A	H00055802-M06	mouse	Novus Biologicals	1:500
10	DCP1A	ab47811	rabbit	Abcam	1:200
11	EEA1	3288S	rabbit	Cell Signaling	1:500

12	FMRP	ab17722	rabbit	Abcam	1:200 / 10 µg/ml / 1:500
13	FUS	sc-47711	mouse	Santa Cruz	1:200 / 0.4 µg/ml / 1:500
14	G3BP1	sc-365338	mouse	Santa Cruz	1:200 / 0.4 µg/ml / 1:500
15	GM130	610822	mouse	BD	1:200 / 1.7 µg/ml / 1:500
16	hnRNP A1	sc-32301	mouse	Santa Cruz	1:200 / 1:1000
17	hnRNP A2B1	sc-53531	mouse	Santa Cruz	1:1000
18	Hoechst 33342	62249		Thermo Fisher	1:8000
19	KIF5A	ab5628	rabbit	Abcam	1:200 / 4 µg/ml / 1:500
20	Lamin B1	66095-1-Ig	mouse	Proteintech	1:500
21	LAMP1	ab25630	mouse	Abcam	1:10 / 0.4 µg/ml
22	LAMP1	9091S	rabbit	Cell Signaling	1:500
23	LSM14A	18336-1-AP	rabbit	Proteintech	1:100
24	LSM14A	HPA017961	rabbit	Atlas Antibodies	1:200
25	MAP2	188 004	guinea pig	Synaptic Systems	1:1000
26	Mitotracker	M22426		Invitrogen	1:20000
27	NCL	14574S	rabbit	Cell Signaling	1:200 / 0.15 µg/ml / 1:500
28	NEMO/Ikkgamma	611306	mouse	BD	1:200 / 5 µg/ml / 1:500
29	NONO/p54nrb	GTX19407	mouse	GeneTex	1:200 / 1:250 / 1:500
30	Nup153	sc-101544	rat	Santa Cruz	1:500
31	Nup62	MABE1043	rat	Millipore	1:500
32	Nup98	ab50610	rat	Abcam	1:500
33	Phalloidin	A12379		Thermo Fisher	1:7500
34	Phalloidin	A12380		Thermo Fisher	1:5000

35	PEX14	abc142	rabbit	EMD Millipore	1:200 / 1:300
36	PML	sc-966	mouse	Santa Cruz	1:200 / 2 µg/ml
37	PSD95 (K28/43 / DLG4)	75-028	mouse	Neuromab	1:200 / 10 µg/ml
38	PSD95	124 308	rat	Synaptic Systems	1:500
39	PURA	12D11	rat	Gift from Dierk Niessing, Helmholtz Munich	undiluted
40	PURA	MA519766	mouse	Thermo Fisher Scientific	1:500
41	PURA	ab79936	rabbit	Abcam	1.5 µg/ml
42	POM121	NBP2-19890	rabbit	Novus Biologicals	1:250
43	SNCA	ab1903	mouse	Abcam	1:200 / 7.5 µg/ml / 1:500
44	SON	HPA023535	rabbit	MERCK/Sigma-aldrich	1:400
45	SQSTM1	ab56416	mouse	Abcam	1:200 / 10 µg/ml / 1:500
46	TDP-43	10782-2-AP	rabbit	Proteintech	1:200 / 0.5 µg/ml / 1:500
47	TDP-43	60019-2-Ig	mouse	Proteintech	1:200
48	TIA-1	sc-166247	mouse	Santa Cruz	4 µg/ml / 1:500
49	TOMM20	ab78547	rabbit	Abcam	1:200 / 1 µg/ml / 1:500
50	Tubulin	ab6161	rat	Abcam	1:500
51	TUJ1/Tubulin β-3 (Custom ordered in PBS based on Cat# 801201; then pre-labeled with CF640R)	98130	mouse	BioLegend	1:300

1118

1119 **Secondary antibodies used**

#	Name	Antibody #	Species (against)	Company	Dilution
1	Anti-rat-Cy2	712-545-153	rat	Jackson ImmunoResearch	1:200
2	Anti-rat CF568	20092	rat	Biotium	1:1000
3	Anti-rabbit-Cy5	711-175-152	rabbit	Jackson ImmunoResearch	1:200
4	Anti-rabbit-Cy3	711-165-152	rabbit	Jackson ImmunoResearch	1:200
5	Anti-rabbit-Cy2	711-225-152	rabbit	Jackson ImmunoResearch	1:200
6	Anti-rabbit-Alexa Fluor 488	A11034	rabbit	Thermo Fisher Scientific	1:200
7	Anti-rabbit CF488A	20019	rabbit	Biotium	1:500
8	Anti-rabbit CF568	20103	rabbit	Biotium	1:1000
9	Anti-rabbit CF640R	20178	rabbit	Biotium	1:1000
10	Anti-mouse-Alexa Fluor 647	A21236	mouse	Thermo Fisher Scientific	1:200
11	Anti-mouse-Cy5	715-175-150	mouse	Jackson ImmunoResearch	1:200
12	Anti-mouse-Cy3	715-165-150	mouse	Jackson ImmunoResearch	1:200
13	Anti-mouse-Cy2	715-225-150	mouse	Jackson ImmunoResearch	1:200
14	Anti-mouse CF488A	20018	mouse	Biotium	1:500
15	Anti-mouse CF568	20101	mouse	Biotium	1:1000
16	Anti-guinea pig-Alexa Fluor 568	A11075	guinea pig	Thermo Fisher Scientific	1:200

17	Alexa Fluor Phalloidin-488	A12379	-	Thermo Fisher Scientific	1:1000

1120

1121 **Primary antibody labeling kit**

1122

Kit name	Provider	Catalog number
CF640R antibody labeling kit	Biotium	92278

1123

1124 **Experimental methods**

1125 **Generation of polyclonal NGN2 iNDI lines**

1126 Prior to transfection, 0.4-0.5 million iPSCs were seeded into a well of a 6-well plate, allowing for 12-24
1127 hours for cell attachment. PG-TO-hNGN2 plasmid (Gift from Michael Ward, Addgene plasmid
1128 #172115) was transfected with TransfeX Transfection Reagent (ATCC® ACS-4005™) along with
1129 piggyBac™ transposase vector. Plasmid DNA and Opti-MEM I Reduced-Serum Medium (Gibco 31985-
1130 047) were equilibrated to room temperature and were gently mixed to avoid foaming or damaging
1131 the reagents. A total of 2µg of DNA was introduced per well, with a donor-to-transposase ratio of 2:1.
1132 Next, 100ul of Opti-MEM I Reduced-Serum Medium was dispensed into a sterile microcentrifuge tube,
1133 along with the donor and transposase plasmids. Then, 3ul of TransfeX Transfection Reagent ACS-4005
1134 was incorporated into the DNA mixture and was mixed thoroughly using gentle pipetting. A mini
1135 centrifuge was used briefly to consolidate the tube's contents. The resultant lipo:DNA complexes were
1136 allowed to incubate at room temperature for 15-30 minutes, promoting the formation of transfection-
1137 ready complexes. The complexes were carefully added drop-wise to the iPSCs, ensuring diverse
1138 coverage within the well for optimal transfection efficiency. The cells were then incubated at 37°C
1139 with 5% CO2 for 24 hours. At 24 hours post-transfection, a complete media change was made and 0.4
1140 ug/ml of puromycin (InvivoGen ant-pr-1) was added to the media. Media supplemented with 0.4
1141 ug/ml of puromycin was replaced every day for 2-3 days until only BFP-expressing cells remained in
1142 the culture.

1143 **Generation of inducible TDP-43$^{\Delta NLS}$ and TDP-43^{wt} iPS cell lines**
1144 We generated iPS cell lines based on iW11-NGN2 (gift from Michael Ward [170]) featuring a doxycycline-
1145 inducible APEX construct [171] fused to either wild-type (TDP-43^{wt}) or NLS-mutated TDP-43 (TDP-43$^{\Delta NLS}$)
1146 (Addgene plasmid #229081), and nuclear export signal (NES) (Addgene plasmid #229082) as
1147 cytoplasmic control. A V5 tag was included to enable visualization by microscopy. After cloning these
1148 constructs into the PG-TO-hNGN2 plasmid in the place of NGN2, the cassette was integrated into the
1149 genome via the piggyBac transposon system described above. After introducing the plasmid, we
1150 carefully selected clones and cultivated them according to established protocols. The differentiation
1151 process followed the described methodology, with the induction of cytoplasmic TDP-43$^{\Delta NLS}$ achieved
1152 by adding doxycycline (2 ug/ml) for 24 hours.

1153 **Human iPSC culture (NGN2 lines)**

1154 iPSCs were grown at 37°C with 5% CO2 on tissue culture dishes coated with Geltrex (Gibco, A1413302)
1155 for at least 1 hour at 37°C. Cell culture media was exchanged daily with mTeSR1 medium (STEMCELL
1156 Technologies, 85850). For passaging, iPSCs were dissociated with accutase (ThermoFisher Scientific,
1157 A1110501) and seeded into mTeSR1 supplemented with ROCK inhibitor Y-27632 (Tocris Bioscience,
1158 1254). Cells were frozen in mTeSR1 supplemented with 30% KnockOut Serum Replacement
1159 (ThermoFisher Scientific, 1082802) and 10% DMSO

1160

1161 **Differentiation of iPSCs to day 8 neurons (NGN2 lines)**

1162 Differentiation was performed as in [170] with minor adjustments. Briefly, after thawing, cells were
1163 transferred to tubes with DPBS, centrifuged, and resuspended in culture medium before seeding onto
1164 one Geltrex (Gibco, A1413302) coated well of a 6-well plate. Media was supplemented with 10 µM
1165 ROCK inhibitor (Y-27632, Tocris Bioscience 1254) for cell survival. During expansion, cells were
1166 cultured with daily media replacements of mTeSR1 medium (STEMCELL Technologies, 85850). Upon
1167 reaching 70%-80% confluency, cells were transferred to larger plates in preparation for induction. On
1168 the day of differentiation induction, cells were seeded with ROCK inhibitor (Tocris Bioscience, 1254,
1169 10 µM) supplemented to induction medium comprising DMEM/F12, HEPES (Gibco, 11330032), N2
1170 supplement (Gibco, 17502048), NEAA (Gibco, 11140050), L-glutamine (Gibco, 25030081), and freshly
1171 prepared doxycycline solution (2mg/ml stock, Sigma D9891). Based on plate size, either 1.5 million or
1172 2.5 million cells were seeded, targeting 5 million and 15 million neurons, respectively. On induction
1173 days 1-3 induction media was replaced daily. For maturation starting from day 3 onwards, overnight
1174 PDL-coated (sigma, P7405, 0.04mg/ml) or Poly-L-Ornithine (PLO)-coated (Sigma Aldrich, P4957) 96-
1175 well plates (Brooks, MGB096-1-2-LG-L or Revvity, 6055302) were prepared, and approximately 60,000
1176 day 3 neurons were seeded per well in maturation medium containing BrainPhys (STEMCELL
1177 Technologies, 05790), B27 supplement (Gibco, 17504044), BDNF (PeproTech, 450-02), NT3
1178 (PeproTech, 450-03), and Laminin (Gibco, 23017-015). On the first maturation day, 40mM BrdU
1179 (Sigma, B9285) was added to the maturation medium. Neurons matured with half-medium
1180 replacements every 3 days. For staining mitochondria, cells were incubated with mitotracker
1181 (M22426, 1:20,000 dilution) for 30 min prior to fixation. For stress experiments, cells were incubated
1182 with sodium arsenite (500 µM, 30 minutes, Sigma Aldrich, S7400) or D-sorbitol (sorbitol, 0.4 M, 2 hr,
1183 Sigma Aldrich, S7547) prior to fixation. For the experiments of wild-type (KOLF) line without treatment
1184 or under oxidative stress, the cells were seeded in PLO-coated 384-well plates (Revvity, 6057300)
1185

1186 **Differentiation of iPSCs into day 60 spinal motor neurons**

1187 Sporadic ALS (sALS), *C9orf72*, and non-neurological control human subject iPSC lines were acquired
1188 from the Answer ALS repository at Cedars Sinai [172] (see Materials list). All iPSCs were maintained in 6
1189 well plates coated with growth factor reduced Matrigel (Corning) and mTeSR Plus Media (StemCell
1190 Technologies). iPSC lines were passaged at a ratio of 1:10 with ReLeSR (StemCell Technologies). As
1191 shown in Supplemental Figure 15, spinal motor neuron cultures were generated by differentiating
1192 iPSCs with a modified version of the direct induced motor neuron (diMNs) protocol that has been

1193 recently described [105,133]. Briefly, iPSCs were cultured and expanded for 3 weeks to facilitate
1194 acclimation and stabilization post-thaw. On day 0, iPSCs were dissociated with ReLeSR and plated in 6
1195 well plates (coated with growth factor reduced Matrigel) at a density of 500,000 cells/well in stage 1
1196 media (47.5% IMDM (Gibco), 47.5% F12 (Gibco), 1% NEAA (Gibco), 1% Pen/Strep (Gibco), 2% B27
1197 (Gibco), 1% N2 (Gibco), 0.2 mM LDN193189 (Stemgent), 10 mM SB431542 (StemCell Technologies),
1198 and 3 mM CHIR99021 (Sigma Aldrich)) supplemented with 20 mM ROCKi (Y-27632, Millipore). The
1199 next day, media was exchanged and replaced with stage 1 media without ROCKi. A full volume of stage
1200 1 media was subsequently exchanged on days 3 and 5 of differentiation. On day 6 of differentiation,
1201 cells were dissociated with accutase and plated in T25 flasks (coated with growth factor reduced
1202 Matrigel) at a density of $2x10^6$ cells/flask in stage 2 media (47.5% IMDM, 47.5% F12, 1% NEAA, 1%
1203 Pen/Strep, 2% B27, 1% N2, 0.2 mM LDN193189, 10 mM SB431542, 3 mM CHIR99021, 0.1 mM all-trans
1204 RA (Sigma Aldrich), and 1 mM SAG (Cayman Chemicals)) supplemented with 20 mM ROCKi. The next
1205 day, media was exchanged and replaced with stage 2 media without ROCKi. A full volume of stage 2
1206 media was subsequently exchanged on days 9 and 11 of differentiation. On day 12 of differentiation,
1207 cells were dissociated with Trypsin and plated in 6 well plates (coated with growth factor reduced
1208 Matrigel) at a density of $5x10^6$ cells/well in stage 3 media (47.5% IMDM, 47.5% F12, 1% NEAA, 1%
1209 Pen/Strep, 2% B27, 1% N2, 0.1 mM Compound E (Millipore), 2.5 mM DAPT (Sigma Aldrich), 0.1 mM
1210 db-cAMP (Millipore), 0.5 mM all-trans RA, 0.1 mM SAG, 200 ng/mL Ascorbic Acid (Sigma Aldrich), 10
1211 ng/mL BDNF (PeproTech), and 10 ng/mL GDNF (PeproTech) supplemented with 20 mM ROCKi. The
1212 next day, media was exchanged and replaced with stage 3 media without ROCKi. A full volume of stage
1213 3 media was exchanged on day 16 of differentiation. On day 18 of differentiation, iPSNs were
1214 dissociated with accutase and plated in 6 well plates (coated with growth factor reduced Matrigel) at
1215 a density of $5x10^6$ cells/well in stage 3 media supplemented with 20 mM ROCKi. The next day, media
1216 was exchanged and replaced with stage 3 media supplemented with 20 mM AraC. The next day, media
1217 was exchanged and replaced with stage 3 media without AraC. A full volume of stage 3 media was
1218 subsequently exchanged every 3-4 days until day 32 of differentiation. Beginning on day 32 of
1219 differentiation, a half volume of stage 3 media was manually exchanged with a P1000 pipette every 3-
1220 4 days until day 53 of differentiation. On day 53 of differentiation, iPSNs were dissociated with
1221 accutase and plated in glass bottom 24 well plates (coated with growth factor reduced Matrigel) at a
1222 density of 350,000 cells per well in stage 3 media supplemented with 20 mM ROCKi. The next day,
1223 media was exchanged and replaced with stage 3 media without ROCKi. A half volume of stage 3 media
1224 was subsequently exchanged on day 57 of differentiation. All iPSC lines used in this study were
1225 differentiated in a single experimental repeat. All iPSCs and iPSNs were maintained at 37°C with 5%
1226 CO_2 and routinely tested negative for mycoplasma.

1227 **Immunofluorescence**

1228 Cells in 96-well or 384-well plates were treated with 4% PFA in 1X PBS++ for a fixed duration of 15
1229 minutes. Post-fixation, cells were rinsed with PBS and were then exposed to 0.1% TritonX in PBS for a
1230 permeabilization step for 10-15 minutes. Blocking was achieved by incubating the cells with CasBlock
1231 (Thermo Fisher, 008120) reagent for 10 minutes at RT. Primary antibodies (listed in Materials) in
1232 CasBlock were prepared, and cells were submerged in 35-70 µl of this mix overnight at 4°C. In the case
1233 of the oxidative stress experiment, antibodies were diluted in permeabilization/blocking buffer (DPBS
1234 supplemented with 0.2% Saponin + 1.5% BSA) and incubated overnight at 4°C. The following day, cells
1235 were washed twice in 100 µl PBS for 5 minutes. Secondary antibodies (listed in Materials), diluted in

1236 PBS, were added to the cells, ensuring a 35-70 µl coverage for an hour while minimizing light exposure.
1237 Hoechst, diluted in PBS at a 1:8000 ratio, served as a DNA stain, and cells were treated with 75-100 µl
1238 of this mix for 10-30 minutes at room temperature. Before proceeding with imaging, the Hoechst
1239 solution was replaced with PBS. It was crucial to ensure the cells remained submerged in PBS,
1240 particularly during extended imaging sequences to prevent desiccation.

1241 For day 60 motor neurons, iPSNs were fixed and immunostained on day 60, as previously described
1242 [173,174]. Briefly, iPSNs were fixed in 4% PFA for 15 mins and washed 3X 5 mins with 1X PBS prior to
1243 permeabilization with 0.1% Triton X-100 in PBS for 15 mins. iPSNs were then incubated in 10% goat
1244 serum/1X PBS blocking solution for 30 mins. Primary antibodies were diluted in blocking solution and
1245 iPSNs were incubated with the resulting primary antibody solution for 2 hours at room temperature.
1246 iPSNs were then washed 3X 10 mins with 1X PBS and incubated with secondary antibody solution
1247 (1:1000 Goat Anti-Rabbit Alexa Fluor 488, 1:1000 Goat Anti-Guinea Pig Alexa Fluor 568, 1:1000 Goat
1248 Anti-Mouse Alexa Fluor 647; Thermo Fisher) diluted in blocking solution for 1 hour at room
1249 temperature. iPSNs were washed 3X 10 mins with 1X PBS, incubated with 1:1000 Hoechst/1X PBS
1250 solution for 5 mins at room temperature, and washed 2X 5 mins with 1X PBS prior to mounting with
1251 Prolong Gold and sealing of wells with a 15 mm glass coverslip. Agitation was not used at any step in
1252 the immunostaining protocol.

1253 **Definitions and experimental design of imaging studies**

1254 **Experimental repeat** - an experiment with an independent differentiation, or cells derived from
1255 different human subjects, according to the MDAR (Materials Design Analysis Reporting) framework
1256 guidelines (https://osf.io/xfpn4)[134].

1257 **Technical repeat** - multiple wells within the same experimental repeat.

1258 For our AI-based imaging studies, we generated several datasets of iPSC-derived neurons under
1259 different conditions (**Table 2**). For each dataset, we created two or more experimental repeats that
1260 arose from separate differentiations. Each of those experimental repeats encompasses two or more
1261 technical repeats, with cells from the same differentiation plated into a different well. An experimental
1262 repeat was imaged uninterruptedly. Human subject lines defined as experimental repeats, were
1263 generated in 2 separate experimental repeats (differentiations).

1264 **Table 2: Detailed experimental datasets of iPSC-derived neurons for organellomics studies**

1265 The table below depicts the overview of experimental setups generated across this study.

Cell lines	**Conditions**	**N experimental repeats (technical repeats per experimental repeat) used for inference**
Wild-type (KOLF)	+/- Sodium arsenite (SA)	3 (8)
TDP-43$^{\Delta NLS}$	+/- Doxycycline (DOX)	5 (3)

Wild-type (KOLF), *FUS* R495* homozygous, *FUS* R495* heterozygous, *FUS* R495* revertant, *TARDBP* M337V, *OPTN* Q398E, *TBK1* E696K	Untreated, day 8	6 (2)
Subject lines, control	Untreated, day 60	6 subjects were used in Data Fig. 5A-D, 3 subjects in Fig. 5E-L
Subject lines, *C9orf72*	Untreated, day 60	3 subjects Fig. 5A-D, , 3 subjects in Fig. 5E-L
Subject lines, sALS+	Untreated, day 60	10 subjects Fig. 5A-D, , 3 subjects in Fig. 5E-L
Subject lines, sALS-	Untreated, day 60	2 subjects Fig. 5A-D, 3 subjects in Fig. 5E-L

Microscopy

The iPSC-derived neurons (iNDI lines, day 8) that were used for training, were assessed using the Visitron Systems laser and laser control, complemented by the spinning disk confocal scanner unit from Yokogawa. The Olympus IX83 served as the primary microscope in this configuration, images were acquired at X60 using oil immersion. We used a filter wheel system featuring EF460/50m, E525/50m, FF01-609/54, and ET700/75m filters, along with the DM405/488/561/640 dichroic mirror. To optimize image acquisition, we employed specific parameters, including binning at 2 for pixel averaging and heightened sensitivity, an exposure time of 300ms, and dynamic adjustments to laser power (range: 0.1-100%) for optimal imaging of distinct fluorophores. Our high-throughput imaging strategy encompassed the capture of 10x10 images per well within a 96-well plate, resulting in a total of 100 images per well, without overlap between adjacent images. This systematic approach was applied to all cell lines in a consecutive run. Each image has 2-4 channels of a panel of 2-4 antibodies. The entire process was controlled through VisiView Software, ensuring seamless microscope control and efficient image acquisition.

The inference dataset of 8-day-old iPSC-derived neurons with or without oxidative stress was collected through automated imaging in the Nikon Bio-Pipeline equipped with a Ti2 Spinning Disk confocal microscope using a X60 water immersion lens. All other inference datasets of 8-day-old iPSC-derived neurons (iNDI collection; ALS lines or wild-type with or without osmotic stress, and the TDP-43$^{\Delta NLS}$ line) were assessed using the Opera Phenix Plus HCS system REVVITY, HH14001000). Images were acquired at X63 using automatic water immersion using two cameras, four channels (splitted between the cameras). Here, we also employed specific parameters, including binning at 2 for pixel averaging and heightened sensitivity. However, the laser power (Intensity) and time exposure (ms) parameters were set for each channel and marker specifically. All images were taken with 4-6 Z-stacks and max projected together with help from REVVITY's expert.

Day 60 motor neurons were imaged with a X63 objective with X1 digital zoom on a Zeiss LSM980 confocal in 24 well plates. Identical imaging parameters (e.g. laser power, gain) were used to acquire images. Ten images per well, 4 antibodies (see above), without overlap between adjacent images were taken.

1294 **Western blot**

1295 For western blot analysis of TDP-43 protein levels in wild-type and TDP-43$^{\Delta NLS}$-V5-APEX-expressing
1296 neurons, iPSC-derived neurons were grown to day 8 and construct expression was induced as
1297 described above. Protein content was harvested by scraping cells directly in RIPA lysis buffer
1298 supplemented with Complete Protease Inhibitor Cocktail (Roche, 4693116001) and PhosphoSTOP
1299 (Roche, 4906837001) and centrifugation of lysates at 15,000 × g for 10 min at 4°C. Protein
1300 concentration was then quantified with Bio-Rad Protein Assay Dye Reagent (Bio-Rad, 500-0006). 30
1301 ug of protein per well was loaded and gel electrophoresis was performed in 10% SDS-PAGE at 100 V
1302 for ~70 min. Next, proteins were transferred to nitrocellulose membranes (Whatman; 10401383) at
1303 250 mA for 70 min followed by membrane blocking with 3% bovine albumin fraction V (MPBio;
1304 160069) in PBS supplemented with 0.05% Tween-20 (PBST) for 1 h at R.T. Membranes were then
1305 incubated at 4°C overnight on a shaker with rabbit anti-TDP-43 antibody (1:5000, Proteintech, 10782-
1306 2-AP) and mouse anti-Tubulin (1:4000; Sigma-Aldrich, T9026) in antibody solution (5% albumin, 0.02%
1307 sodium azide and five drops of phenol red in 0.05% PBST). The following day, membranes were washed
1308 with 0.05% PBST three times for 5 min before proceeding to incubation with horseradish peroxidase-
1309 conjugated secondary antibodies (anti-rabbit, Jackson ImmunoResearch, 711-035-152; anti-mouse,
1310 Jackson ImmunoResearch, 715-035-150). Membranes were then washed with 0.05% PBST three times
1311 for 5 min and imaged using the Westar NOVA 2.0 Chemiluminescence kit (Cyanagen, XLS071) and
1312 ImageQuant LAS 4000 (GE Healthcare Life Sciences). Band intensities were quantified using ImageJ
1313 software and averaged across three experimental repeats for plotting.

1314

1315 **Fluorescence recovery after photobleaching (FRAP)**

1316 U2OS cells overexpressing DCP1A-YFP (yellow fluorescent protein, a gift from Dr. Nancy Kadersha and
1317 Prof. Paul Tylor) were maintained as described above (section of: U2OS cells). For FRAP of P-bodies
1318 under uninduced or induced cytoplasmic TDP-43 or Nuclear export signal (NES) expression, ~250K
1319 U2OS cells were seeded in individual 6-wells with coverslips. Next, the cells were co-transfected with
1320 two different plasmids: piggyBac transposase plasmid and PG-TO-hNGN2 that carries doxycycline-
1321 inducible NES-V5-APEX (as negative control) or TDP-43$^{\Delta NLS}$-V5-APEX (see above, expresses BFP; Blue
1322 Fluorescent Protein) in the place of NGN2, using Transfex reagent (ATCC, ACS-4005). The inducible
1323 expression constructs were integrated into the genome via the piggyBac transposon system. Twenty-
1324 four hours post-transfection, the cells were incubated overnight with doxycycline (DOX; 1ug/ml) for
1325 NES or cytoplasmic TDP-43 induction or only with media (as control; -DOX; uninduced) and with
1326 sodium arsenite (250 uM, Sigma, S7400) 60 min before the FRAP measurement. After 60 min, FRAP
1327 image sequences were obtained during 30 min on a Zeiss LSM 900 inverted scanning confocal
1328 microscope equipped with a heated chamber and a Plan-Apochromat 40× water objective (Carl Zeiss,
1329 Jena, Germany). First, we looked for cells expressing BFP to verify the successful uptake of the
1330 inducible constructs (NES- or TDP-43$^{\Delta NLS}$-V5-APEX. Those cells were scanned using a 488 laser for the
1331 detection of YFP-labeled P-bodies. For analysis of the fluorescence recovery, an internal area within a
1332 few P-bodies in a field of view was bleached and the fluorescence recovery was measured every ~1
1333 sec for 2 min. A single P-body and background area without bleaching were also measured per field of
1334 view (a site in a well). In each experiment, for each condition (uninduced or induced), 3-5 sites were
1335 analyzed in each of four 6-wells (technical repeats). In each site, between two to nine P-bodies were

1336 measured and the intensities for each time point were averaged. FRAP data were normalized and
1337 calculated by subtracting the background signal and then normalized to the P-body that was not
1338 bleached as reference. Measured P-bodies that were out-of-focus or exhibiting technical problems
1339 (e.g. unsuccessful bleaching) were excluded. The average of the normalized data for an experiment
1340 was synchronized by the average time point value. The final data points that are shown in the figures
1341 represent average of the 4 technical repeats as described above. For each experimental repeat, the
1342 statistical testing was two-way ANOVA with repeated measures and Geisser-Greenhouse correction,
1343 in Prism (version 10).

1344 **APEX proximity labeling**

1345 Monoclonal iPSC lines carrying TDP-43$^{\Delta NLS}$ and NES APEX constructs were differentiated into neurons
1346 as described previously. After 5 days of maturation, construct expression was induced for 24 and 4
1347 hours respectively to achieve comparable levels of expression. APEX activity was induced by
1348 supplementing biotin-phenol (BP, 500 µM, Iris Biotech GmbH, LS-3500) for 90 minutes and H2O2 (1
1349 mM, J.T.Baker 7722-84-1) for 1 min. Labeling activity was halted with quenching solution (QS: sodium
1350 azide (10mM, Mallinckrodt, 1953-57), sodium ascorbate (10mM, Sigma-Aldrich, A7631) and Trolox
1351 (5mM, Sigma-Aldrich, 238813) in PBS. Then, cells were scraped directly in RIPA lysis buffer
1352 supplemented with Complete Protease Inhibitor Cocktail (Roche, 4693116001) and PhosphoSTOP
1353 (Roche, 4906837001). Lysates were centrifuged at 15,000 × g for 10 min at 4°C after which protein
1354 concentration was quantified with Bio-Rad Protein Assay Dye Reagent (Bio-Rad, 500-0006).
1355 Streptavidin-coated magnetic beads (Pierce Streptavidin Magnetic Beads, Thermo-Fisher, 88816)
1356 were incubated at a ratio of 100 µl beads per 500 µg of sample with rotation overnight at 4°C. The
1357 next day, bead samples were washed with a series of buffers, 1 ml per wash, for 3 minutes at 1100
1358 rpm at room temp to remove non-specific binders: twice with RIPA lysis buffer, once with 1 M KCl
1359 (MERCK, 104936), once with 0.1 M Na2CO3 (Sigma-Aldrich, S7795), and once with 2 M Urea solution
1360 containing 10 mM Tris-HCl, pH 8.0 (Invitrogen, 15568–025).

1361 **Sample preparation for mass spectrometry**

1362 All chemicals are from Sigma-Aldrich Aldrich, unless stated otherwise. Samples were subjected to on-
1363 bead tryptic digestion followed by a desalting step. Briefly, washed beads after pull-down were
1364 suspended in 8M urea, 0.1M Tris HCl buffer, pH 7.6, and incubated at room temp for 30 min. Proteins
1365 were then reduced with 100 mM DTT (5mM final conc) at room temp for 1 hr and then alkylated using
1366 iodoacetamide (10 mM final concentration) for 45 min in the dark at room temp. Urea concentration
1367 was diluted 5-fold by addition of 50mM ammonium bicarbonate. 250 ng trypsin was then added and
1368 samples were incubated at 37°C overnight, followed by a second trypsin digestion (250 ng) for 4 hours
1369 at 37°C. Digested peptides were then collected by centrifugation of the beads and transferring the
1370 supernatant into a clean tube. Peptides were acidified with trifluoroacetic acid, desalted using HBL
1371 Oasis (Waters 094225), speed vac to dryness and stored in -80°C until analysis.
1372

1373 **Liquid chromatography and mass spectrometry**

1374 Digested proteins were loaded and analyzed using split-less nano-Ultra Performance Liquid
1375 Chromatography (10 kpsi nanoAcquity; Waters, Milford, MA, USA). The mobile phase was: A) H2O +

1376 0.1% formic acid and B) acetonitrile + 0.1% formic acid. Desalting of the samples was performed online
1377 using a Symmetry C18 reversed-phase trapping column (180 µm internal diameter, 20 mm length, 5
1378 µm particle size; Waters). The peptides were then separated using a T3 HSS nano-column (75 µm
1379 internal diameter, 250 mm length, 1.8 µm particle size; Waters) at 0.35 µL/min. Peptides were eluted
1380 from the column into the mass spectrometer using the following gradient: 4% to 26%B in 155 min,
1381 26% to 90%B in 5 min, maintained at 90%B for 5 min and then back to initial conditions. The nanoUPLC
1382 was coupled online through a nanoESI emitter (10 µm tip; New Objective; Woburn, MA, USA) to a
1383 quadrupole orbitrap mass spectrometer (Q Exactive Plus, Thermo Scientific) using a FlexIon nanospray
1384 apparatus (Proxeon).
1385
1386 For targeted MS, samples were analyzed by targeted analysis while monitoring relevant peptides. The
1387 targeted analysis data were analyzed using the Skyline algorithm and manually curated for confident
1388 identifications and accurate quantification. The data were also searched against the human protein
1389 database using the Proteome Discoverer software to increase confidence in the assignment of the
1390 relevant peaks.
1391
1392 For unbiased, proteome-wide MS, data was acquired in data dependent acquisition (DDA) mode, using
1393 a Top10 method. MS1 resolution was set to 70,000 (at 200m/z) and maximum injection time was set
1394 to 60 msec. MS2 resolution was set to 15,000 (at 200m/z) and maximum injection time of 60 msec.
1395

1396 **Raw proteomic data analysis of unbiased MS**

1397 Raw data was analyzed using MaxQuant (v1.6.6.0) [175]. The raw data was searched against the human
1398 protein database downloaded from UniprotKB appended with 125 common laboratory contaminant
1399 proteins. Enzyme specificity was set to trypsin and up to two missed cleavages were allowed. Fixed
1400 modification was set to carbamidomethylation of cysteines and variable modifications were set to
1401 oxidation of methionines, asparagine and glutamine deamidation, and protein N-terminal acetylation.
1402 Peptide precursor ions were searched with a maximum mass deviation of 4.5 ppm and fragment ions
1403 with a maximum mass deviation of 20 ppm. Peptide, protein and site identifications were filtered at
1404 an FDR of 1% using the decoy database strategy. The minimal peptide length was 7 amino-acids and
1405 the minimum Andromeda score for modified peptides was 40. Peptide identifications were
1406 propagated across samples using the match-between-runs option checked. Searches were performed
1407 with the label-free quantification option selected.

1408 **Proteomics statistical analysis**

1409 MaxQuant output table ProteinGroups was imported to Perseus [176] and analyzed as follows. Reverse
1410 proteins, proteins identified only based on a modified peptide and contaminants were excluded
1411 before log2-transforming the data. Rows were filtered to keep only those with at least 6 valid values,
1412 and missing values were replaced by low values from a normal distribution. Two-sample t-test
1413 comparing samples with biotin to samples without biotin was performed to remove non-specific
1414 binders (FDR < 0.05, log2FC > 0). Samples were separated based on stress condition before filtering to
1415 remain only those proteins with a minimum of 2 valid values in at least one experimental group (TDP-
1416 $43^{\Delta NLS}$ or NES). Missing values were imputed again using a normal distribution. Two-sample t-test using
1417 log2-transformed LFQ values was performed to gain proteins enriched in TDP-$43^{\Delta NLS}$.

1418 For targeted MS, peptide intensities were normalized against the Total Ion Current Area per peptide
1419 for each protein. These values were averaged to get a single value per protein. Then, data from both
1420 groups (TDP-43$^{\Delta NLS}$ and NES) were normalized to the average of the NES group per protein before
1421 comparing between conditions to get fold changes.
1422

1423 **Human post-mortem tissue staining and quantification**

1424 Motor cortical tissues from *C9orf72* or sALS cases and age-and sex-matched controls were from the
1425 Target ALS post-mortem core or from the Sheffield Brain bank under the following ethical approvals:
1426 SBTB REC number 08/MRE00/103+5, SBTB application no: 23/007. Cases were included in triplicate in
1427 a tissue microarray (TMA) format (TMA available through the Target ALS Post-mortem core). For P-
1428 body immunohistochemistry analysis, sections were cut at 4 µm thickness onto superfrost charged
1429 slides and deparaffinized. Sections then underwent heat mediated antigen retrieval in citric acid
1430 (pH=6) for 15 minutes in a pressure cooker. Following this antibodies were incubated for 90 minutes
1431 at the following concentrations: DCP1A 1:100 (Abcam ab47811), LSM14A 1:100 (Proteintech 18336-
1432 1-AP) and AGO2 1:200 (Abcam ab32381) for 1 hr at room temperature. Sections were stained using
1433 the Novolink Polymer detection system and 3,3'-Diaminobenzidine (DAB) chromogen was used and
1434 counterstaining was performed with haematoxylin, according to standard operating procedures. TDP-
1435 43 aptamer dual chromogenic stains were performed using our standard operating protocol freely
1436 available online [177] using the following concentrations: DCP1A 1:100, LSM14A 1:100, secondary anti-
1437 biotin Alkaline phosphatase antibody at 1:100 (30 minutes incubation). Digital analysis was performed
1438 using ImageJ analyze particle function. Images were batch processed as follows: Image>8-bit.
1439 Process>Sharpen. Image>Adjust>Brightness & Contrast>minimum = 53, maximum = 144. Set
1440 measurements> area and limit to threshold. Image>Adjust>Threshold>48-103. Analyze>Analyze
1441 Particles>Size=5-Infinity, Circularity = 0-1, Show = Bare Outlines, Display results, Add to Manager.

1442 **SLAM-seq and mRNA stability analysis**

1443 For metabolic RNA labeling of TDP-43$^{\Delta NLS}$-expressing iPSC-derived neurons, the maturation medium
1444 was replaced with a medium containing 4sU (200 µM, T4509, Sigma). Since multiple timepoints are
1445 recommended, and 3 hours of labeling was shown to be sufficient to reveal changes in RNA half-life
1446 [131], cells were incubated with 4sU for 0, 2 or 3 hours. After labeling, cells were harvested with Tri-
1447 reagent (Sigma) followed by RNA extraction under reducing conditions and treatment with
1448 iodoacetamide (A3221, Sigma) as previously described [130]. RNA-seq libraries were prepared at the
1449 Crown Genomics Institute of the Nancy and Stephen Grand Israel National Center for Personalized
1450 Medicine, Weizmann Institute of Science. A bulk adaptation of the MARS-Seq protocol [178,179] was used
1451 to generate RNA-Seq libraries for SLAM-seq. Briefly, 30 ng of input RNA from each sample was
1452 barcoded during reverse transcription and pooled. Following Agencourt Ampure XP beads cleanup
1453 (Beckman Coulter), the pooled samples underwent second-strand synthesis and were linearly
1454 amplified by T7 in vitro transcription. The resulting RNA was fragmented and converted into a
1455 sequencing-ready library by tagging the samples with Illumina sequences during ligation, RT, and PCR.
1456 Libraries were quantified by Qubit and TapeStation as well as by qPCR for Human GAPDH gene as
1457 previously described [178,179]. Sequencing was done on a Nextseq 500, using Nextseq High Output 75
1458 cycles kit mode, allocating 400M reads in total (Illumina). RNA-seq reads were aligned to the human

genome (version GRCh38.99) with STAR (version 2.7.3a) [180] using parameters "--outFilterMismatchNmax 20 --outFilterScoreMinOverLread 0.4 --outFilterMatchNminOverLread 0.4 --outSAMattributes nM MD NH --alignEndsType Extend5pOfRead1 --quantMode GeneCounts". Bam files from STAR were processed with GRAND-SLAM (version 2.0.7b) [131] with trimming of 20 nucleotides in the 5' end due to higher mismatch rates across all nucleotides in this region. The error rate correction linear model was set to AT instead of the default TA, because the latter showed a higher error rate and variability across samples. Unlabeled samples without 4sU were used for the model estimation. The main output table of GRAND-SLAM ({prefix}.tsv) was used as input for analysis with grandR (version 0.2.5) [132] for half-life estimations as previously explained [181]. We based analysis of P-body-enriched RNAs, on data from [116] (FDR < 0.05, log2FC > 1). Final statistical testing was done with Prism (version 10).

Computational methods

Preprocessing pipeline of microscopic images

Day 8 iPSC-derived neurons (used for model training): Immunofluorescence confocal images were taken using a Spinning disc confocal microscope. Each image (1,024x1,024 pixels, also referred as "site image") is dual-channel, holding the target marker as the first channel and the nucleus (Hoechst 33342) as the second. First, raw pixels were scaled to a range of 0 to 1 using the rescale_intensity function from skimage python package (V0.21.0), with the in_range parameter sets to 0.5 percentile and 99.9 percentile of the pixels' intensity distribution and out_range sets to numpy.float32. Corrupted/out-of-focus sites were filtered (see **Methods**). Site image was then cropped to 64 equal-sized tiles (128x128 pixels). Each tile was resized to 100x100 pixels (using the resize function from skimage package V0.19.3, with anti_aliasing=True). Tiles containing at least 80% of a single nucleus and not more than 5 nuclei were considered valid. See also **Supplementary Figure 2**.

Day 8 iPSC-derived neurons in inference (**Figures 1-4**): Immunofluorescence confocal images were taken using an Opera Phenix Plus microscope (Revvity, **Methods**). Site images of 1,080x1,080 pixels were cropped into 1024x1024 pixels by cropping 28 pixels from each edge. The same pipeline as described before was applied here. In addition, pixel intensity of each tile was scaled to a range of 0 to 1 with the rescale_intensity function using the same parameters as applied to the full site. Tiles containing dead cells or lacking detectable signal in any channel were excluded. Since images of neurons are highly sparse, all tiles were subjected to QC process, where we kept only valid tiles. See also **Supplementary Figure 2**.

Immunofluorescent confocal images of sALS patient-derived motor neurons (day 60) (1,024x1,024 pixels) were taken using Zeiss LSM 980 confocal microscope (Zeiss), with a larger zoom magnitude (X63) than the rest of the data (X60). Hence, each image was first cropped to 1022x1022 by removing one pixel from each side, then cropped into 49 equal-sized tiles (146x146 pixels), which were subsequently resized to 100x100 pixels as described before. Neither intensity rescaling nor filtering of unfocused images were needed. Tiles containing dead cells or lacking detectable signal in at least one channel were excluded.

A detailed summary of the datasets is provided in the **Supplementary Materials**.

1499 **Quality control**

1500 Site images (both the target organelle and the nucleus channels) that contained debris or were out of
1501 focus were filtered using Brenner's Gradient score [182] (applied on both horizontal and vertical
1502 dimensions), an approach for focus evaluation. Site images that passed filtering were then uniformly
1503 cropped to tiles of size 100x100. A tile considered valid if it contained 0.8 of the nuclei, and if both its
1504 maximum pixel intensity and variance exceeded predefined thresholds as follows.
1505
1506 To determine whether a tile contained at least 80% of a nucleus, we performed nuclei detection using
1507 Cellpose[183] (V2.0.3, parameters: model type='nuclei', diameter=60) on the nucleus channel convolved
1508 with [[-1,-1,-1], [-1,25,-1], [-1,-1,-1]] for edges enhancement. For each detected nucleus, a polygon
1509 was computed using the Python package Shapely (version 2.0.1). We then calculated the ratio
1510 between the area of the polygon within the tile and the total polygon area outside the tile. Tiles with
1511 a ratio greater than 0.8 were considered to contain a sufficiently complete nucleus. Nuclei intersecting
1512 the site boundaries, where the full nuclear size could not be determined and the 80% threshold could
1513 therefore not be tested, were excluded from the nuclei count. Intersection with the site boundaries
1514 was detected by computing a polygon for the entire site boundary, minus a padding of 1 unit on each
1515 side. If the nucleus polygon was not completely contained within the site's polygon, the nucleus was
1516 disqualified (**Supplementary Figure 2**). The neuron count in our data, therefore, reflects the number
1517 of nuclei for which at least 80% of the area was captured within valid tile.

1518 To detect tiles containing dead cells, we leveraged the observation that dead cells typically exhibit
1519 elevated nuclear pixel intensities and smaller nuclei than living cells. Accordingly, we evaluated the
1520 median intensity of each nucleus within the rescaled intensity tile. Instance segmentation of nuclei
1521 was performed in two steps: first, pixels belonging to nuclei were identified by applying Otsu
1522 thresholding (using the threshold_otsu function from scikit-image), and second, individual nuclei were
1523 delineated by detecting connected components (using the label function from scipy.ndimage,
1524 v1.12.0). This procedure yielded a mask for each nucleus, from which we computed the median pixel
1525 intensity. Nuclei with median intensity above 0.95 (on a scale where 1 represents the maximum
1526 possible intensity) were classified as dead cells, except for the sALS patient-derived motor neuron (Day
1527 60) full dataset, where a lower threshold of 0.8 was used. For the iPSC-derived neuron datasets, an
1528 additional size-based criterion was applied to improve dead-cell detection, since dead cells typically
1529 display smaller nuclei than living cells. For nuclei not touching the tile frame, the area was measured
1530 as the number of pixels within the nucleus mask. Nuclei with an area below 800 pixels were classified
1531 as dead.

1532 For detecting tiles lacking a detectable signal, we applied two criteria. First, we tested whether the
1533 maximum pixel intensity of the tile (prior to intensity rescaling) was below a predefined threshold (0.2
1534 for both channels) . Second, we evaluated whether the variance of the rescaled pixel intensities fell
1535 below a predefined threshold (0.0001 for the target channel, and 0.03 for the nucleus). Tiles meeting
1536 either condition were excluded.

1537 **Localization encoding ViT-based model**

1538 A ViT model with linear head and cross-entropy loss was trained from scratch on the publicly available
1539 OpenCell dataset (1,100,253 cropped images [48]). The data was split into 70%, 15%, 15% for training,

validation, and testing data, respectively. Model parameters: embed_dim=192, patch_size=14, in_chans=2, output_dim=1311. The input for the model are dual-channel tiles of 100x100 (a 3D vector sized (2,100,100)). Model training converged after 44 epochs (**Supplementary Figure 3A**). In training, the following augmentations were applied with a probability of 0.5 for each: horizontal flip, vertical flip, and rotation of 90, 180, or 270 degrees. Train parameters: we used the AdamW optimizer with adjustable weight_decay for non bias nor Norm parameters. A cosine scheduler was used for controlling the weight decay (base value=0.04, final value=0.4, number of epochs=300) and the learning rate (base value=0.0008*experimental repeat_size/256, final value= 0.000001, number of epochs=300, number of warmup epochs=5). Experimental repeat comprised of 350 site images, each containing 7 valid tiles on average. Early stopping was applied after ten epochs in which the validation loss showed no improvement. A grad scaler (torch.cuda.amp.GradScaler) was used for calculating the gradients. Unscaled gradients' norms were clipped (torch.nn.utils.clip_grad_norm_) with max_norm=3.

Perturbation learning ViT-based model using InfoNCE contrastive loss

For perturbation learning, we extended the pre-trained model as follows. We first initialized a ViT model with weights from the pre-trained model (that was trained for localization encoding). To better capture non-linear relationships in the data, the original linear ViT head was replaced with a multi-layer architecture (*Linear(192, 768) -> BatchNorm1(768) -> GELU -> Linear(768, 384) -> BatchNorm1d(384) -> GELU -> Linear(384, 128) -> LayerNorm(128))*. During fine-tuning, we partially froze selected layers (see **Methods**, **Supplementary Figure 4**) and the model was trained in a supervised contrastive framework using the infoNCE[4445] loss (**Figure 1B**, **Supplementary Figure 6**).

The contrastive learning task was implemented as following: for each anchor tile x during training (100x100 pixels, two channels), six additional images of the same organelle were randomly sampled: one positive (x^+) and five negatives (x^-). Positives corresponded to image tiles from the same organelle under the same perturbation, whereas negatives were tiles under different perturbations. Notably, sampling is done with replacement, and matches were allowed to originate from different experimental repeats. Pulling anchors and positives together across repeats reduced repeat-specific variations, thereby mitigating overfitting to technical artifacts and encouraging the model to learn repeat-invariant representations. Conversely, pushing anchors away from negatives refined representations towards true perturbation-specific effects.

The InfoNCE loss was calculated as follows:

$$L_{infoNCE} = -\mathbb{E}[log \frac{f(x,x^+)}{f(x,x^+)+\sum_{i=1}^{K} f(x,x^-{}_i)}],$$

$$where\ f(x,x') = exp\ (\frac{sim(x,x')}{\tau}), sim(x,x') = \frac{x \cdot x'}{||x|| \cdot ||x'||}, \tau = 0.1, K = 5$$

Since sampling was performed with replacement, each tile could also serve as an anchor, positive or negative across different matched triplets, enhancing generalization. This transitive structure of contrastive learning reinforces relationships across samples, reducing overfitting to specific image

pairs and improving robustness. By sharing anchors among multiple comparisons, the model learns a consistent representation space that better captures true perturbation effects.

Unlike standard supervised classification, this contrastive formulation models *weak supervision*: perturbation labels indicate potential, but not guaranteed, phenotypic effects. Because not all perturbations yield consistent organellar changes, relying solely on label differences could introduce spurious relationships. Incorporating negatives within the contrastive framework mitigates this risk by emphasizing reproducible, perturbation-specific signals over random or noise-driven variation.

Training followed the same procedure as the pre-trained model, with the exception of a reduced output dimension of 128 and an experimental repeat size of 750. The dataset used for training was composed of 3,213,360 dual-channel images of human iPSC-derived neurons spanning 25 organelles (Nucleus, ER, Nucleolus, TDP43 granules, Paraspeckles, ANXA11 granules, Golgi, Lysosome, FUS granules, Peroxisome, P-bodies, Integrin puncta, Autophagosomes, PML bodies, Presynapse, NEMO granules, Postsynapse, Transport machinery, Coated vesicles, MOM, Mitochondria, PURA granules, Stress granules, Actin Cytoskeleton, FMRP granules) across 9 different cell lines/conditions (WT, WT treated with stress, FUS heterozygous, FUS homozygous, FUS revertant, TBK1, OPTN, TDP43 and SNCA). The data was generated from two independent biological differentiations (referred to as "experimental repeats"), with each differentiation including two to eight technical repeats per condition. It was split into train (70%), validation (15%), and test (15%) sets. The model converged after 19 epochs (**Supplementary Figure 5**). All reported results were obtained on held-out datasets and were not used during model development.

Partial fine-tuning: the angle-metric approach for freezing layers in perturbation learning

Fine-tuning is the adaptation of a pre-trained model, initially trained on massive amounts of labeled data, to perform well on a different but related problem. This involves selectively updating the model's parameters to capture the nuances of the new task. [184]. The "localization encoding model" is extended to perform "perturbation learning" in neurons (**Figure 1B**) using partial fine-tuning (**Supplementary Figure 4**). All weights of the transformer encoder are copied to the new model, except for the head, but not all model layers were re-trained with data of neurons. The training process is done by utilizing a data-drive approach for selecting which layers to freeze and which to fine-tune with our perturbed neurons. Frozen layers are not being updated during the fine-tuning process. For selecting which layers to freeze we first trained a perturbation learning model (see **Methods**) without freezing any layer. Then, we calculated for each layer how much it deviated from the pre-trained model weights using the angle metric [49]:

$$\theta(L) = arccos\left(\frac{W^L{}_p * W^L{}_t}{||W^L{}_p||_2 \, ||w^L{}_t||_2}\right)$$

where $W^L{}_p$ are the weights of layer L in the pre-trained model, and $W^L{}_t$ are the weights of the same layer L in the model after no-freezing fine-tuning.

Finally, since the tasks are different, yet share basic commonalities, we picked the least deviated layers (50% of the layers) to be the ones we freeze.

Image encoding

While our training pipeline runs the training consecutively (the localization encoding model and then the perturbation learning model), the inference step is done only with the perturbation learning model. During inference, a 100x100 pixels image (target and nucleus channel) is fed into the model to generate a 192-dimensional numerical representation from the second-to-last layer, normalized with L2 norm.

Combined effect size via random-effects meta-analysis

To quantify the effect of a perturbation on an organelle topography (relative to a baseline), we define a distance-based "effect size" metric on NOVA-derived embeddings (full latent space). This measure captures the degree to which a perturbation shifts organelle topography away from a baseline state, while accounting for natural variability within the baseline population.

Since we seek for perturbational changes that are consistent across experimental repeats (i.e., biological differentiations or human subjects within the same gene group, etc.), our meta-analytic approach considers each experimental repeat as a "study" with effect size, and performs a meta-analysis with mixed-effects for each organelle–perturbation pair. This results in an estimate of "combined effect size" across experimental repeats, while modeling both the sampling variance within each repeat and the heterogeneity across repeats.

Let K be the number of experimental repeats. For each combination of (perturbation × organelle × experimental repeat), we compute the observed effect size and variance for experimental repeat (steps 1-4), that are subsequently aggregated across experimental repeats using mixed-effects meta-analysis to yield a final combined effect estimate (step 5).

Denote,

$\mathcal{X}_b = \{x_1^b, \ldots, x_{n_b}^b\} \subset \mathbb{R}^{192}$: embeddings of baseline (WT) samples

$\mathcal{X}_p = \left\{x_1^p, \ldots, x_{n_p}^p\right\} \subset \mathbb{R}^{192}$: embeddings of perturbed samples

$d(\cdot,\cdot)$: a distance function, assumed to be Euclidian

n_b, n_p: number of baseline and perturbation samples, respectively

$\forall k \in 1, .., K$ We compute the per-experimental repeat estimates, namely effect size $\widehat{\theta_k}$ and $Var(\hat{\theta}_k)$ as follows:

Step 1: Baseline median

Let $\widetilde{x_b} \in \mathbb{R}^{192}$ be the median of the baseline group in the latent space.

Step 2: Within-group dispersion

Median distance of baseline samples to baseline median:

$$\widetilde{d_b} = median\{d(x_i^b, \widetilde{x_b})\}$$

Step 3: Between-group dispersion

Median distance of perturbed samples to baseline median:

$$\widetilde{d_p} = median\{d(x_j^p, \widetilde{x_b})\}$$

Step 4: Effect size and bootstrapped sampling variance per experimental repeat

Effect size $\hat{\theta}$ is defined as the "relative distance shifts" (how much a perturbation shifts a distribution in embedding space), and computed as the log fold change between the "between-group dispersion" and "within-group dispersion":

$$\text{Effect size } \hat{\theta} = log_2 FC = log_2 \left(\frac{\widetilde{d_p}}{\widetilde{d_b}}\right)$$

Estimate the empirical variance $Var(\hat{\theta})$: assess the sampling uncertainty of the effect size across samples by bootstrapping: (i) Resample (with replacement) tiles from different sites from 80% of the perturbation and baseline samples. (ii) Recompute the effect size $\hat{\theta}$ for each bootstrap resample. (iii) Repeat B times, and trim extreme outliers (iv) Estimate variance ($Var(\hat{\theta})$) from the bootstrap distribution.

Step 5: Random-effects meta-analysis

Given the per-repeat estimates from steps 1-4 above (experimental repeat effect sizes $\hat{\theta}_1, .., \hat{\theta}_K$ and $Var(\hat{\theta}_1), .., Var(\hat{\theta}_K)$), the combined (pooled) effect size $\hat{\mu}$ and heterogeneity measures τ^2 (namely "between-studies variance"), Q and I^2, are computed as follows:

Fixed-effects weights:

$$\omega_k = \frac{1}{Var(\hat{\theta}_k)}$$

Q statistics (heterogeneity):

$$Q = \sum_{k=1}^{K} \omega_k \left(\hat{\theta}_k - \bar{\hat{\theta}}\right)^2, \quad \bar{\hat{\theta}} = \frac{\sum_{k=1}^{K} \omega_k \hat{\theta}_k}{\sum_{k=1}^{K} \omega_k}, (df = k - 1)$$

Estimate between-experimental repeat variance τ^2 :

$$\tau^2 = max \left\{ 0, \frac{Q-(k-1)}{\sum_{k=1}^{K} \omega_k - \frac{\sum_{k=1}^{K} {\omega_k}^2}{\sum_{k=1}^{K} \omega_k}} \right\}$$

Random-effects weights: each experimental repeat is weighted by the inverse of its total variance

$${\omega^*}_k = \frac{1}{Var(\hat{\theta}_k) + \tau^2}$$

Combined (pooled) effect size:

$$\hat{\mu} = \frac{\sum_k {\omega^*}_k \hat{\theta}_k}{\sum_k {\omega^*}_k}$$

The I^2 statistic, a measure of heterogeneity across repeats:

$$I^2 = max\ (0, \frac{Q - df}{Q}) * 100\%, (df = k - 1)$$

I^2 ranges from 0% (no observed heterogeneity) to 100% (all variation due to heterogeneity). Values above 75% are typically interperted as indicating considerable heterogeneity.

Notably, when estimated heterogeneity (τ^2) was zero, the combined effect size and CI coincides with the fixed-effect model.

Step 6 (optional): confidence interval for τ^2

Confidence intervals were calculated using a profile likelihood approach. Log-likelihood was defined as follow:

$$l(\tau^2) = -\frac{1}{2}\left[\sum_{i=1}^{k} ln\,(Var(\widehat{\theta_i}) + \tau^2)\ + ln\,(\sum_{i=1}^{k} \omega_i^*) + \sum_{i=1}^{k} \omega_i^*(\widehat{\theta_i} - \hat{\mu})\right]$$

If $\tau^2 = 0$, the lower bound was set to 0. Otherwise the lower bound was obtained by solving for the value of $\widehat{\tau^2}$ between 0 and τ^2 where the $2 * l(\tau^2) - l(\widehat{\tau^2})$ equalled the chi-square cutoff ($\chi^2_{1,0.95}$). For the upper bound, the search range was iteratively expanded from τ^2 until the log-likelihood dropped below the chi-square threshold, after which the precise upper bound was located by root-finding within this interval, also using optimize.brentq.

Effect sizes were tested for significance using z-scores, calculated as the ratio between the combined effect estimate and its standard error. One-tailed p-values were obtained under the null hypothesis of $ratio <= 0$, ($\alpha = 0.05$) . To control for multiple testing across organelles, p-values were corrected using the Benjamini–Hochberg procedure (FDR).

Inclusion of an experimental repeat in the meta-analysis required meeting a predefined minimum sample size (see **Supplementary Materials** for the threshold for each dataset).

Combined effect size and its confidence intervals were calculated using the combine_effects function from the statsmodels python package (v0.14.2). Confidence interval for τ^2 (profile likelihood approach) were computed using optimize.brentq function from the scipy (v1.12.0) python package.

Organelle scoring forest plot

For each organelle × perturbation pair, the organellome was ranked based on the combined effect size $\hat{\mu}$. The ranking is visualized with a stacked forest plot with multiple organelle × perturbation pairs, presenting as a group both experimental repeat-level effects and the combined (pooled) inference for every organelle. Each repeat is represented by a dot (experimental repeat-wise effect estimate) and a light-colored horizontal line (error bar width indicating within-experimental repeat CIs). The experimental repeat-level (within-study) CIs are computed using experimental repeat-level variance and effect (effect ± 1.96·SE, Wald intervals). The black diamond in each group represents the combined effect estimate across experimental repeats ($\hat{\mu}$), shown with its 95% meta-analytic CIs (black horizontal line), which accounts for between-experimental repeat variance (τ^2) when present. For perturbations where $\tau^2 = 0$, the combined effect and CI corresponds to a fixed-effect model.

1716 **Pixel-level colocalization analysis of TDP-43 and P-body**

1717 To assess spatial colocalization between TDP-43 and P-body, we implemented a pixel-wise overlap
1718 analysis using multiplexed site images co-stained for TDP-43 (V5 tag) and P-body marker (DCP1A) in 8
1719 day iPSC-derived neurons expressing TDP-43$^{\Delta NLS}$. Site images (1024×1024) were acquired from three
1720 experimental repeats, each containing four technical repeats and ~200 sites (fields of view) per
1721 condition. Pixel-level colocalization was quantified using a conditional probability approach: for each
1722 image, the fraction of DCP1A-positive pixels that were also positive for TDP-43 was calculated, yielding
1723 the colocalization score:

1724 $$Fraction\ Overlap = P(TDP\text{-}43^{+}|DCP1A^{+}) = \frac{\#\ (TDP\text{-}43-positive\ pixels) \cap \#\ (DCP1A-positive\ pixels)}{\#\ (DCP1A-positive\ pixels)}$$

1725 To define "positive" signal pixels, binary masks for each marker were generated by applying per-image
1726 intensity thresholds. For TDP-43, the threshold was defined as the mean pixel intensity plus two
1727 standard deviations (mean+2×SD), and for DCP1A, the threshold was mean+2.5×SD. Only pixels
1728 exceeding these thresholds were considered "positive."
1729

1730 To determine whether observed colocalization exceeded what would be expected by random spatial
1731 proximity, we implemented a rotation-based null model. For each image, the TDP-43 channel was
1732 rotated 90° counterclockwise and re-aligned to the original DCP1A channel. This procedure preserved
1733 pixel intensities and marginal marker distributions, while disrupting spatial alignment. Real and
1734 rotated scores were computed for each image, yielding one colocalization value and one null control
1735 per image. A paired Wilcoxon signed-rank test was used to test whether real colocalization was
1736 significantly greater than rotated (null) colocalization.

1737 A similar analysis was performed on site images (2275x2284) of 60 day iPSC-derived neurons from
1738 subjects (healthy controls or ALS patients) stained for TDP-43 (TDP-43 antibody) and P-body marker
1739 (DCP1A) using thresholds of mean+0.5×SD for TDP-43 and mean+3×SD for DCP1A. To estimate the
1740 level of colocalization in each human subject group, we applied a linear fixed-effects model with
1741 human subject-clustered standard errors (fallback used).

1742 All analyses were performed using Python, with custom utilities implemented in the
1743 tools.channels_colocalization.pixel_colocalization_utils module. Visualization and statistical tests
1744 were conducted using matplotlib, seaborn, and scipy.stats.

1745

1746 **Post-hoc classifier for neuronal organelle identification: Model training and accuracy**

1747 To evaluate model performance, classification was performed on the wild-type group of the day 8
1748 iPSC-derived neurons across 26 organelles spanning three experimental repeats. A three-fold cross-
1749 validation scheme was used, where in each fold one experimental repeat was used for training and
1750 the remaining two for testing. The classifier was a linear support vector machine (LinearSVC, C=1.0,
1751 max_iter=1000, random_state=42) obtained from the *scikit-learn* python package (v1.3.0).

For each fold, accuracy, sensitivity, and specificity were computed per class. Macro-level statistics were obtained by averaging the per-class metrics within each fold, and the overall performance was calculated as the mean of the fold-level macro statistics.

ROC curves were computed in a one-vs.-rest manner for each class in every fold using the classifier decision scores. To obtain curves across folds, decision scores from all folds were concatenated and the ROC curves were recalculated from these combined arrays.

Confusion matrices were generated for each fold and then aggregated across folds. For visualization, the aggregated confusion matrix was row-wise normalized.

Rollout attention maps

For visualization of attention maps, self-attention tensors were extracted from each attention layer of the ViT model for every image, resulting in a tensor of shape $(12,3,50,50)$, corresponding to 12 attention layers, 3 attention heads per layer and $50x50$ patch-to-patch attention maps. Each tensor was reduced to shape $(12,50,50)$ by averaging over the attention heads.

The attention mechanism is defined as:

$$\textit{self_attention}(\boldsymbol{Q},\boldsymbol{K},\boldsymbol{V}) = \boldsymbol{softmax}(\frac{\boldsymbol{QK^T}}{\sqrt{\boldsymbol{d}}})\boldsymbol{V},$$

where $Q, K, V \in R^{n\times d}$ are the query, key, and value tensors for n patches with embedding dimension d, obtained from the output of the previous layer of the model. The softmax term produces an attention weight matrix $A \in R^{n\times n}$, with entries a_{ij} representing the contribution of patch j to i.

To capture the aggregated contribution of all layers, we applied an attention rollout [185]. Rollout propagates attention across all layers by recursively multiplying the attention matrices:

$$\widetilde{A^{(l)}} = IA^{(0)}A^{(1)}\ldots A^{(l-1)}A^{(l)},$$

where $A^{(l)}$ is the attention tensor at layer l, and $\widetilde{A^{(l)}}$ represents the cumulative attention up to layer l. This yields a final rollout attention tensor of shape $(50,50)$.

From the resulting tensor, we extracted the values corresponding to the CLS token (the first patch) as its attention distribution over the remaining 49 patches. The resulting values were min-max scaled to the range $[0,1]$.

Then, to match the resolution of the input image, the attention tensor was multiplied by 255 and cast to uint8 to enable resizing with the PIL library. We applied bicubic interpolation to resize the attention tensor to $(100,100)$, matching the image dimensions. Finally, we divided it by 255 to restore the $[0,1]$ range, yielding a resized attention tensor that highlights regions of high model focus with larger values and low model focus with lower values. For visualization purposes, we applied a threshold to display only values exceeding 0.5.

1784 **UMAP, dimensionality reduction of latent space and 2D clustering**

1785 To cluster images of organelles from different experimental perturbations, the image representations
1786 are subjected to dimensionality reduction using the Uniform Manifold Approximation and Projection
1787 (UMAP) algorithm (umap-learn v0.5.3, random_state=1). The first 2 UMAP components were plotted
1788 in a scatter plot to visualize clusters and colored according to their experimental perturbation. Our
1789 work presents different types of UMAPs based on the model output: single organelle plots (**Figure 2C**,
1790 **Figure 4D,E**, **Figure 5C,D,G,H**, **Supplementary Figure 12B**, **Supplementary Figure 14B**, **Supplementary**
1791 **Figure 15B**, **Supplementary Figure 22C,D**, **Supplementary Figure 24D**), and multiple organelles plots
1792 (**Figure 1C**, **Supplementary Figure 3D**, **Supplementary Figure 8**)

1793 **Distances between organelles or human subjects**

1794 To quantify the relationships between groups of embeddings shown in a UMAP (organelles / human
1795 subjects), pairwise Euclidean distances *d* were computed in the full latent space using 192-dimensional
1796 embeddings per image. The median of these pairwise distances was used as a robust summary statistic
1797 reflecting their similarity in the embedding space. For visualization, distances were shown in a
1798 heatmap after min–max normalized to the range [0, 1], where 0 indicates the closest and 1 the furthest
1799 relationship.

1800 **Unbiased CellProfiler analysis**

1801 For benchmarking organellome-wide analysis, CellProfiler (version 4.2.1; jdk version 14.0.1; python
1802 version 3.8) [47] objects were identified in images in three different size ranges to cover all possible
1803 organellar stainings; in addition, 'secondary object' identification was used for more diffuse cellular
1804 stains. Entire site images (1,024x1,024) were used as input images. All main object-related CellProfiler
1805 features relating to area, intensity, distribution, neighbors and texture were then extracted. Object
1806 measurements were averaged per image and concatenated across object types (using pandas, version
1807 1.4.4). After removing constant features and features containing missing values, the remaining 347
1808 features calculated with Cellprofiler as described above were used as features for classification and
1809 UMAP plotting as described above.

1810 **CellProfiler quantification of P-body size**

1811 A CellProfiler pipeline for calculating P-body size was applied. The pipeline identified P-bodies in the
1812 correct size range and extracted object features with 'MeasureObjectSizeShape'. Object-level
1813 measurements were extracted and averaged per site image. Effect size and statistical significance was
1814 calculated with linear mixed-effects models. Linear fixed-effects fallback used when variance was zero.
1815 In the case of TDP-43$^{\Delta NLS}$, DOX was set as a fixed effect and experimental repeat as a random intercept.
1816 In the case of day 60 human subject-derived neurons, effect was estimated per group (C9ALS, sALS+,
1817 etc.) while accounting for within-human subject dependences, by modeling the group variable as a
1818 fixed effect with human subject-clustered SEs (to handle collinearity of subject ID with group).

1819 **CellProfiler quantification of cytoplasmic/nuclear TDP-43 ratio**

1820 A CellProfiler pipeline was applied to quantify the cytoplasmic TDP-43 signal relative to the nuclear
1821 TDP-43 signal. First, nuclei were identified with 'IdentifyPrimaryObjects'. Using nuclei as input objects,

1822 the cytoplasm was then identified with 'IdentifySecondaryObjects' using the MAP2 channel and the
1823 'Propagation' method in case of day 60 human subject-derived neurons. For TDP-43$^{\Delta NLS}$ neurons, the
1824 TDP-43 channel and the 'Distance -N' method were used as input for secondary object identification.
1825 Since TDP-43 is also present in the nucleus, a third step was applied to subtract the nucleus from the
1826 secondary object using 'IdentifyTertiaryObjects', resulting in the cytoplasm. Intensity of TDP-43
1827 staining was then measured in both nucleus and cytoplasm, and the final ratio of cytoplasmic/nuclear
1828 TDP-43 was calculated with the 'CalculateMath' module.

1829

1830 Effect size and statistical significance was calculated with linear mixed-effects models. Linear fixed-
1831 effects fallback used when variance was zero. In the case of TDP-43$^{\Delta NLS}$, DOX was set as a fixed effect
1832 and experimental repeat as a covariate. In the case of day 60 human subject-derived neurons, effect
1833 was estimated per group (C9ALS, sALS+, etc.) by linear mixed-effects models (modeling the human
1834 subject group as a fixed effect and human subject as random intercept).

1835 **Prediction of protein-protein interactions**

1836 SpeedPPI [186] was implemented to predict interaction strength between TDP-43 and P-body proteins.
1837 Briefly, the pipeline generates multiple sequence alignments (MSAs) for TDP-43 and its potential
1838 interactors using HHlibs. It offers multiple operational modes, including "all-vs-all" and "some-vs-
1839 some"; we utilized the "some-vs-some" mode to compare TDP-43 against a defined list of target
1840 proteins. The MSAs are then subjected to structure prediction and validation using AlphaFold2 [113],
1841 providing high-confidence structural models for each protein. These validated structures are fed into
1842 the SpeedPPI predictor, a machine learning-based model that integrates several features. The final
1843 output is a structural modeling prediction that illustrates the potential interaction interfaces between
1844 TDP-43 and its interactors. In addition, a pDockQ score, a probabilistic score ranging from 0 to 1, is
1845 generated to estimate the confidence of the predicted interaction. This score integrates structural
1846 features such as interface size and pLDDT confidence. Notably, the list of the P-body-enriched and -
1847 depleted proteins was based on Hubstenberger et al. [116]. The list was also determined based on the
1848 direction of the most extreme fold-change, with only proteins meeting a p-value < 0.05 without
1849 applying a strict fold-change cutoff, considered significant. In addition, proteins that were not also
1850 identified as interactors of DDX6 (a key resident protein of P-bodies) as characterized in the literature
1851 [115] were filtered out. Accordingly, positive controls correspond to FC > 1.58, while negative controls
1852 correspond to FC < -0.71.

1853 **Analysis of post-mortem patient RNA-seq data for depleted and enriched P-body genes**

1854 Data sources:

1855 - Bulk RNA-seq data from Edward Lee, "Loss of Nuclear TDP-43 Is Associated with
1856 Decondensation of LINE Retrotransposons"[140].
1857 - List of enriched and depleted genes from Hubstenberger et al, "P-Body Purification Reveals
1858 the Condensation of Repressed mRNA Regulons"[116].

1859 Bulk RNA-seq count tables (raw counts and TPM) from the GSE126542 dataset were downloaded,
1860 and gene identifiers were mapped to gene symbols using a GRCh38 annotation. To restrict analyses

to expressed genes, we computed the median raw count per gene across samples and retained genes with median > 5 in the raw matrix. Per subject, log2 fold change (L2FC) was calculated as log2(TPM_NEG / TPM_POS).
For P-body gene set construction, we retained genes with median count ≥ 5 P-body–enriched genes were defined by FDR ≤ 0.05 and enrichment ≥ 1, and P-body–depleted genes by FDR ≤ 0.05 and enrichment ≤ −1.

Per patient, variable genes were defined as those with absolute L2FC ≥ 1. We then counted up-regulated (L2FC > 0) and down-regulated (L2FC < 0) genes and computed the percentage down-regulated. This was done separately within the enriched and depleted P-body subsets. A 2×2 contingency table per-patient was constructed. One-sided Fisher's exact tests were performed, with the alternative hypothesis being greater down-regulation in P-body–enriched genes compared to depleted genes. P-values across subjects were adjusted by Benjamini–Hochberg FDR. To combine evidence across subjects while controlling for subject as a stratum, we performed a Cochran–Mantel–Haenszel (CMH) test on the set of per-subject 2×2 tables. The analysis reported the CMH χ^2 statistic and p-value, the Mantel–Haenszel common odds ratio with a 95% confidence interval obtained via the Mantel–Haenszel method, and a one-sided p-value in the expected direction derived from the two-sided CMH p-value.

Data availability

Proximity labeling proteomics data are available in ProteomeXchange (PXD056534).
SLAM-seq RNA-seq data are available in GEO (GSE279980).

The imaging dataset[187] can be downloaded via Amazon S3 API. Bucket name: organellomics, region: eu-west-1. (https://organellomics.s3.amazonaws.com). A script for downloading the data is available on our Github repository. To browse the data we suggest using Cyberduck (https://cyberduck.io/). Detailed instructions are provided in the README file on our Github repository.

Software and hardware

All deep-learning architectures were implemented in Pytorch version 2.2.2[188], cuda version 11.8 on Python v3.9.19. The training was performed on an NVIDIA A40 (48GB GPU) card.

Code availability

The code can be found on our Github page: https://github.com/Sagykri/NOVA[189]

Extendend statistical values

Detailed tables of statistical parameters and their values for each dataset are provided in the supplementary materials files.

Figure design

We placed and organized all the figures by using Adobe Illustrator software, which was also used for generating **Figure 1A**. The graphs were generated either by Prism (version 5.9.1 or 10) or via python (v3.9.19; matplotlib (v3.8.4) and seaborn (v0.13.2)). Representative confocal images were generated by FiJi software v. 1.52p. or ZEN software. We generated the graphical abstract, **Figures 1B**, **2A**, **4L**, **5A,E,R** and **Supplementary Figures 1,2,4,6,10,11,** and **17** by Biorender.com.

Acknowledgments

We wish to thank Leeat Keren (WIS), Maya Schuldiner (WIS), Eran Segal (WIS) Sasha Devore (WIS), Ernest Fraenkel (MIT), Hirofumi Kobayashi (Chan Zuckerberg Biohub), Assaf Zaritzky (BGU), Tomer Lapidot (UPENN), Ophir Shalem (UPENN) and Johnathan Cooper Knock (U Sheffield) for advice during project development and on the manuscript draft. We thank Michael Ward (NINDS, NIH) and Bill Skarnes (Jackson labs) for early access to iNDI lines Nancy Kadersha Paul Anderson and Pavel Ivanov (HMS) for G3BP1 and YFP-DCP1A U2OS cells. Shai Bagon (WIS) and Ron Rotkofp (WIS) for advice in statistical and computational sides. Alon Savidor (WIS) and Yishai Levin (WIS) for Mass spectrometry. For the RNA-seq procedure for SLAM-seq, we wish to thank Inbal Bolocan Nachman (WIS). We thank Chen Eitan, Aviad Siany, Jazz Lubliner, Yahel Cohen, Emmanuel Amzalleg, and Lior Lin for preliminary experiments that are not in the scope of the final manuscript.
EH is the Mondry Family Professorial Chair and Head of the Andrea L. and Lawrence A. Wolfe Family Center for Research on Neuroimmunology and Neuromodulation. Funding for research: Binational Science Foundation (BSF); Association Francaise Contre les Myopathies (AFM); Amyotrophic Lateral Sclerosis Association (ALSA); Target ALS; Israel Science Foundation (ISF 3497/21, 424/22, 494/24); ALS Canada; Minna-James-Heineman Stiftung through Minerva, Minerva Foundation, with funding from the Federal German Ministry for Education and Research; Robert Packard Center for ALS Research at Johns Hopkins; McGill University; EU - ERA-Net; Radala Foundation for ALS Research; Additional support generously provided by the Kekst Family Institute for Medical Genetics. Weizmann SABRA - Yeda-Sela - WRC Program, the Estate of Emile Mimran, and The Maurice and Vivienne Wohl Biology Endowment. Nella and Leon Benoziyo Center for Neurological Diseases. Goldhirsh-Yellin Foundation. Dr. Sydney Brenner and friends. Weizmann - Center for Research on Neurodegeneration. Redhill Foundation – Sam and Jean Rothberg Charitable Trust Dr. Dvora and Haim Teitelbaum Endowment Fund. This research was supported in part by the Intramural research Program of the NIH, National institute on Aging and National Institutes of Neurological Diseases and Stroke. LM is funded by a Minerva Postdoctoral Fellowship. YDM was funded by the Weizmann - CNRS (Centre National de la Recherche Scientifique) Collaboration Program.

1932 **References**

1933 1. Gottschling, D. E. & Nyström, T. The Upsides and Downsides of Organelle Interconnectivity. *Cell*
1934 **169**, 24–34 (2017).
1935 2. Zung, N. & Schuldiner, M. New horizons in mitochondrial contact site research. *Biol. Chem.* **401**,
1936 793–809 (2020).
1937 3. Itzhak, D. N. *et al.* A Mass Spectrometry-Based Approach for Mapping Protein Subcellular
1938 Localization Reveals the Spatial Proteome of Mouse Primary Neurons. *Cell Rep.* **20**, 2706–2718
1939 (2017).
1940 4. Borner, G. H. H. Organellar Maps Through Proteomic Profiling - A Conceptual Guide. *Mol. Cell.*
1941 *Proteomics* **19**, 1076–1087 (2020).
1942 5. Schessner, J. P., Albrecht, V., Davies, A. K., Sinitcyn, P. & Borner, G. H. H. Deep and fast label-
1943 free Dynamic Organellar Mapping. *Nat. Commun.* **14**, 5252 (2023).
1944 6. Itzhak, D. N., Schessner, J. P. & Borner, G. H. H. Dynamic organellar maps for spatial proteomics.
1945 *Curr. Protoc. Cell Biol.* **83**, e81 (2019).
1946 7. Thul, P. J. *et al.* A subcellular map of the human proteome. *Science* **356**, (2017).
1947 8. Youn, J.-Y. *et al.* High-Density Proximity Mapping Reveals the Subcellular Organization of mRNA-
1948 Associated Granules and Bodies. *Mol Cell* **69**, 517–532.e11 (2018).
1949 9. Go, C. D. *et al.* A proximity-dependent biotinylation map of a human cell. *Nature* **595**, 120–124
1950 (2021).
1951 10. Hein, M. Y. *et al.* Global organelle profiling reveals subcellular localization and remodeling at
1952 proteome scale. *Cell* **188**, 1137–1155.e20 (2025).
1953 11. Kobayashi, H., Cheveralls, K. C., Leonetti, M. D. & Royer, L. A. Self-supervised deep learning
1954 encodes high-resolution features of protein subcellular localization. *Nat. Methods* **19**, 995–1003
1955 (2022).
1956 12. Spitzer, H., Berry, S., Donoghoe, M., Pelkmans, L. & Theis, F. J. Learning consistent subcellular
1957 landmarks to quantify changes in multiplexed protein maps. *Nat. Methods* **20**, 1058–1069

1958 (2023).

1959 13. Carpenter, A. E. *et al.* CellProfiler: image analysis software for identifying and quantifying cell
1960 phenotypes. *Genome Biol.* **7**, R100 (2006).

1961 14. Heinrich, L. *et al.* Whole-cell organelle segmentation in volume electron microscopy. *Nature*
1962 **599**, 141–146 (2021).

1963 15. Lu, A. X., Kraus, O. Z., Cooper, S. & Moses, A. M. Learning unsupervised feature representations
1964 for single cell microscopy images with paired cell inpainting. *PLoS Comput. Biol.* **15**, e1007348
1965 (2019).

1966 16. Husain, S. S. *et al.* Single-cell subcellular protein localisation using novel ensembles of diverse
1967 deep architectures. *Commun Biol* **6**, 489 (2023).

1968 17. Long, W., Yang, Y. & Shen, H.-B. ImPLoc: a multi-instance deep learning model for the prediction
1969 of protein subcellular localization based on immunohistochemistry images. *Bioinformatics* **36**,
1970 2244–2250 (2020).

1971 18. Kim, K.-M., Son, K. & Palmore, G. T. R. Neuron Image Analyzer: Automated and Accurate
1972 Extraction of Neuronal Data from Low Quality Images. *Sci. Rep.* **5**, 17062 (2015).

1973 19. Ascoli, G. A., Donohue, D. E. & Halavi, M. NeuroMorpho.Org: a central resource for neuronal
1974 morphologies. *J. Neurosci.* **27**, 9247–9251 (2007).

1975 20. Oberlaender, M., Bruno, R. M., Sakmann, B. & Broser, P. J. Transmitted light brightfield mosaic
1976 microscopy for three-dimensional tracing of single neuron morphology. *J. Biomed. Opt.* **12**,
1977 064029 (2007).

1978 21. Moshkov, N. *et al.* Learning representations for image-based profiling of perturbations. *Nat.*
1979 *Commun.* **15**, 1594 (2024).

1980 22. Serrano, E. *et al.* Progress and new challenges in image-based profiling. *arXiv [q-bio.QM]* (2025)
1981 doi:10.48550/ARXIV.2508.05800.

1982 23. Seal, S. *et al.* Cell Painting: a decade of discovery and innovation in cellular imaging. *Nat*
1983 *Methods* **22**, 254–268 (2025).

1984 24. Hirose, T., Ninomiya, K., Nakagawa, S. & Yamazaki, T. A guide to membraneless organelles and
1985 their various roles in gene regulation. *Nat. Rev. Mol. Cell Biol.* (2022) doi:10.1038/s41580-022-
1986 00558-8.
1987 25. Banani, S. F., Lee, H. O., Hyman, A. A. & Rosen, M. K. Biomolecular condensates: organizers of
1988 cellular biochemistry. *Nat. Rev. Mol. Cell Biol.* **18**, 285–298 (2017).
1989 26. Brangwynne, C. P. Phase transitions and size scaling of membrane-less organelles. *J. Cell Biol.*
1990 **203**, 875–881 (2013).
1991 27. Lyon, A. S., Peeples, W. B. & Rosen, M. K. A framework for understanding the functions of
1992 biomolecular condensates across scales. *Nat. Rev. Mol. Cell Biol.* **22**, 215–235 (2021).
1993 28. Alberti, S. & Hyman, A. A. Biomolecular condensates at the nexus of cellular stress, protein
1994 aggregation disease and ageing. *Nat. Rev. Mol. Cell Biol.* **22**, 196–213 (2021).
1995 29. Platt, F. M., d'Azzo, A., Davidson, B. L., Neufeld, E. F. & Tifft, C. J. Lysosomal storage diseases.
1996 *Nat Rev Dis Primers* **4**, 27 (2018).
1997 30. Cox, T. M. & Cachón-González, M. B. The cellular pathology of lysosomal diseases. *J. Pathol.*
1998 **226**, 241–254 (2012).
1999 31. Gorman, G. S. *et al.* Mitochondrial diseases. *Nat Rev Dis Primers* **2**, 16080 (2016).
2000 32. Schapira, A. H. V. Mitochondrial disease. *Lancet* **368**, 70–82 (2006).
2001 33. Levine, B. & Kroemer, G. Autophagy in the pathogenesis of disease. *Cell* **132**, 27–42 (2008).
2002 34. Mizushima, N. & Levine, B. Autophagy in Human Diseases. *N. Engl. J. Med.* **383**, 1564–1576
2003 (2020).
2004 35. Nedelsky, N. B. & Taylor, J. P. Bridging biophysics and neurology: aberrant phase transitions in
2005 neurodegenerative disease. *Nat. Rev. Neurol.* **15**, 272–286 (2019).
2006 36. Alberti, S. & Dormann, D. Liquid-Liquid Phase Separation in Disease. *Annu. Rev. Genet.* **53**, 171–
2007 194 (2019).
2008 37. Dosovitskiy, A. *et al.* An image is worth 16x16 words: Transformers for image recognition at
2009 scale. *arXiv [cs.CV]* (2020).

2010 38. Kim, V., Adaloglou, N., Osterland, M., Morelli, F. & Zapata, P. A. M. Self-supervision advances
2011 morphological profiling by unlocking powerful image representations. (2023)
2012 doi:10.1101/2023.04.28.538691.
2013 39. Doron, M. *et al.* Unbiased single-cell morphology with self-supervised vision transformers.
2014 *bioRxiv* (2023).
2015 40. Kraus, O. *et al.* Masked autoencoders for microscopy are scalable learners of cellular biology.
2016 *arXiv [cs.CV]* (2024).
2017 41. Atmaramani, R. *et al.* Deep Learning Analysis on Images of iPSC-derived Motor Neurons
2018 Carrying fALS-genetics Reveals Disease-Relevant Phenotypes. *bioRxiv* (2024).
2019 42. Natekar, P., Wang, Z., Arora, M., Hakozaki, H. & Schöneberg, J. Self-supervised deep learning
2020 uncovers the semantic landscape of drug-induced latent mitochondrial phenotypes. *bioRxiv*
2021 (2023) doi:10.1101/2023.09.13.557636.
2022 43. Perakis, A. *et al.* Contrastive learning of single-cell phenotypic representations for treatment
2023 classification. in *Machine Learning in Medical Imaging* 565–575 (Springer International
2024 Publishing, Cham, 2021).
2025 44. van den Oord, A., Li, Y. & Vinyals, O. Representation learning with Contrastive Predictive
2026 Coding. *arXiv [cs.LG]* (2018).
2027 45. Khosla, P. *et al.* Supervised Contrastive Learning. *arXiv [cs.LG]* (2020).
2028 46. Bray, M.-A. *et al.* Cell Painting, a high-content image-based assay for morphological profiling
2029 using multiplexed fluorescent dyes. *Nat. Protoc.* **11**, 1757–1774 (2016).
2030 47. Stirling, D. R. *et al.* CellProfiler 4: improvements in speed, utility and usability. *BMC*
2031 *Bioinformatics* **22**, 433 (2021).
2032 48. Cho, N. H. *et al.* OpenCell: Endogenous tagging for the cartography of human cellular
2033 organization. *Science* **375**, eabi6983 (2022).
2034 49. Ye, P. *et al.* Partial Fine-tuning: A successor to full fine-tuning for vision transformers. *arXiv*
2035 *[cs.CV]* (2023).

2036 50. McInnes, L., Healy, J. & Melville, J. UMAP: Uniform Manifold Approximation and Projection for
2037 Dimension Reduction. *arXiv [stat.ML]* (2018).
2038 51. Shai, N. *et al.* Systematic mapping of contact sites reveals tethers and a function for the
2039 peroxisome-mitochondria contact. *Nat Commun* **9**, 1761 (2018).
2040 52. Wong, Y. C., Ysselstein, D. & Krainc, D. Mitochondria-lysosome contacts regulate mitochondrial
2041 fission via RAB7 GTP hydrolysis. *Nature* **554**, 382–386 (2018).
2042 53. DiGiovanni, L. F. *et al.* ROS transfer at peroxisome-mitochondria contact regulates
2043 mitochondrial redox. *Science* **389**, 157–162 (2025).
2044 54. Chu, B.-B. *et al.* Cholesterol transport through lysosome-peroxisome membrane contacts. *Cell*
2045 **184**, 289 (2021).
2046 55. Deus, C. M., Yambire, K. F., Oliveira, P. J. & Raimundo, N. Mitochondria-lysosome crosstalk:
2047 From physiology to neurodegeneration. *Trends Mol. Med.* **26**, 71–88 (2020).
2048 56. Kim, S., Wong, Y. C., Gao, F. & Krainc, D. Dysregulation of mitochondria-lysosome contacts by
2049 GBA1 dysfunction in dopaminergic neuronal models of Parkinson's disease. *Nat Commun* **12**,
2050 1807 (2021).
2051 57. Du, M., Ea, C.-K., Fang, Y. & Chen, Z. J. Liquid phase separation of NEMO induced by
2052 polyubiquitin chains activates NF-κB. *Mol. Cell* **82**, 2415–2426.e5 (2022).
2053 58. West, J. A. *et al.* Structural, super-resolution microscopy analysis of paraspeckle nuclear body
2054 organization. *J. Cell Biol.* **214**, 817–830 (2016).
2055 59. Naganuma, T. *et al.* Alternative 3'-end processing of long noncoding RNA initiates construction
2056 of nuclear paraspeckles. *EMBO J.* **31**, 4020–4034 (2012).
2057 60. Arseni, D. *et al.* Heteromeric amyloid filaments of ANXA11 and TDP-43 in FTLD-TDP Type C.
2058 *Nature* (2024) doi:10.1038/s41586-024-08024-5.
2059 61. Robinson, J. L. *et al.* Annexin A11 aggregation in FTLD-TDP type C and related
2060 neurodegenerative disease proteinopathies. *Acta Neuropathol* **147**, 104 (2024).
2061 62. Miedema, S. S. M. *et al.* Proteomics of the temporal cortex in semantic dementia reveals brain-

2062 region specific molecular pathology and regulation of the TDP-43-ANXA11 interactome. *Acta*
2063 *Neuropathol Commun* **13**, 162 (2025).
2064 63. Hodgson, R. *et al.* TDP-43 is a Master Regulator of Paraspeckle Condensation. (2024)
2065 doi:10.2139/ssrn.4721338.
2066 64. Nishimoto, Y. *et al.* The long non-coding RNA nuclear-enriched abundant transcript 1_2 induces
2067 paraspeckle formation in the motor neuron during the early phase of amyotrophic lateral
2068 sclerosis. *Mol Brain* **6**, 31 (2013).
2069 65. Chazotte, B. Labeling nuclear DNA with hoechst 33342. *Cold Spring Harb. Protoc.* **2011**,
2070 db.prot5557 (2011).
2071 66. Chazotte, B. Labeling mitochondria with MitoTracker dyes. *Cold Spring Harb. Protoc.* **2011**, 990–
2072 992 (2011).
2073 67. Wurm, C. A. *et al.* Nanoscale distribution of mitochondrial import receptor Tom20 is adjusted to
2074 cellular conditions and exhibits an inner-cellular gradient. *Proc. Natl. Acad. Sci. U. S. A.* **108**,
2075 13546–13551 (2011).
2076 68. Turner, D. L., Korneev, D. V., Purdy, J. G., de Marco, A. & Mathias, R. A. The host exosome
2077 pathway underpins biogenesis of the human cytomegalovirus virion. *Elife* **9**, e58288 (2020).
2078 69. Nava, C. *et al.* Hypomorphic variants of cationic amino acid transporter 3 in males with autism
2079 spectrum disorders. *Amino Acids* **47**, 2647–2658 (2015).
2080 70. Chazotte, B. Labeling cytoskeletal F-actin with rhodamine phalloidin or fluorescein phalloidin for
2081 imaging. *Cold Spring Harb. Protoc.* **2010**, db.prot4947 (2010).
2082 71. Brinkley, B. R., Fistel, S. H., Marcum, J. M. & Pardue, R. L. Microtubules in cultured cells; indirect
2083 immunofluorescent staining with tubulin antibody. *Int. Rev. Cytol.* **63**, 59–95 (1980).
2084 72. Zocchi, R., Compagnucci, C., Bertini, E. & Sferra, A. Deciphering the tubulin language: Molecular
2085 determinants and readout mechanisms of the tubulin code in neurons. *Int. J. Mol. Sci.* **24**, 2781
2086 (2023).
2087 73. Lauria, G. *et al.* Tubule and neurofilament immunoreactivity in human hairy skin: markers for

2088 intraepidermal nerve fibers. *Muscle Nerve* **30**, 310–316 (2004).

2089 74. Kageyama, S. *et al.* p62/SQSTM1-droplet serves as a platform for autophagosome formation
2090 and anti-oxidative stress response. *Nat. Commun.* **12**, 16 (2021).

2091 75. Gowrishankar, S., Wu, Y. & Ferguson, S. M. Impaired JIP3-dependent axonal lysosome transport
2092 promotes amyloid plaque pathology. *J. Cell Biol.* **216**, 3291–3305 (2017).

2093 76. Koyano, F. *et al.* Parkin-mediated ubiquitylation redistributes MITOL/March5 from
2094 mitochondria to peroxisomes. *EMBO Rep.* **20**, e47728 (2019).

2095 77. Tsygankova, O. M. & Keen, J. H. A unique role for clathrin light chain A in cell spreading and
2096 migration. *J. Cell Sci.* **132**, (2019).

2097 78. Srivastava, M., Fleming, P. J., Pollard, H. B. & Burns, A. L. Cloning and sequencing of the human
2098 nucleolin cDNA. *FEBS Lett.* **250**, 99–105 (1989).

2099 79. Fox, A. H., Bond, C. S. & Lamond, A. I. P54nrb forms a heterodimer with PSP1 that localizes to
2100 paraspeckles in an RNA-dependent manner. *Mol. Biol. Cell* **16**, 5304–5315 (2005).

2101 80. Fox, A. H. *et al.* Paraspeckles: a novel nuclear domain. *Curr. Biol.* **12**, 13–25 (2002).

2102 81. Tsuji, H. *et al.* Epitope mapping of antibodies against TDP-43 and detection of protease-
2103 resistant fragments of pathological TDP-43 in amyotrophic lateral sclerosis and frontotemporal
2104 lobar degeneration. *Biochem. Biophys. Res. Commun.* **417**, 116–121 (2012).

2105 82. Yang, L., Gal, J., Chen, J. & Zhu, H. Self-assembled FUS binds active chromatin and regulates
2106 gene transcription. *Proc. Natl. Acad. Sci. U. S. A.* **111**, 17809–17814 (2014).

2107 83. Weis, K. *et al.* Retinoic acid regulates aberrant nuclear localization of PML-RAR alpha in acute
2108 promyelocytic leukemia cells. *Cell* **76**, 345–356 (1994).

2109 84. Eystathioy, T. *et al.* The GW182 protein colocalizes with mRNA degradation associated proteins
2110 hDcp1 and hLSm4 in cytoplasmic GW bodies. *RNA* **9**, 1171–1173 (2003).

2111 85. Yang, W.-H., Yu, J. H., Gulick, T., Bloch, K. D. & Bloch, D. B. RNA-associated protein 55 (RAP55)
2112 localizes to mRNA processing bodies and stress granules. *RNA* **12**, 547–554 (2006).

2113 86. Tourrière, H. *et al.* The RasGAP-associated endoribonuclease G3BP assembles stress granules. *J.*

2114 *Cell Biol.* **160**, 823–831 (2003).

2115 87. Liao, Y.-C. *et al.* RNA Granules Hitchhike on Lysosomes for Long-Distance Transport, Using
2116 Annexin A11 as a Molecular Tether. *Cell* **179**, 147–164.e20 (2019).

2117 88. Daigle, J. G. *et al.* Pur-alpha regulates cytoplasmic stress granule dynamics and ameliorates FUS
2118 toxicity. *Acta Neuropathol.* **131**, 605–620 (2016).

2119 89. Molitor, L. *et al.* Depletion of the RNA-binding protein PURA triggers changes in
2120 posttranscriptional gene regulation and loss of P-bodies. *Nucleic Acids Res.* **51**, 1297–1316
2121 (2023).

2122 90. Liu, M. *et al.* KIF5A-dependent axonal transport deficiency disrupts autophagic flux in
2123 trimethyltin chloride-induced neurotoxicity. *Autophagy* **17**, 903–924 (2021).

2124 91. Ray, S. *et al.* α-Synuclein aggregation nucleates through liquid-liquid phase separation. *Nat.*
2125 *Chem.* **12**, 705–716 (2020).

2126 92. Bayer, T. A. *et al.* Neural expression profile of alpha-synuclein in developing human cortex.
2127 *Neuroreport* **10**, 2799–2803 (1999).

2128 93. Sampedro, M. N., Bussineau, C. M. & Cotman, C. W. Postsynaptic density antigens: preparation
2129 and characterization of an antiserum against postsynaptic densities. *J. Cell Biol.* **90**, 675–686
2130 (1981).

2131 94. Lai, A., Valdez-Sinon, A. N. & Bassell, G. J. Regulation of RNA granules by FMRP and implications
2132 for neurological diseases. *Traffic* **21**, 454–462 (2020).

2133 95. Sharma, A., Takata, H., Shibahara, K.-I., Bubulya, A. & Bubulya, P. A. Son is essential for nuclear
2134 speckle organization and cell cycle progression. *Mol. Biol. Cell* **21**, 650–663 (2010).

2135 96. Protter, D. S. W. & Parker, R. Principles and Properties of Stress Granules. *Trends Cell Biol.* **26**,
2136 668–679 (2016).

2137 97. Anderson, P. & Kedersha, N. RNA granules: post-transcriptional and epigenetic modulators of
2138 gene expression. *Nat. Rev. Mol. Cell Biol.* **10**, 430–436 (2009).

2139 98. Ramos, D. M., Skarnes, W. C., Singleton, A. B., Cookson, M. R. & Ward, M. E. Tackling

2140 neurodegenerative diseases with genomic engineering: A new stem cell initiative from the NIH.
2141 *Neuron* **109**, 1080–1083 (2021).
2142 99. Waibel, S., Neumann, M., Rabe, M., Meyer, T. & Ludolph, A. C. Novel missense and truncating
2143 mutations in FUS/TLS in familial ALS. *Neurology* **75**, 815–817 (2010).
2144 100. Bosco, D. A. *et al.* Mutant FUS proteins that cause amyotrophic lateral sclerosis incorporate into
2145 stress granules. *Hum Mol Genet* **19**, 4160–4175 (2010).
2146 101. Rutherford, N. J. *et al.* Novel mutations in TARDBP (TDP-43) in patients with familial
2147 amyotrophic lateral sclerosis. *PLoS Genet.* **4**, e1000193 (2008).
2148 102. Sreedharan, J. *et al.* TDP-43 mutations in familial and sporadic amyotrophic lateral sclerosis.
2149 *Science* **319**, 1668–1672 (2008).
2150 103. Kenna, K. P. *et al.* Delineating the genetic heterogeneity of ALS using targeted high-throughput
2151 sequencing. *J. Med. Genet.* **50**, 776–783 (2013).
2152 104. Freischmidt, A. *et al.* Haploinsufficiency of TBK1 causes familial ALS and fronto-temporal
2153 dementia. *Nat. Neurosci.* **18**, 631–636 (2015).
2154 105. Rothstein, J. D. *et al.* Sporadic ALS induced pluripotent stem cell derived neurons reveal
2155 hallmarks of TDP-43 loss of function. *Nat Commun* **16**, 7092 (2025).
2156 106. Neumann, M. *et al.* Ubiquitinated TDP-43 in frontotemporal lobar degeneration and
2157 amyotrophic lateral sclerosis. *Science* **314**, 130–133 (2006).
2158 107. Balendra, R. *et al.* Amyotrophic lateral sclerosis caused by TARDBP mutations: from genetics to
2159 TDP-43 proteinopathy. *Lancet Neurol.* **24**, 456–470 (2025).
2160 108. Birsa, N., Bentham, M. P. & Fratta, P. Cytoplasmic functions of TDP-43 and FUS and their role in
2161 ALS. *Semin Cell Dev Biol* **99**, 193–201 (2020).
2162 109. Wagner, K. *et al.* Induced proximity to PML protects TDP-43 from aggregation via SUMO-
2163 ubiquitin networks. *Nat Chem Biol* **21**, 1408–1419 (2025).
2164 110. Antoniani, F. *et al.* Loss of PML nuclear bodies in familial amyotrophic lateral sclerosis-
2165 frontotemporal dementia. *Cell Death Discov* **9**, 248 (2023).

2166 111. Gasset-Rosa, F. *et al.* Cytoplasmic TDP-43 De-mixing Independent of Stress Granules Drives
2167 Inhibition of Nuclear Import, Loss of Nuclear TDP-43, and Cell Death. *Neuron* **102**, 339–357.e7
2168 (2019).
2169 112. Bryant, P. & Noé, F. Improved protein complex prediction with AlphaFold-multimer by
2170 denoising the MSA profile. *PLoS Comput. Biol.* **20**, e1012253 (2024).
2171 113. Bryant, P., Pozzati, G. & Elofsson, A. Improved prediction of protein-protein interactions using
2172 AlphaFold2. *Nat. Commun.* **13**, 1265 (2022).
2173 114. Burke, D. F. *et al.* Towards a structurally resolved human protein interaction network. *Nat.*
2174 *Struct. Mol. Biol.* **30**, 216–225 (2 2023).
2175 115. Ayache, J. *et al.* P-body assembly requires DDX6 repression complexes rather than decay or
2176 Ataxin2/2L complexes. *Mol Biol Cell* **26**, 2579–2595 (2015).
2177 116. Hubstenberger, A. *et al.* P-Body Purification Reveals the Condensation of Repressed mRNA
2178 Regulons. *Mol. Cell* **68**, 144–157.e5 (10 2017).
2179 117. Marmor-Kollet, H. *et al.* Spatiotemporal Proteomic Analysis of Stress Granule Disassembly Using
2180 APEX Reveals Regulation by SUMOylation and Links to ALS Pathogenesis. *Mol. Cell* **80**, 876–
2181 891.e6 (2020).
2182 118. Lam, S. S. *et al.* Directed evolution of APEX2 for electron microscopy and proximity labeling.
2183 *Nat. Methods* **12**, 51–54 (1 2014).
2184 119. Hung, V. *et al.* Spatially resolved proteomic mapping in living cells with the engineered
2185 peroxidase APEX2. *Nat. Protoc.* **11**, 456–475 (2016).
2186 120. Ashburner, M. *et al.* Gene Ontology: tool for the unification of biology. *Nature Genetics 2000*
2187 *25:1* **25**, 25–29 (5 2000).
2188 121. Consortium, T. G. O. *et al.* The Gene Ontology knowledgebase in 2023. *Genetics* **224**, (5 2023).
2189 122. Liu, J., Valencia-Sanchez, M. A., Hannon, G. J. & Parker, R. MicroRNA-dependent localization of
2190 targeted mRNAs to mammalian P-bodies. *Nat Cell Biol* **7**, 719–723 (2005).
2191 123. Sen, G. L. & Blau, H. M. Argonaute 2/RISC resides in sites of mammalian mRNA decay known as

2192 cytoplasmic bodies. *Nat Cell Biol* **7**, 633–636 (2005).

2193 124. Standart, N. & Weil, D. P-bodies: Cytosolic droplets for coordinated mRNA storage. *Trends*
2194 *Genet.* **34**, 612–626 (2018).

2195 125. Jain, S. & Parker, R. The discovery and analysis of P Bodies. *Adv. Exp. Med. Biol.* **768**, 23–43
2196 (2013).

2197 126. Gasset-Rosa, F. *et al.* Cytoplasmic TDP-43 De-mixing Independent of Stress Granules Drives
2198 Inhibition of Nuclear Import, Loss of Nuclear TDP-43, and Cell Death. *Neuron* vol. 102 339–
2199 357.e7 Preprint at https://doi.org/10.1016/j.neuron.2019.02.038 (4 2019).

2200 127. Dewey, C. M. *et al.* TDP-43 is directed to stress granules by sorbitol, a novel physiological
2201 osmotic and oxidative stressor. *Mol. Cell. Biol.* **31**, 1098–1108 (2011).

2202 128. Lee, Y.-B. *et al.* Cytoplasmic TDP-43 is involved in cell fate during stress recovery. *Hum. Mol.*
2203 *Genet.* **31**, 166–175 (2021).

2204 129. Luo, Y., Na, Z. & Slavoff, S. A. P-Bodies: Composition, Properties, and Functions. *Biochemistry*
2205 **57**, 2424–2431 (5 2018).

2206 130. Herzog, V. A. *et al.* Thiol-linked alkylation of RNA to assess expression dynamics. *Nat. Methods*
2207 **14**, 1198–1204 (12 2017).

2208 131. Jürges, C., Dölken, L. & Erhard, F. Dissecting newly transcribed and old RNA using GRAND-SLAM.
2209 *Bioinformatics* **34**, i218–i226 (2018).

2210 132. Rummel, T., Sakellaridi, L. & Erhard, F. grandR: a comprehensive package for nucleotide
2211 conversion RNA-seq data analysis. *Nat. Commun.* **14**, 3559 (2023).

2212 133. Baskerville, V., Rapuri, S., Mehlhop, E. & Coyne, A. N. SUN1 facilitates CHMP7 nuclear influx and
2213 injury cascades in sporadic amyotrophic lateral sclerosis. *Brain* **147**, 109–121 (2024).

2214 134. Macleod, M. *et al.* The MDAR (Materials Design Analysis Reporting) Framework for transparent
2215 reporting in the life sciences. *Proc Natl Acad Sci U S A* **118**, (2021).

2216 135. Almeida, S. & Gao, F.-B. Lost & found: C9ORF72 and the autophagy pathway in ALS/FTD. *EMBO*
2217 *J* **35**, 1251–1253 (2016).

2218 136. Beckers, J., Tharkeshwar, A. K. & Van Damme, P. C9orf72 ALS-FTD: recent evidence for
2219 dysregulation of the autophagy-lysosome pathway at multiple levels. *Autophagy* **17**, 3306–3322
2220 (2021).
2221 137. Trist, B. G. *et al.* Co-deposition of SOD1, TDP-43 and p62 proteinopathies in ALS: evidence for
2222 multifaceted pathways underlying neurodegeneration. *Acta Neuropathol. Commun.* **10**, 122
2223 (2022).
2224 138. Guise, A. J. *et al.* TDP-43-stratified single-cell proteomics of postmortem human spinal motor
2225 neurons reveals protein dynamics in amyotrophic lateral sclerosis. *Cell Rep.* **43**, 113636 (2024).
2226 139. Spence, H. *et al.* RNA aptamer reveals nuclear TDP-43 pathology is an early aggregation event
2227 that coincides with STMN-2 cryptic splicing and precedes clinical manifestation in ALS. *Acta*
2228 *Neuropathol.* **147**, 50 (2024).
2229 140. Liu, E. Y. *et al.* Loss of Nuclear TDP-43 Is Associated with Decondensation of LINE
2230 Retrotransposons. *Cell Rep* **27**, 1409–1421.e6 (2019).
2231 141. Workman, M. J. *et al.* Large-scale differentiation of iPSC-derived motor neurons from ALS and
2232 control subjects. *Neuron* **111**, 1191–1204.e5 (2023).
2233 142. Bussi, C. *et al.* Stress granules plug and stabilize damaged endolysosomal membranes. *Nature*
2234 **623**, 1062–1069 (2023).
2235 143. Amen, T. & Kaganovich, D. Stress granules inhibit fatty acid oxidation by modulating
2236 mitochondrial permeability. *Cell Rep.* **35**, 109237 (2021).
2237 144. Qin, W. *et al.* Dynamic mapping of proteome trafficking within and between living cells by
2238 TransitID. *Cell* **186**, 3307–3324.e30 (2023).
2239 145. Stoecklin, G. & Kedersha, N. Relationship of GW/P-bodies with stress granules. *Adv. Exp. Med.*
2240 *Biol.* **768**, 197–211 (2013).
2241 146. Cohen, S., Valm, A. M. & Lippincott-Schwartz, J. Interacting organelles. *Curr. Opin. Cell Biol.* **53**,
2242 84–91 (2018).
2243 147. Donahue, E. K. F., Ruark, E. M. & Burkewitz, K. Fundamental roles for inter-organelle

2244 communication in aging. *Biochem. Soc. Trans.* **50**, 1389–1402 (2022).

2245 148. Rossini, M., Pizzo, P. & Filadi, R. Better to keep in touch: investigating inter-organelle cross-talk.
2246 *FEBS J.* **288**, 740–755 (2021).

2247 149. Schrader, M., Kamoshita, M. & Islinger, M. Organelle interplay-peroxisome interactions in
2248 health and disease. *J. Inherit. Metab. Dis.* **43**, 71–89 (2020).

2249 150. Mitrea, D. M. *et al.* Methods for Physical Characterization of Phase-Separated Bodies and
2250 Membrane-less Organelles. *J. Mol. Biol.* **430**, 4773–4805 (2018).

2251 151. Shin, M.-G. *et al.* RMeDPower for Biology: guiding design, experimental structure and analyses
2252 of repeated measures data for biological studies. *bioRxiv* 2022.07.18.500490 (2022)
2253 doi:10.1101/2022.07.18.500490.

2254 152. Black, S. *et al.* CODEX multiplexed tissue imaging with DNA-conjugated antibodies. *Nat. Protoc.*
2255 **16**, 3802–3835 (2021).

2256 153. Gut, G., Herrmann & Pelkmans, L. Multiplexed protein maps link subcellular organization to
2257 cellular states. *Science* **361**, (2018).

2258 154. Singh, S. P. *et al.* 3D Deep Learning on Medical Images: A Review. *Sensors* **20**, (2020).

2259 155. Caicedo, J. C. *et al.* Data-analysis strategies for image-based cell profiling. *Nat. Methods* **14**,
2260 849–863 (2017).

2261 156. Sun, J., Tárnok, A. & Su, X. Deep learning-based single-cell optical image studies. *Cytometry A*
2262 **97**, 226–240 (2020).

2263 157. Lavitt, F., Rijlaarsdam, D. J., van der Linden, D., Weglarz-Tomczak, E. & Tomczak, J. M. Deep
2264 learning and transfer learning for automatic cell counting in microscope images of human
2265 cancer cell lines. *Appl. Sci.* **11**, 4912 (2021).

2266 158. Sahin, U. *et al.* Oxidative stress-induced assembly of PML nuclear bodies controls sumoylation
2267 of partner proteins. *J Cell Biol* **204**, 931–945 (2014).

2268 159. Chen, J. *et al.* Oxidative stress disrupts the cytoskeleton of spinal motor neurons. *Brain Behav*
2269 **13**, e2870 (2023).

2270 160. Rhoads, S. N. *et al.* Neurons and astrocytes have distinct organelle signatures and responses to
2271 stress. *Cell Rep* **44**, 116280 (2025).
2272 161. Mutihac, R. *et al.* TARDBP pathogenic mutations increase cytoplasmic translocation of TDP-43
2273 and cause reduction of endoplasmic reticulum Ca^{2+} signaling in motor neurons. *Neurobiol. Dis.*
2274 **75**, 64–77 (2015).
2275 162. Hulme, A. J., Maksour, S., St-Clair Glover, M., Miellet, S. & Dottori, M. Making neurons, made
2276 easy: The use of Neurogenin-2 in neuronal differentiation. *Stem Cell Reports* **17**, 14–34 (2022).
2277 163. Hofweber, M. *et al.* Phase Separation of FUS Is Suppressed by Its Nuclear Import Receptor and
2278 Arginine Methylation. *Cell* **173**, 706–719.e13 (2018).
2279 164. Yoshizawa, T. *et al.* Nuclear Import Receptor Inhibits Phase Separation of FUS through Binding
2280 to Multiple Sites. *Cell* **173**, 693–705.e22 (2018).
2281 165. Dormann, D. *et al.* ALS-associated fused in sarcoma (FUS) mutations disrupt Transportin-
2282 mediated nuclear import. *EMBO J.* **29**, 2841–2857 (2010).
2283 166. Aulas, A. *et al.* G3BP1 promotes stress-induced RNA granule interactions to preserve
2284 polyadenylated mRNA. *J. Cell Biol.* **209**, 73–84 (2015).
2285 167. Ye, Y. *et al.* DCPS modulates TDP-43 mediated neurodegeneration through P-body regulation.
2286 *bioRxiv* (2025) doi:10.1101/2025.06.13.659508.
2287 168. Xie, L. *et al.* Context-dependent Interactors Regulate TDP-43 Dysfunction in ALS/FTLD. *bioRxiv*
2288 (2025) doi:10.1101/2025.04.07.646890.
2289 169. Pantazis, C. B. *et al.* A reference human induced pluripotent stem cell line for large-scale
2290 collaborative studies. *Cell Stem Cell* **29**, 1685–1702.e22 (2022).
2291 170. Fernandopulle, M. S. *et al.* Transcription Factor-Mediated Differentiation of Human iPSCs into
2292 Neurons. *Curr. Protoc. Cell Biol.* **79**, e51 (2018).
2293 171. Lee, S.-Y. *et al.* APEX Fingerprinting Reveals the Subcellular Localization of Proteins of Interest.
2294 *Cell Rep.* **15**, 1837–1847 (2016).
2295 172. Baxi, E. G. *et al.* Answer ALS, a large-scale resource for sporadic and familial ALS combining

2296 clinical and multi-omics data from induced pluripotent cell lines. *Nat Neurosci* **25**, 226–237
2297 (2022).
2298 173. Rothstein, J. D., Warlick, C. & Coyne, A. N. Highly variable molecular signatures of TDP-43 loss of
2299 function are associated with nuclear pore complex injury in a population study of sporadic ALS
2300 patient iPSNs. *bioRxiv* (2023) doi:10.1101/2023.12.12.571299.
2301 174. Coyne, A. N. *et al.* Nuclear accumulation of CHMP7 initiates nuclear pore complex injury and
2302 subsequent TDP-43 dysfunction in sporadic and familial ALS. *Sci. Transl. Med.* **13**, (2021).
2303 175. Cox, J. & Mann, M. MaxQuant enables high peptide identification rates, individualized p.p.b.-
2304 range mass accuracies and proteome-wide protein quantification. *Nat. Biotechnol.* **26**, 1367–
2305 1372 (2008).
2306 176. Tyanova, S. *et al.* The Perseus computational platform for comprehensive analysis of
2307 (prote)omics data. *Nature Methods 2016 13:9* **13**, 731–740 (6 2016).
2308 177. Waldron, F. M., Rifai, O. & Gregory, J. Antibody and TDP-43 RNA aptamer dual staining to detect
2309 patterns of co-pathology in FFPE-preserved human t. (2024).
2310 178. Jaitin, D. A. *et al.* Massively parallel single-cell RNA-seq for marker-free decomposition of
2311 tissues into cell types. *Science* **343**, 776–779 (2014).
2312 179. Keren-Shaul, H. *et al.* MARS-seq2.0: an experimental and analytical pipeline for indexed sorting
2313 combined with single-cell RNA sequencing. *Nat. Protoc.* **14**, 1841–1862 (2019).
2314 180. Dobin, A. *et al.* STAR: ultrafast universal RNA-seq aligner. *Bioinformatics* **29**, 15–21 (2013).
2315 181. Finkel, Y. *et al.* SARS-CoV-2 uses a multipronged strategy to impede host protein synthesis.
2316 *Nature* **594**, 240–245 (2021).
2317 182. Brenner, J. F. *et al.* An automated microscope for cytologic research a preliminary evaluation. *J.*
2318 *Histochem. Cytochem.* **24**, 100–111 (1976).
2319 183. Stringer, C., Wang, T., Michaelos, M. & Pachitariu, M. Cellpose: a generalist algorithm for
2320 cellular segmentation. *Nat. Methods* **18**, 100–106 (2021).
2321 184. Bozinovski, S. Reminder of the first paper on transfer learning in neural networks, 1976.

Informatica (Ljubl.) **44**, (2020).

185. Abnar, S. & Zuidema, W. Quantifying attention flow in transformers. *arXiv [cs.LG]* (2020) doi:10.48550/ARXIV.2005.00928.

186. Bryant, P. & Noé, F. Rapid protein-protein interaction network creation from multiple sequence alignments with Deep Learning. *bioRxiv* 2023.04.15.536993 (4 2023).

187. Krispin, S. & Van Zuiden, W., Danino, Y., Rudberg, N., Molitor, L., Abarbanel, B., Aviram, G., Wolf, G., Bar, C., Siani, A., Meimoun, T., Coyne, A., Santiana, M., Weller, C., Cookson, M., Ward, M., Waldron, F., Gregory, J., Fisher, T., Nachshon, A., Stern-Ginossar, N., Yacovzada, N., Hornstein, E. Organellomics: AI-driven deep organellar phenotyping reveals novel ALS mechanisms in human neurons (Dataset). Zenodo. https://doi.org/10.5281/zenodo.18152964.

188. Paszke, A. *et al.* Pytorch: An imperative style, high-performance deep learning library. *Adv. Neural Inf. Process. Syst.* **32**, (2019).

189. Krispin, S. & Van Zuiden, W. , Danino, Y. , Rudberg, N. , Molitor, L. , Abarbanel, B. , Aviram, G. , Wolf, G. , Bar, C. , Siani, A. , Meimoun, T. , Coyne, A. , Santiana, M. , Weller, C. , Cookson, M. , Ward, M. , Waldron, F. , Gregory, J. , Fisher, T. , Nachshon, A. , Stern-Ginossar, N. , Yacovzada, N. , Hornstein, E. Organellomics: AI-driven deep organellar phenotyping reveals novel ALS mechanisms in human neurons (Source Code). Zenodo. https://doi.org/10.5281/zenodo.18152732.